E. coli Nissle 1917 as a potential chassis for osmolality biosensors in the gut

Maria T. Orozco Hidalgo

A thesis
in
The Department
of
Biology

Presented in Partial Fulfillment of the Requirements For the Degree of Master of Science (Biology)
at Concordia University
Montréal, Québec, Canada

May 2023

CONCORDIA UNIVERSITY

School of Graduate Studies

This is to certify that the thesis prepared

By: **Maria T. Orozco Hidalgo**

Entitled: ***E. coli* Nissle 1917 as a potential chassis for osmolality biosensors in the gut**

and submitted in partial fulfillment of the requirements for the degree of

Master of Science (Biology)

complies with the regulations of this University and meets the accepted standards with respect to originality and quality.

Signed by the final examining committee:

_____Chair
Dr.

_____Examiner
Dr. Vincent Martin

_____Examiner
Dr. Stephanie Weber

_____Examiner
Dr. Elena Kuzmin

_____Supervisor
Dr. Laurent Potvin-Trotier

Approved by

_____Graduate Program Director
Dr. Robert Weladji

_____Dean of Arts and Science
Dr. Pascale Sicotte

Date:_____

Abstract

E. coli Nissle 1917 as a potential chassis for osmolality biosensors in the gut

Maria T. Orozco Hidalgo

The human gut is a heterogeneous environment. Diseases like inflammatory bowel disease (IBD) modify the physical properties of the gut, such as osmolality. These changes are thus desirable biomarkers for personalized diagnosis and treatment. Current diagnostic tools are invasive and insufficient to precisely detect changes of the physical environment. Likewise, disease heterogeneity hinders final diagnosis, showing the importance of creating personalized and sensitive diagnostic tools. For these reasons, its necessary to develop clinically relevant technologies that can safely and accurately report on these physical changes across different regions of the human gut. Extensive research on the human microbiome has revealed that microbes are able to sense shifts in the gut's physical properties, making them strong candidates to report on these novel biomarkers. Furthermore, advances in synthetic biology have allowed the creation of microbial whole-cell biosensors that robustly report disease biomarkers in the human gut. Therefore, this thesis shows the potential of the probiotic strain *Escherichia coli* Nissle 1917 (EcN) as a chassis for gut osmolality biosensors. Here, RNA-seq and differential gene expression analysis were used to filter and compare genes that strongly and exclusively respond to different osmolality levels relative to general stress conditions. It was found that five promoters met the conditions, nevertheless, there was cross-reactivity within levels of osmolality and with other general stress conditions. Interestingly, some of the selected promoters had not been shown to react to elevated osmolality conditions, hinting at differences between EcN and other *E. coli* strains. Based on this, further experimentation is necessary to validate the activity of these promoters in the conditions of interest. Taken together, this work provides a starting point for gut osmolality biosensors using the probiotic strain EcN, providing more options for building biosensors of gut biomarkers.

Acknowledgments

First, I would like to thank my parents Adriana and Luis German for their unconditional support on this journey. They have stood by me through every decision and all the ups and downs. I feel so lucky and proud to be your daughter.

I want to thank my friend Laura Camelo for being my chosen family during this time. You listened to my endless talks about science, academia, and life in general. I couldn't be happier to have randomly met you almost two years ago, and can't wait to share more experiences together, amiga del alma.

I am extremely grateful for the support I received from my community in Montreal, especially from J, Danna, Zineb, Daniele V, Michael, Anshul, Maria Paola, and Ugo. Thank you for your friendship, late nights out, coffee, outdoor adventures, dance parties, karaoke nights and endless conversations. I'm also grateful for the presence of my cousin Carolina in my life, you've been a constant guide at a professional and personal level.

I would also like to thank my lab mates Tina, Paige, Saba, Felipe, Maude, Pierre, and Jylar for encouraging talks, lunches, and support.

This work wouldn't have been possible without the SynBioApps NSERC CREATE Fellowship and the Weston Family Foundation Catalyst grant.

Finally, I would like to thank Dr. Laurent Potvin-Trottier for his supervision. Special thanks to Dr. Carolina Tropini and Dr. Steph Weber for their support.

Author contributions

The EcN biosensor project discussed in Chapters 1, 2, 3 and 5 of this thesis was conceived by Dr. Laurent Potvin-Trottier, Dr. Mina Hoofar from the University of Victoria (UVic), and Dr. Carolina Tropini from the University of British Columbia (UBC). The scripts for bacterial growth analysis were provided by Dr. Carolina Tropini. The protocols for RNA extraction and scripts for differential gene expression analysis were provided by Juan Camilo Burckhardt from the Tropini lab at UBC. All the RNA-seq library preparation and sequencing were done at the UBC Sequencing+Bioinformatics Consortium. This research was supported in part by computational resources and services provided by Advanced Research Computing at UBC. All experiments were designed, performed, and analyzed by Maria T. Orozco Hidalgo.

The prion propagation project discussed in Chapters 2, 4 and 5 is part of a research manuscript submitted for publication at the time of the defense of this thesis. It was co-first authored by Krista Jager and Maria T. Orozco Hidalgo, alongside Benjamin Lennart Springstein, Euan Joly-Smith, Fotini Papazotos, EmilyKate McDonough, Eleanor Fleming, Giselle McCallum, Andreas Hilfinger, Ann Hochschild, and Laurent Potvin-Trottier. Here, Maria T. Orozco Hidalgo helped to write the manuscript, produce figures, and performed experiments shown in Figures 3, 4, S1, S6, S7, S8, and S11.

Krista Jager[†], Maria Teresa Orozco-Hidalgo[†], Benjamin Lennart Springstein, Euan Joly-Smith, Fotini Papazotos, EmilyKate McDonough, Eleanor Fleming, Giselle McCallum, Andreas Hilfinger, Ann Hochschild, Laurent Potvin-Trottier. Measuring prion propagation elucidates mechanism of loss. bioRxiv 2023.01.11.523042; doi: https://doi.org/10.1101/2023.01.11.523042

[†]These authors contributed equally to this work

Table of contents

List of Figures

Chapter 1

Chapter 3

Chapter 4

List of Tables

Chapter 1: Introduction

1.1. The gut's physical environment

The human gastrointestinal tract (referred to as the human gut in this thesis) is a highly heterogeneous and complex environment[1]. It harbours the gut microbiome, a collection of protozoa, archaea, eukaryotes, viruses, and bacteria that live in close association with their host[2]. Thanks to advancements in meta-genomics and sequencing technologies, the gut microbiome has been largely researched and was found to play a role in nutrient metabolism, immunomodulation, gut health, and disease, among others[3]. Due to the increased interest in this subject, many studies have focused on understanding the identity and distribution of the microbial populations along the gut[4]. Although microbiome distribution is a multifactorial process, it is largely governed by the changing physiological conditions along the gut and its microhabitats[4]. Of special interest are the physical conditions, understood as environmental factors that lead to physical forces. These include pH, osmolality, oxygen concentration, flow and mucus thickness, among others[1].

Extensive research has allowed the partial characterization of these physical conditions and their impact on the microbiome of healthy mammalian guts. For instance, it has been observed that the mammalian small intestine is more acidic and has higher levels of oxygen than other parts of the lower intestinal tract, stimulating the growth of bacterial species that can grow in these conditions (**Figure 1a**)[4,5]. Also, the gut epithelium has a complex topology, where cells are organized into villi and crypts[6] (**Figure 1**). Here, there is a shift of physiological conditions like oxygen concentration and mucus thickness of the small intestine and colon, giving rise to distinct microbial communities[7].

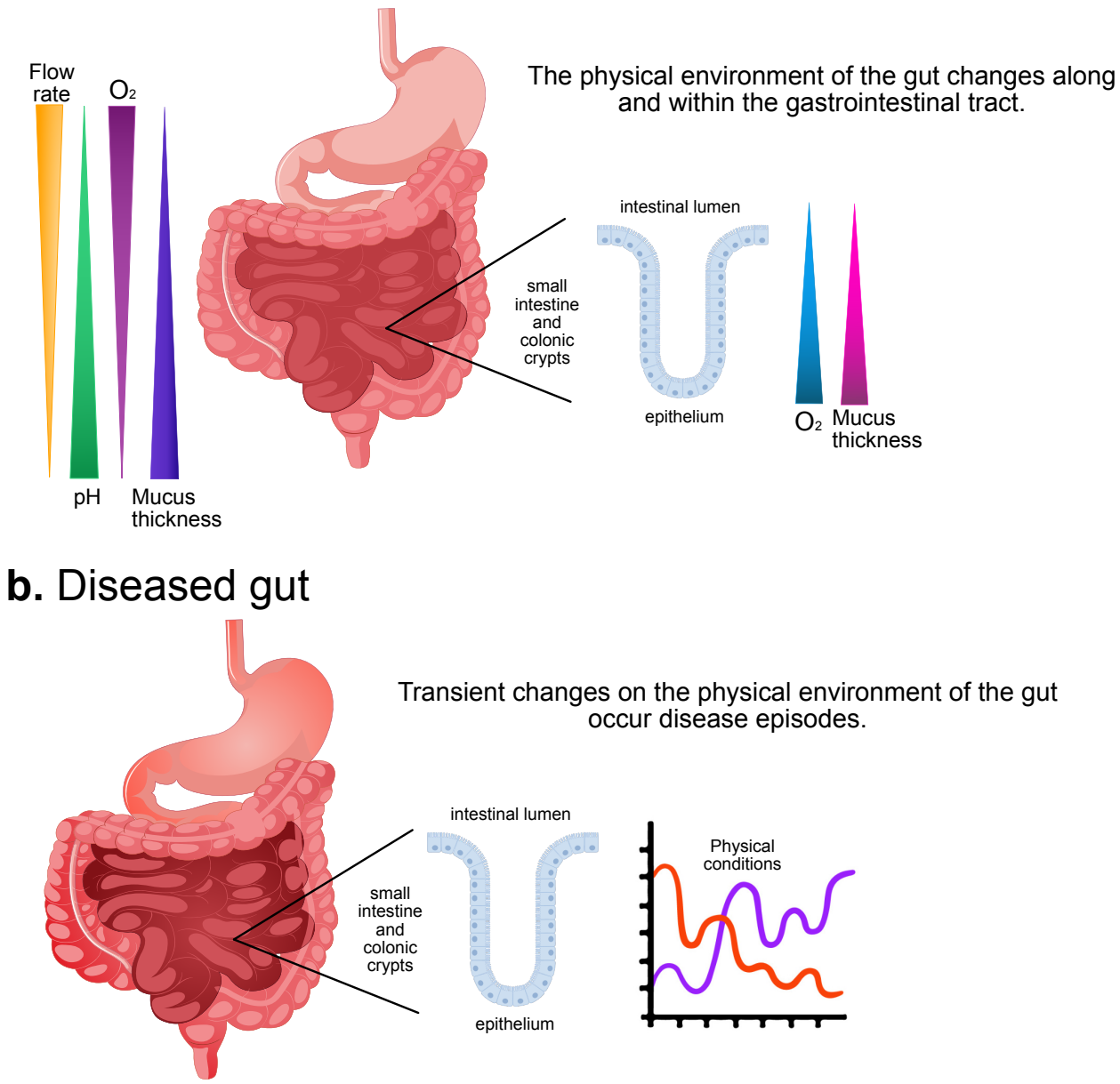

Figure 1: Schematic of the physical environment of the gut. Some of the physical properties of the **a)** healthy, and **b)** diseased gut are shown.

The physical environment of the gut has also been observed to shift during disease episodes at a transient or generalized level (**Figure 1b**)[1]. For example, inflammatory bowel disease (IBD) patients present variations in pH across the gut[8], while osmolality and flow change due to diarrhea[9,10].

1.2.Gut osmolality

Osmolality (mmol/L) and osmolality (mOsm/Kg) refer to the concentration of solute particles in a solution[11]. They differ from each other in that osmolality considers the mass of the solute (Kg), instead of its volume (L). Since mass is independent of temperature, osmolality is the preferred measurement in biological systems[12].

In the context of the gut, osmolality constantly changes due to the absorption and secretion of water and luminal contents by the epithelium[13,14]. Furthermore, transient osmolality changes occur during osmotic diarrhea episodes[15]. Here, non-absorbed solutes will cause water efflux from the intestine's epithelial cells into the lumen, increasing intestinal motility[16]. This condition arises during laxative consumption[16] or diseases like lactose intolerance, celiac disease, and pancreatic cancer[15].

As previously established, the gut microbiota's distribution is tightly regulated by the physical conditions of the gut, including osmolality. Different bacterial communities are able to sense and respond to these changes[4]. During transient osmotic perturbations, microbiota composition is dramatically modified[10], potentially causing long-term health problems to its host. This highlights the importance of this physicochemical parameter as a biomarker of gut and microbiota function.

1.3. Bacterial osmoadaptative response

The bacterial response to osmolality has been well documented in model organisms like *E. coli*[17,18], elucidating that osmolality shifts can lead to changes in osmotic pressure[19]. It has been shown that the integrity and hydration of cell compartments are dictated by osmotic pressure[20]:

- When it decreases, water influx, swelling, or lysis occurs.
- When it increases, water efflux and dehydration occur.
- Optimal: bacteria keep an osmotic pressure of 1 atm inside the cytosol, avoiding cell lysis and maintaining a rigid membrane[21].

At a physiological level, bacterial growth is affected by osmolality changes[22]. Properties like cell volume and turgor pressure are affected by external osmotic pressure[23]. To cope with these changes, bacteria are equipped with osmoadaptive mechanisms that are mainly regulated at the transcriptional level[24]. The most studied mechanism during high osmotic pressure is the accumulation of solutes via membrane channels and protein pumps. The response to this condition has two stages, first import of K^+ ions into the cytoplasm; followed by the import/synthesis of compounds like proline, glycine betaine, carnitine, and glutamate among others[18,24]. These compounds are known as compatible solutes or osmoprotectants because they don't disrupt vital cellular processes and aid in the stabilization of enzymes and proteins under high salinity

environments[18]. The genetic and biochemical elements that mediate osmoadaptation vary between taxonomic groups, resulting in a variety of responses to this condition[24]. In E. coli, it is known that osmoresponsive systems like TrK (membrane K+ transporter)[25], Kup (major K+ transporter)[26], Kdp (high-affinity transporter of K+)[27] participate in the uptake of K+ ions; while systems like ProU (glycine betaine and proline ABC trsnsporter)[28] and BetT (choline transporter)[29] are responsible for importing compatible solutes.

1.4. Gut diseases and osmolality

Human gut diseases heavily change the gut's physical environment by disrupting natural conditions, including osmolality. It has been observed that malabsorption due to intolerances, like celiac disease or lactose intolerance, could lead to changes in gut osmolality[30,31]. Similarly, IBD patients exhibit varying levels of gut osmolality during diarrhea episodes[32,33].

The rising incidence of gut diseases in the global population and their difficult diagnosis pose a burden on health care systems[34–38]. This calls for research on the characterization of the gut and the development of precise diagnostic tools.

1.5. Biosensors

Clinicians use techniques such as colonoscopy and endoscopy to diagnose and monitor gut diseases[39]. These techniques are not able to reach all gut locations, and they disrupt the local environment due to their extensive prep[40,41]. Hence, there is a gap in our ability to measure gut properties precisely.

An alternative to traditional techniques is the use of biosensors. By definition, a biosensor is a device that measures reactions by generating signals proportional to the concentration of a product or analyte in a reaction (biological or chemical). Biosensors should be selective, reproducible, stable, and sensitive[42]. Typically, biosensors have four parts:

1) Bioreceptor element, which are biological elements (antibodies, organelles, enzymes, whole-cells, DNA, nanoparticles, among others) that interact with the analyte or product[42,43].
2) Transducer element, which detects the signal emitted by the bioreceptor and transforms it into a measurable signal (electrical, optical, etc). Examples of this could be electrodes or spectrophotometers, among others[44].
3) Electronics, consisting of an electronic circuit that conditions or prepares the signal from the transducer. Signaling conditioning entails signal amplification or conversion from analogue to digital form[42].
4) Display, formed by software and hardware elements that quantify the signal and display it in a friendly user manner. Examples of this are graphics, images, or numeric tables[42,43].

These devices have been employed for a variety of applications; for instance monitoring of environmental conditions[45], food quality[46], disease[47] and presence of toxins[48], among others[49]. More recently, advances in microbiology and synthetic biology have boosted the development of microbial biosensors[50]. These systems use the whole microbial cell (commonly bacteria) as the bioreceptor element, taking advantage of the vast collection of metabolic pathways and biomolecules that allow the organisms to respond to a range of environmental stimuli[51].

A constraint of these systems has been achieving precise sensing given the complexity of these biological 'factories'[52]. Nevertheless, synthetic biology advances have allowed the design of genetic circuits that precisely detect a variety of molecules[53–55]. Based on this, biosensors have been proposed as tools to characterize complex environments such as the mammalian gut[56,57].

1.6. Microbial biosensors for the gut

Microorganisms interact intimately with the human body[58], surviving and sometimes thriving by responding to environmental cues with their versatile genetic and biochemical machinery[55]. Of special interest is the gut microbiome[59], where metagenomic studies have revealed that different microorganisms are able to colonize the different niches along the mammalian gut, revealing their capacity to interact and sense a variety of environmental signals[4]. It has also been observed that these microbes respond to local and transient shifts of these signals[10], making them excellent candidates to report on gut function[57].

As previously mentioned, the development of genetic engineering and microbiology have allowed the construction of whole-cell biosensors, where complex genetic circuits proportionally respond to relevant gut biomarkers (**Figure 2**). These sensors are composed of three key elements[57]:

1) Sensory element: bacterial sensing and signaling pathways can be one-component (OCS) or two-component systems (TCS)[60]. OCS are transcription factors that directly bind to the ligand of interest (environmental stimuli) and activate/repress gene expression[61]. On the other hand, TCS consists of membrane-bound histidine kinases that generate a phosphorylation cascade in response to environmental stimuli. This cascade activates transcriptional factors that in turn activate/repress gene expression[62].
2) Processing element: circuits that determine if an input was detected and what kind of output will be produced. They could be binary (input is present or not), analogue (how much of the input is present) or recording an input throughout time[57]. For instance, Boolean logic gates can be used to determine which combination of inputs produces a determined output[60,63,64]
3) Actuator element: this is the output of the whole-cell biosensor. Bacteria can rapidly report on an input via luminescence, fluorescence, or colorimetric reporters[57]. They can also

record an input over time via DNA memory circuits, for instance, recombinase-based or transcriptionally-based DNA writing methods[65].

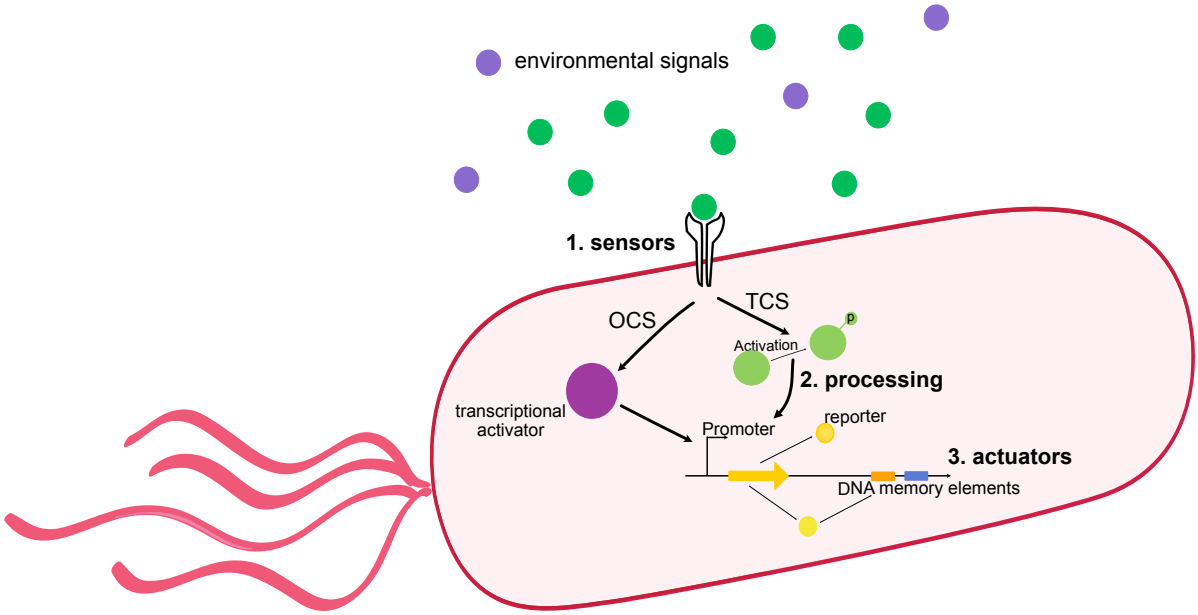

Figure 2: General schematic of a bacterial biosensor. 1) Sensory element which could be a one component system (OCS) or two component system (TCS), 2) Processing circuit which transfer signal to 3) actuator elements that transform the signal into a detectable output.

Taken together, these elements allow for the successful reporting of gut activity in a non-invasive manner. This technology navigates different niches along the gut (normally unreachable by current technology), reports and records transient signals, and is finally collected for analysis. Overall, these characteristics make it a desirable alternative to invasive and disruptive diagnostic options[41,66,67].

To date, there is a good amount of work showcasing the efficacy of these systems *in vitro* and *in vivo* (**Table 1**). Foundational work has been done in developing biosensors for inflammation, given that is an important biomarker for IBD diseases[68] and depression[56]. For instance, researchers engineered nitric oxide (NO) detection into *E. coli* using a bidirectional fluorescent reporter driven by the switch of *fimS* orientation, a native and heritable mechanism present in native fimbrae phase variation[69]. Likewise, NO detection was engineered using the *norRVW* operon in *E. coli* Nissle 1917 (EcN), where the expression of the norR regulatory element was tuned via promoter optimization and feedback loop design[70]. Furthermore, thiosulfate and tetrathionate sensing has

been engineered in *E. coli* using the TtrSr two-component system[71]. When paired with a transcriptional memory element the sensing was stable and functional over time[72].

Other properties, like pH, oxygen, lactate and biliary acids, can be considered biomarkers of gut function and help characterize the different niches along the gut (**Table 1**). For example, researchers engineered EcN to grow exclusively in certain regions of the gut based on the detection of oxygen, lactate, and pH[73]. Here, they paired logic gates with: a hypoxia promoter based on the expression of FDR in the absence of oxygen, the *lldPRD* operon from the lactic acid fermentation and a membrane bound protein CadC that is sensitive to acidic pH[73].

Host	Target	Output	Physiological relevance	Mechanism	Ref
E. coli Nissle 1917 and mini SimCells	Nitric oxide (NO)	GFP fluorescence	Biomarker of many chronic inflammatory diseases and cancers.	Engineered *norRVW* operon: promoter tuning and addition of a positive feedback loop.	[70]
E. coli Nissle 1917	Nitrate and thiosulfate	GFP fluorescence	Biomarker for inflammation. Used in a model for colitis in mice.	Engineered *narX-narL* circuit. Use of boolean gates.	[74]
E. coli NGF-1	Tetrathionate	β-galactosidase	Biomarker for inflammation.	*ttrR/S* and PttrBCA drive Cro 'trigger' expression to switch a phage- lambda- memory circuit	[72]
E. coli Nissle 1917	Thiosulfate and tetrathionate	GFP fluorescence	Biomarker for inflammation.	Engineered TtrSR two-component system (TCS)	[71]
E. coli Nissle 1917	Oxygen, pH and lactate	GFP fluorescence	Physiological indicators of different microenvironments of the gut.	-Oxygen: pPepT promoter. -Lactate: constitutive production of an LldR repressor. -pH: pCadC system. -AND logic gates controlling bacterial replication	[73]
E. coli strain EA3020	Nitric oxide (NO)	YFP (OFF state) and CFP (ON state) fluorescence	Biomarker for inflammation.	Bidirectional fluorescent reporter switch fimbriae (Fim) phase variation system. Inversion of *fimS* by the DNA recombinase FimE.	[69]
E. coli Nissle 1917	pH, oxygen, lithocholic acid (2ndary), deoxycholic acid	mCherry fluorescence	Relevant compounds and conditions found in the human GI tract.	Engineered pMUT plasmid with environmentally responsive promoters driving GFP expression: -pH: activation of pCadC	[75]

	(2ndary, taurocholic acid (primary), caffeine, lactate, acetoacetate			-oxygen: repression of pF8 -2ndary bile acids: activation of pVtrA -Primary bile acids: activation of pTcpP -caffeine: activation of pCaf -lactate: activation of pLac -Acetolactate" activation pf pAto	
E. coli MG1655	Bacterial replication (cell division)	Count of bacterial generations by RINGS method based on colony fluorescence due to the triple reporter system (repressilator)	Bacterial growth rate in the mammalian gut	Use of the repressilator circuit.	[76]
B. thetaiotaomicron VPI-5482	Arabinogalactan, chondroitin sulfate, IPTG, rhamnose	Luminescence (luciferase activity)	Generating a synthetic biology toolbox to engineer this organism for applications in the murine gut.	-Library of biological parts, comprised of constitutive promoters, inducible promoters, and RBSs -CRISPRi for regulated knockdown of recombinant and endogenous gene expression -Recombinase based memory systems.	[77]

Table 1. Literature review of studies on engineered bacteria that report on gut function. The selected studies include testing of biomarkers of interest *in vivo*.

1.6.1 Probiotic organisms used as chassis of biosensors

As it has been shown, most of the work has been done in an *E. coli* chassis. Given the ample knowledge, genetic stability, and availability of genetic tools for this organism, it is a good starting point for developing these technologies[55,78]. Moreover, several studies use a probiotic *E. coli* strain known as Nissle 1917 (EcN). One study found significant differences between EcN and other well-studied E. coli strains like MG1655 and BL21; these differences are mainly related to iron transport systems and the arginine deiminase pathway[79]. The same study showed that EcN and the other strains have comparable activity of the central metabolic pathway[79], making it feasible to leverage certain gene expression studies from MG1655 and BL21 to engineer EcN[80]. In addition to the benefits of using a model organism, EcN has been safely used in several clinical applications, which makes it a feasible option from a regulatory point of view[80]. This chassis has shown to promote intestinal barrier function[81], stimulate anti-inflammatory activity[82] and impede growth of opportunistic pathogens through the production of iron-scavenging siderophores and microcin proteins[83]. Additionally, this strain does not colonize the gut over log periods of time[84], which is a positive feature for biosensors collected and analyzed in the stool of patients.

1.7. Thesis Objectives

As it has been established, there is a need to develop technologies that enable the interrogation of the physical environment of the gut to better understand this environment during disease. As an alternative, bacteria are being engineered to report on gut function[57,60]. To date, there are no tools that precisely report on local osmolality shifts in the gut, a key property to understanding this environment. Based on this, the purpose of this thesis was to characterize *E. coli* Nissle 1917 (EcN) as a chassis for osmolality biosensors. This probiotic strain is genetically tractable, does not colonize the gut, and has a long history of safe applications in humans[80]. This makes it a desirable chassis for gut biosensors. Furthermore, it has been shown that there are significant genetic differences between laboratory strains and EcN[85], highlighting the importance of studying the osmotic response of EcN separately.

To accomplish this, the transcriptional responses of EcN to different osmolality conditions and general stress were analyzed in **Chapter 3**. With this information, five promoters were selected as candidates for biosensor development. In the future, these promoters will be validated *in vivo* and further paired with stable fluorescent proteins (FPs) and genetic memory elements to report on local osmolality changes along the gut. To achieve precise measurements, signal uniformity within the clonal EcN population is necessary to avoid stochastic noise due to heterogeneous responses to environmental stimuli[86]. In the long term, these biosensors would be encapsulated, released in the human gut, collected from the stool of patients and analyzed by clinicians to diagnose conditions and personalize microbiome interventions. This project was part of a broader collaboration with Tropini lab at the University of British Columbia (UBC) and with the Hoofar

lab at the University of Victoria (UVic). The UBC team will build the biosensor in *Bacteroidetes tethaiotamicron* (a common member of the human commensal microbiota) and conduct *in vivo* mouse experiments. The UVic team will develop a microfluidic-based encapsulation system for targeted delivery of the engineered probiotics into the different sections of the mouse gut for the *in vivo* mouse experiments.

Simultaneously, single cell heterogeneity was studied in bacterial prions. In **Chapter 4,** a submitted manuscript shows how time-lapse microscopy and microfluidics elucidate the mechanism of loss in single cells of model bacteria.

Chapter 2: Materials and methods

2.1. Bacterial growth and kinetics

E. coli Nissle 1917 was purchased from Ardeypharm. To start bacterial cultures, a glycerol stock was streaked overnight in a LB agar plate, producing single colonies after incubation at 37°C. Overnight 5 ml cultures were started from the singles colonies in LB media at 37°C with constant shaking (150 rpm). After 16h, OD600 measurements were performed in a TECAN Infinite M200 instrument. From these cultures, bacteria were diluted to 0.1 OD with LB media or LB conditioned media (specified below) according to the condition being assayed. The diluted cultures were placed in a 96 well plate (200 ul per well) in triplicates for each condition. The plate was later loaded into a Biotek Synergy H1 plate reader. The instrument was set to record the OD600 every 5 min during 24h, continuous orbital shaking, and incubation at 37°C (unless otherwise stated). With the collected data, growth kinetics were constructed using MATLAB to plot OD over time. To account for variability, each condition had three biological replicates which were averaged, showing the standard deviation as a shaded area. For every condition, the doubling time (dt) was calculated in the exponential growth phase using the following formula:

$$Doubling\ time\ (dt)\ = \frac{time\ (min) \times ln(2)}{ln(\frac{max\ OD600}{min\ OD600})}$$

2.2. Osmolality and stress conditions

In order to measure the effect of different compounds (osmolytes) and different levels of osmolality, the bacteria were grown in LB conditioned media (media+osmolyte). For each condition, a plain LB condition was included for control (osmolality of ~300 mOsm/kg). The osmolytes assayed, and their respective osmolalities, can be found in **Table 2**. To discern between the osmolality specific response and the general stress response, the bacteria were exposed to general stress. The details for this can be found in **Table 3**.

Osmolyte	Osmolality (mOsm/kg)
Sodium Chloride (NaCl)	339, 528, 712, 902
Sorbitol	332, 433, 522, 612, 721, 828, 929, 1050
Lactulose	339, 427, 536, 637, 760, 899
PEG	300, 700, 900

Table 2. Osmolality conditions assayed in EcN.

Type of stress	Details
High temperature	42°C
Acidic pH	pH adjusted to 5.8 with HCl
Oxidative stress	100 uM of oxygen peroxide (H_2O_2) added to LB media prior to starting the experiment.

Table 3. General stress conditions assayed in EcN.

2.3. Bacterial growth and preparation for RNA extraction

To prepare the cells for RNA extraction, a 5 ml LB culture of EcN was started overnight as explained above. After obtaining the OD600, the cells were diluted to OD 0.1 in LB media or LB conditioned media (see section below) to a final volume of 5 ml. This was done in triplicates for each condition (**Table 4**). These diluted cultures were incubated at 37°C (unless otherwise stated) and constant shaking of 150 rpm for 2 to 4 hours, depending on the time it takes to reach the exponential or stationary phase. For this step, the growth kinetics produced before were used as a guide. Finally, OD600 measurements were done and recorded at the end of each incubation period.

2.4. Conditions for RNA extraction

According to the growth kinetics data and previous studies on gut osmolality[32,33], it was decided to extract bacterial RNA in low/normal (reference condition), medium and high (perturbed conditions) osmolality levels. For all of the conditions, including the general stress, the RNA was extracted in exponential phase, nevertheless, RNA was also extracted in stationary phase in the control condition and in a high osmolality condition (NaCl). This was done to account for genes being exclusively expressed during this growth phase. A complete summary of the conditions can be found in **Table 4**.

Osmolyte/stress condition	Osmolality (mOsm/kg)	Growth phase
Sodium Chloride	712, 902	Exponential, stationary (high osmolality)
Sorbitol	721, 929	Exponential
Lactulose	760, 899	Exponential
PEG	700, 900	Exponential
No osmolyte - control	~300	Exponential, stationary
High temperature (42°C)	~300	Exponential
Oxidative stress (100 uM of H_2O_2)	~300	Exponential
Acidic pH (5.8)	~300	Exponential

Table 4. Growth conditions for RNA extraction.

2.5. RNA extraction

For all RNA manipulation, the area of work was decontaminated with 70% ethanol and RNAse Away reagent. The disposable material used was DNAse and RNAse free. Bacteria were harvested according to the conditions stated in **Table 4**. Bacterial lysis was done following the protocol for Enzymatic Lysis of bacteria found in the RNAprotect Bacteria Reagent Handbook by Qiagen. In this process, RNA protect (Qiagen), lysozyme (15 mg/ml) (NEB) and 2-Mercaptoethanol (Milpore Sigma) were used. To purify RNA from the bacterial lysate, the RNAeasy Mini kit (Qiagen) was used. After final elution in RNAse-free water, the concentration and quality of genetic material was determined using spectrophotometry with a TECAN plate reader instrument. If the sample had over 50 ng/ul of RNA, the TURBO DNA-free kit (Thermo Scientific) was used according to manufacturer's specifications.

2.6. RNA quantification and quality control

After the DNAse treatment, the concentration of RNA in the sample was recorded as explained above. Samples were stored at -80°C until further analysis. To confirm RNA integrity, a non-denaturing RNA gel was run for all the samples. To do this, the ssRNA ladder (NEB) and RNA loading dye 2X (NEB) were used. Additionally, all the samples were quality checked in a 2100 Bioanalyzer Instrument (Agilent Technologies) prior to RNA sequencing.

2.7. RNA sequencing (RNA-seq)

Sample preparation and RNA-seq was done at the UBC Sequencing + Bioinformatics Consortium at the University of British Columbia, Vancouver, Canada. In brief, the quality of extracted RNA was assessed using the BioAnalyzer RNA Nano Kit (Agilent) and quantity measured using the Qubit BR RNA Kit (Thermofisher). Libraries were prepared using 200 ng input RNA with the NEBNext Ultra II RNA Library Prep Kit according to manufacturer's instructions (NEB). Libraries were then pooled and sequenced on a NextSeq 2000 P3 lane to generate 1x50 bp reads. Raw base call data (bcl) were converted into FastQ format using the bcl2fastq conversion software from Illumina.

2.8. Data analysis

The quality of sequencing was assessed using FASTQC. An adapter version of the SAMSA2 pipeline[87], was used to: remove low quality sequences and trim adapter sequences from FASTQ files (Trimmomatic), remove rRNA reads from FASTQ files (SortMeRNA), annotate and generate counts using a generated *E. coli* Nissle reference database (DIAMOND).

The annotated data was analyzed using DESeq2[88]. Here, data is normalized and clustered (unsupervised). After this, a count matrix was generated for every gene in all of the conditions assayed. A shrinkage based on log2 fold changes was made. With this, a differential expression test was done. Here, the differences between treated (stressed), and untreated samples are identified. After this test, we filtered the genes that had a log2 fold equal or greater than 1, this allows us to keep the genes that were expressed 2 times or more in the treated conditions vs the untreated condition. In addition to this, we filtered genes that had an adjusted p-value equal to or lower than 0.05 to ensure that our data were significant. Using Venn diagrams, a comparison of which genes were being over expressed across all osmolality and stress conditions was made. The expression level of genes that were over expressed in all the conditions was shown using a heatmap. Distance between samples was shown with a PCA plot.

2.9. Materials and methods Chapter 4

Detailed Materials and Methods are available in the SI Appendix. The base strain used throughout the paper was *E. coli* MG1655. Prion formation was induced overnight by the production of the SSB PrDs fusion proteins and the New1 fusion protein with 10μM IPTG at 30°C. Cells were cured of the New1-containing plasmid by plating overnight at non-permissive temperature (37°C). These indicator plates contained X-Gal which enabled distinguishing colonies with prion-containing cells (dark blue). For the microfluidic experiments, dark blue colonies were grown overnight at 30°C and the cultures were inspected with fluorescence microscopy to confirm that the cells contained prion aggregates. These confirmed cultures were then loaded into the microfluidic device, where the cells were continuously fed a supplemented M9 growth medium. Multiple cell positions were

imaged in fluorescence every 8 min with a Zeiss Axio Observer at 63x, and the cell lineages were segmented and tracked as previously done.

Chapter 3: Characterizing *E. coli* Nissle 1917 (EcN) as a potential chassis for osmolality biosensors

3.1. Introduction

Extensive research on the human gut has revealed that it has a heterogeneous physical environment[1]. Diseases in the gut modify its physical properties, such as osmolality[32,33]. This parameter is thus a desirable biomarker to characterize the human gut, create personalized diagnoses and treatments. The invasive and non-specific nature of current diagnostic tools has boosted the creation of microbial biosensors to robustly report shifts inside the gut[40,41,57]. In this chapter, the potential of *E. coli* Nissle 1917 (EcN) as a chassis for gut osmolality biosensors was explored. To do this, the growth kinetics of EcN were determined under different osmolality and general stress conditions. Furthermore, gene expression was investigated in these conditions through transcriptomics. With this data, it was assessed which EcN genes are exclusively expressed during osmolality shifts. The promoters of these genes will serve as a starting step for osmolality biosensor development.

3.2. Objectives

1. Characterize EcN growth kinetics across a range of osmolalities and osmolytes relevant to gut diseases.
2. Analyze the transcriptional response of EcN with transcriptomics and differential gene expression.
3. Identify osmolality-specific EcN promoters across multiple high and medium osmolality conditions.

3.3 EcN is able to grow at different rates in different osmolytes and osmolalities

In order to evaluate EcN as a chassis for osmolality biosensors, we first characterized its growth in different osmolytes at different osmolalities (**Figure 3**). Different compounds can change the gut's osmolality, causing cells to increase their efflux of water. Even though the response mechanism could be the same, different conditions and doses could affect the cells differently, thus activating a variety of promoters.

Four compounds were selected for the analysis: two sugars/sugar-alcohol (lactulose and sorbitol), one polymer (PEG) and one salt (NaCl). These compounds are relevant because of their different effects on bacterial cells. For instance, salts could affect bacterial cell division[89], sugars could serve as an additional nutrient source for bacteria, and polymers can cause precipitation of the bacterial

membrane proteins[90]. Additionally, sugars are relevant in the context of the gut because they could be present as non-absorbed leftovers of food. Likewise, PEG is also relevant in this context because it's a widely used laxative[91].

To understand the response of EcN to different osmolytes and osmolalities, the growth kinetics of EcN were monitored at different osmolalities ranging from 300-1000 mOsm/kg (**Figure S2**). Once it was confirmed that the bacteria could grow in all compounds, high osmolalities (900 mOsm/kg) and medium osmolalities (700 mOsm/kg) were selected[32,33]. Furthermore, bacteria were grown in osmolyte-free rich media as a control (~300mOsm/kg). As the growth curves show, EcN is able to grow in the conditions assayed. As expected, an increase in osmolality imposes a penalty on doubling time (**Figure 3**). This is especially evident for the bacteria grown in PEG (**Figure 3a**), where the maximum OD reached was 0.3 and 0.2 for medium and high osmolality, respectively. From these data, it was inferred that EcN grows at different rates depending on the level of stress inflicted by higher osmolalities.

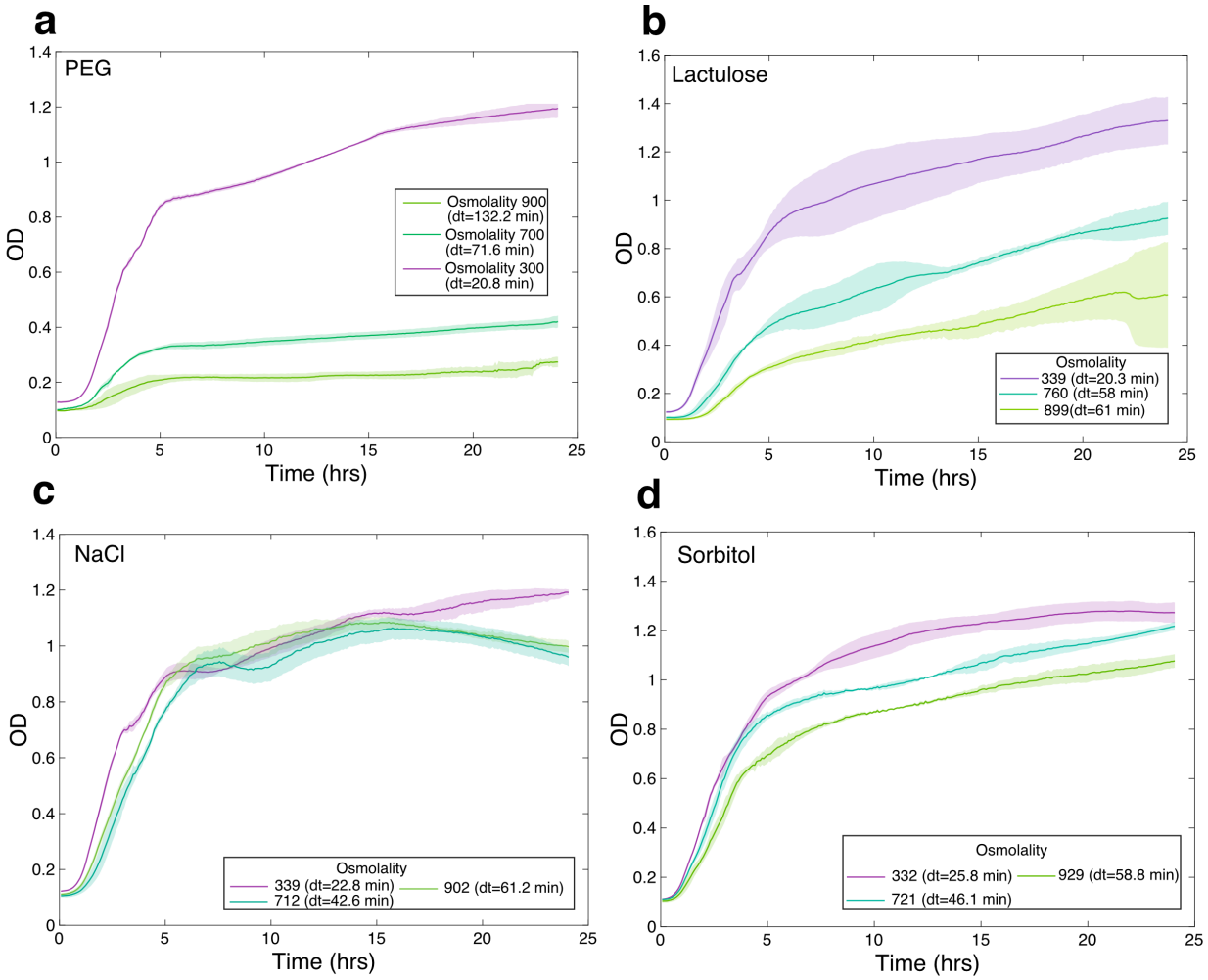

Figure 3. Growth curves (OD in function of time) of EcN in untreated (LB) and treated (LB+osmolyte) rich media. High (~900mOsm/kg) and medium (~700mOsm/kg) osmolality conditions were evaluated for the osmolytes: **a)** PEG; **b)** Lactulose; **c)** Sodium chloride (NaCl); and **d)** Sorbitol. Osmolality values are expressed in mOsm/kg. For every condition, 3 biological replicates were made. The curves represent the average of the replicates, while the shaded area represents the standard deviation. Doubling times (dt) at 37°C are shown for each condition.

The general stress response of bacteria is a well-studied subject, especially in *E. coli*[92,93]. In brief, it promotes survival under several environmental stresses encountered throughout bacterial growth and survival. It is known that these conditions result in the activation of small or large groups of genes that help the organism cope with stress[94]. Many of these genes are expressed under more than one type of stress, hence the name of general response.

In the context of this project, it is important to investigate if EcN has a specific response to osmolality conditions. An ideal gut osmolality biosensor chassis will exclusively respond to changes in osmolality, rather than other environmental stresses like pH or temperature. Considering the complex and heterogeneous nature of the gut, other physiological factors (environmental stresses for bacteria) fluctuate along the gut, disease episodes, or simply healthy

gut functioning[1]. For instance, during IBD inflammation episodes, pH along the gut could vary from acidic to alkaline or vice versa[8], while reactive oxygen species (ROS) could increase in concentration[95]. Also, during infections, patients could have elevated body temperatures[96]. As a control step for EcN's general stress response, bacterial growth was evaluated under three common general stress conditions: high temperature, acidic pH, and oxidative stress. The growth curves show the bacteria were able to grow in all the general stress conditions assayed (**Figure 4**). As expected, there was a penalty on doubling times compared to the control condition, more evident for the acidic pH (**Figure 4b**).

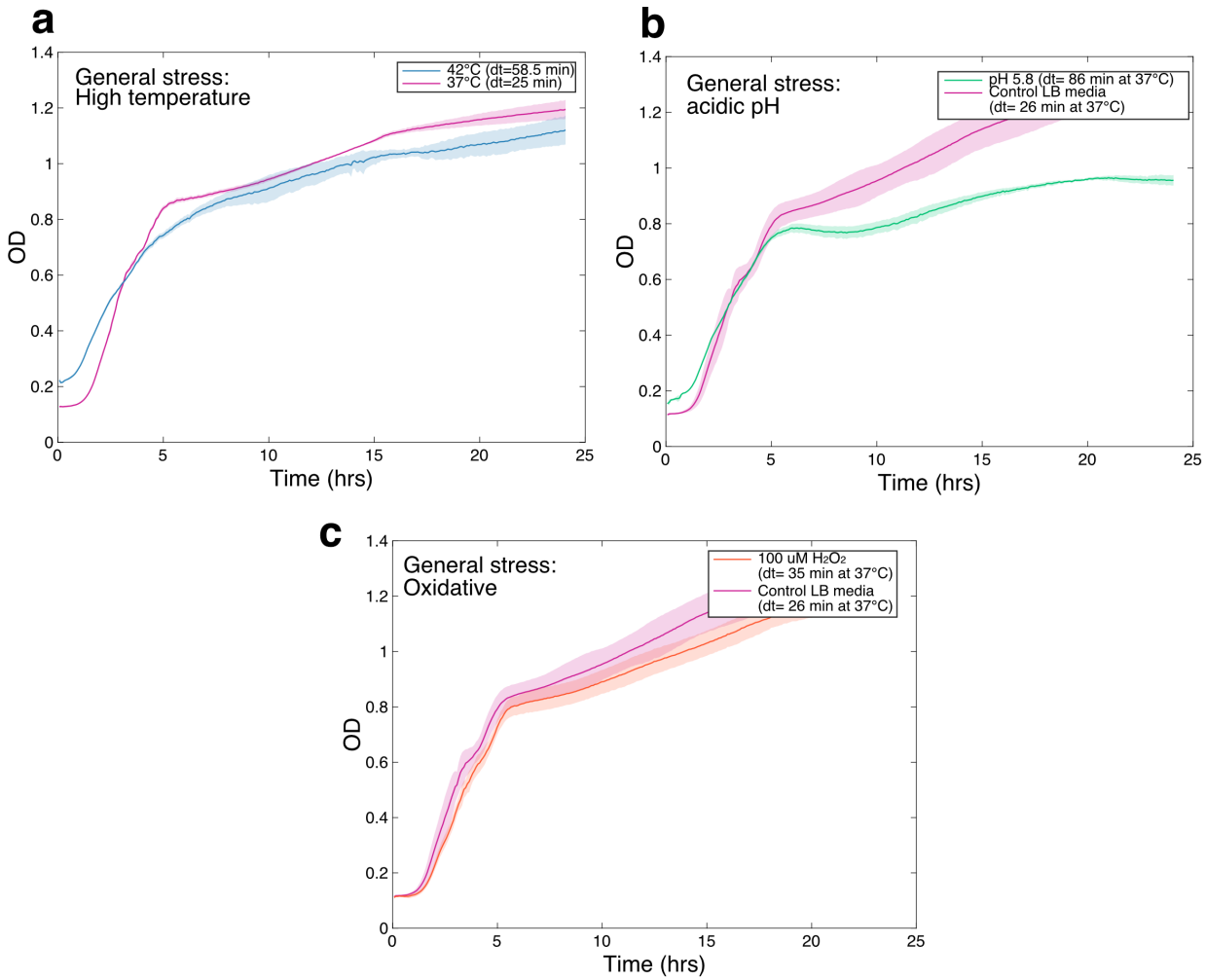

Figure 4. Growth curves of EcN (OD in function of time) in general stress conditions. In every condition, EcN was grown in rich media (LB) as a control. The conditions assayed were: **a)** High temperature (42°C); **b)** acidic pH (5.8); and **c)** oxidative stress (100 uM of oxygen peroxide). For every condition, 3 biological replicates were made. The curves represent the average of the replicates, while the shaded area represents the standard deviation. Doubling times (dt) for each condition are shown.

3.4. Some EcN genes have a specific response to different osmolality levels in rich media

3.4.1 Transcriptomic analysis of EcN

To uncover which genes were responsible for the survival of EcN under the osmolality and general stress conditions, transcriptomics (RNA-seq) were performed in all the conditions assayed above (**Table 4, Chapter 2, Materials and Methods**). Although the osmotic stress response of *E. coli* has been thoroughly characterized through gene expression studies, this has been done using compounds such as NaCl, glycine, and sorbitol in the common laboratory strain of *E. coli* MG1655[97–100]. An ideal and simplified approach would be to use the existing literature to select the desired promoters and interrogate their expression in the presence of different osmolytes (at different osmolality levels) through a fluorescent reporter in a high throughput manner. Unfortunately, there is no available data on EcN response to these conditions. Furthermore, it has been reported that the EcN strain has more than 1,000 unique coding sequences (CDSs) when compared to the MG1655 strain[85] (**Figure S1**), opening the possibility of discovering unique EcN genes being over expressed during osmotic stress events.

In order to identify genes involved in the osmolality (700 to 900 mOsm/kg) and general stress response (pH, temperature, oxidative stress), EcN was grown using the data from the growth kinetics (**Figures 3** and **4**). Subsequently, RNA was extracted, sequenced and annotated with the EcN genome as a reference using the SAMSA2 pipeline[87] (**Chapter 2, Materials and methods, sections 2.5-2.8**). In all the conditions assayed, RNA was extracted during the exponential growth phase. Given the complexity of bacterial growth in the gut, it is relevant to investigate EcN's osmolality response during stationary phase, thus RNA was extracted in this phase in rich media (base) and rich media with NaCl at high osmolality (~900 mOsm/kg).

In every condition, the sequenced reads are annotated using the EcN genome as a reference. This generates a count matrix of all the genes identified (**Chapter 2, Materials and Methods, sections 2.7 and 2.8**). For all conditions, three biological replicates were made. With these, a principal component analysis (PCA) plot was generated in order to visualize and determine the variability between samples (**Figure 5**). PCA plots simplify multidimensional data by constructing lower dimensions called principal components (PCs), in this case PC1 and PC2 were presented to visualize the dimensions where most variability occurs[101]. In the context of this project, determining variability is important to confirm that the treated conditions (osmolality and general stress) are different from the base condition (control) due to different gene expression profiles. As a general statement, the plot shows there are different degrees of variability between all the treated conditions and the base condition (red) (**Figure 5**). Biological replicates (shown in the same color) are close to each other, compared to the different conditions, showing the reproducibility of the assay. The highest degree of variability occurs between the base condition (red) and certain high

& medium osmolality samples (**Figure 5**), hinting that bacterium in these samples presented elevated levels of stress. It is also observed that the high temperature, oxidative stress, and stationary phase conditions are close together (**Figure 5**), hinting at a potentially similar gene expression profile. Similarly, the acidic pH and stationary phase with high osmolality stress (turquoise) conditions are also in proximity.

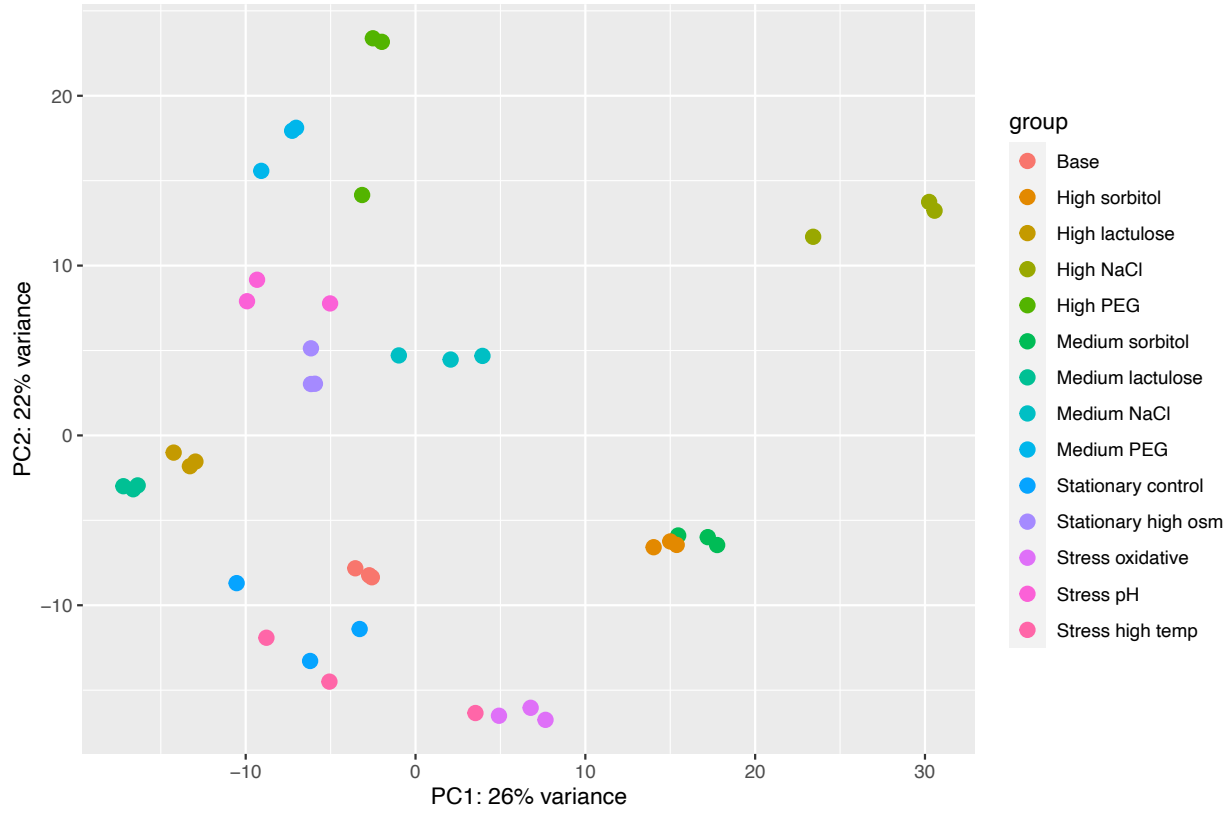

Figure 5. Principal component analysis (PCA) plot showing variability between all the samples in two dimensions. Each individual sample is represented by a colored circle corresponding to the conditions displayed on the right-side legend. For every condition, 3 biological replicates were made. The dimensions used are PC2: 21% variance and PC1: 25% variance.

3.4.2 Differential expression analysis of EcN's osmolality and general stress response

After visualizing and determining the variability of the data, a differential gene expression analysis was made using the DESeq2 framework[88] (Chapter 2, Materials and Methods, 2.8). This determined the fold increase of the treated samples (osmolality and general stress) compared to the base level sample (untreated rich media). This analysis results in log2 fold increase values for each gene detected in every condition assayed. Each gene has a p-value and adjusted p-value that represent the significance of the differential gene expression analysis[102]. To control variability in

low count genes, a Shrinkage of effect size was performed (**Figures S3** and **S4**). The shrunken values were used in downstream analysis[88].

To investigate which genes could potentially serve as osmolality biosensors in the gut, an independent filtering was done on all the conditions assayed to obtain genes overexpressed at least two times compared to the base condition (Chapter 2, Materials and Methods, 2.8). It is important to investigate if there are genes being over expressed in all the conditions of osmolality in order to build a robust biosensor. Osmolality shifts could come from different sources in the heterogeneous and complex environment of the gut. Therefore, high osmolality conditions and medium osmolality conditions were separately compared using Venn diagrams. There were 36 genes over expressed in all of the high osmolality conditions (**Figure 6a**), and 31 genes over expressed in all of the medium osmolality conditions (**Figure 6b**). To find the common genes between these two groups, another Venn diagram was made (**Figure 6c**). Here, it was shown that 22 genes are over expressed at high and medium osmolalities, 14 genes in high osmolality, and 9 genes in medium osmolality.

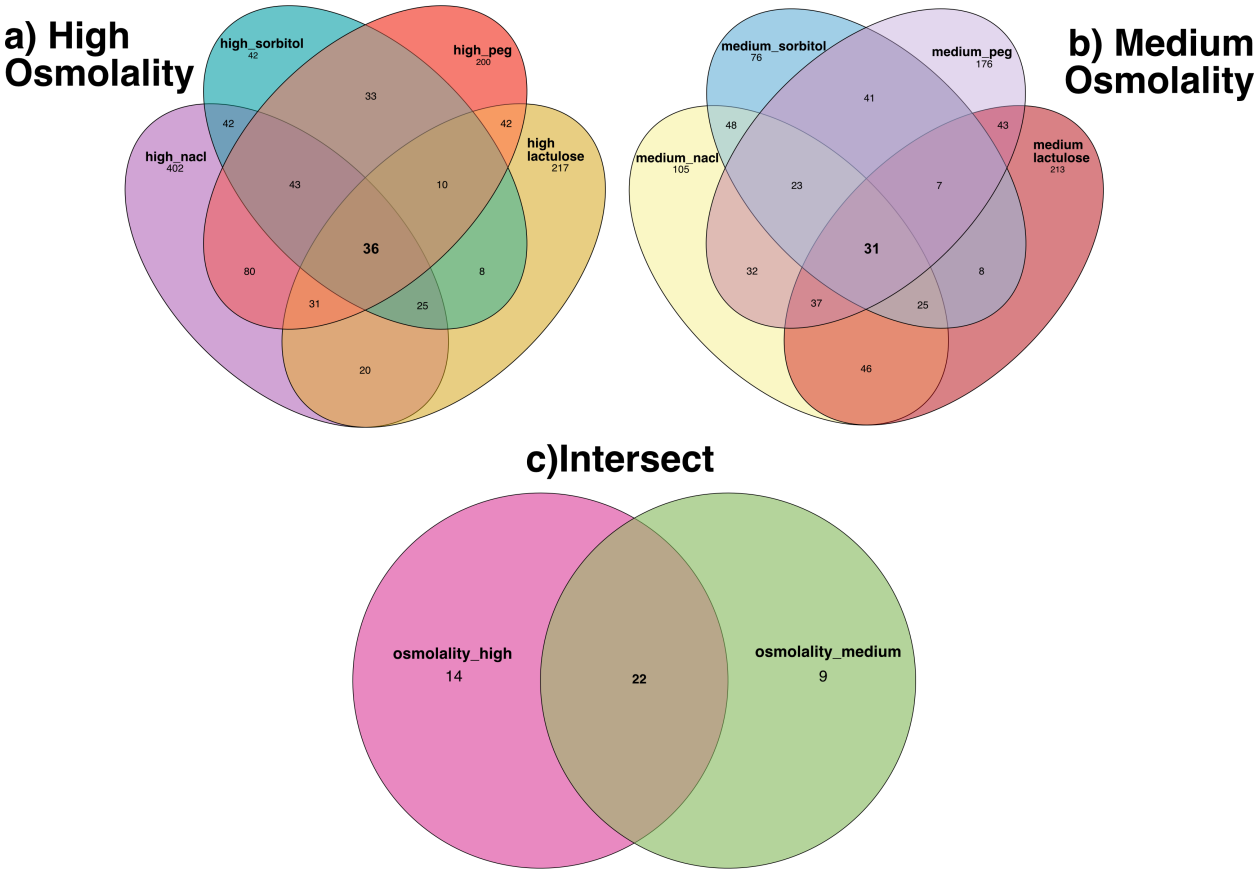

Figure 6. Relationship between over expressed genes in all the osmolality conditions. Venn's diagrams were used to illustrate these relationships. Above, 4-way Venn diagrams of all the **a)** high and all **b)** medium osmolality conditions are shown separately. In bold, the number of genes in the intersection between these conditions is shown. **c)** The intersection of high and medium osmolality conditions via a 2-way Venn diagram, the number of genes in common are displayed in bold.

As said before, an important quality of biosensors is specific response to the input of interest. For this reason, it is important to find genes that respond to osmolality and not other sources of stress. To do this, the differential gene expression of EcN in general stress conditions was also analyzed. The relationship between the high osmolality, medium osmolality (**Figure 6**), high temperature stress, acidic pH stress, and oxidative stress genes was explored. A 5-way Venn diagram shows that 6 genes were being exclusively expressed due to osmolality shifts: 4 genes for high osmolality and 2 genes for medium osmolality (shown in bold) (**Figure 7**). On the other hand, it was found that all the 22 genes over expressed in both high and medium osmolalities are also over expressed in at least one of the general stress conditions (**Figure 7**), posing an obstacle for specific sensing in the complex environment of the gut. The level of expression of these genes throughout the conditions assayed is shown in **Figure 9**.

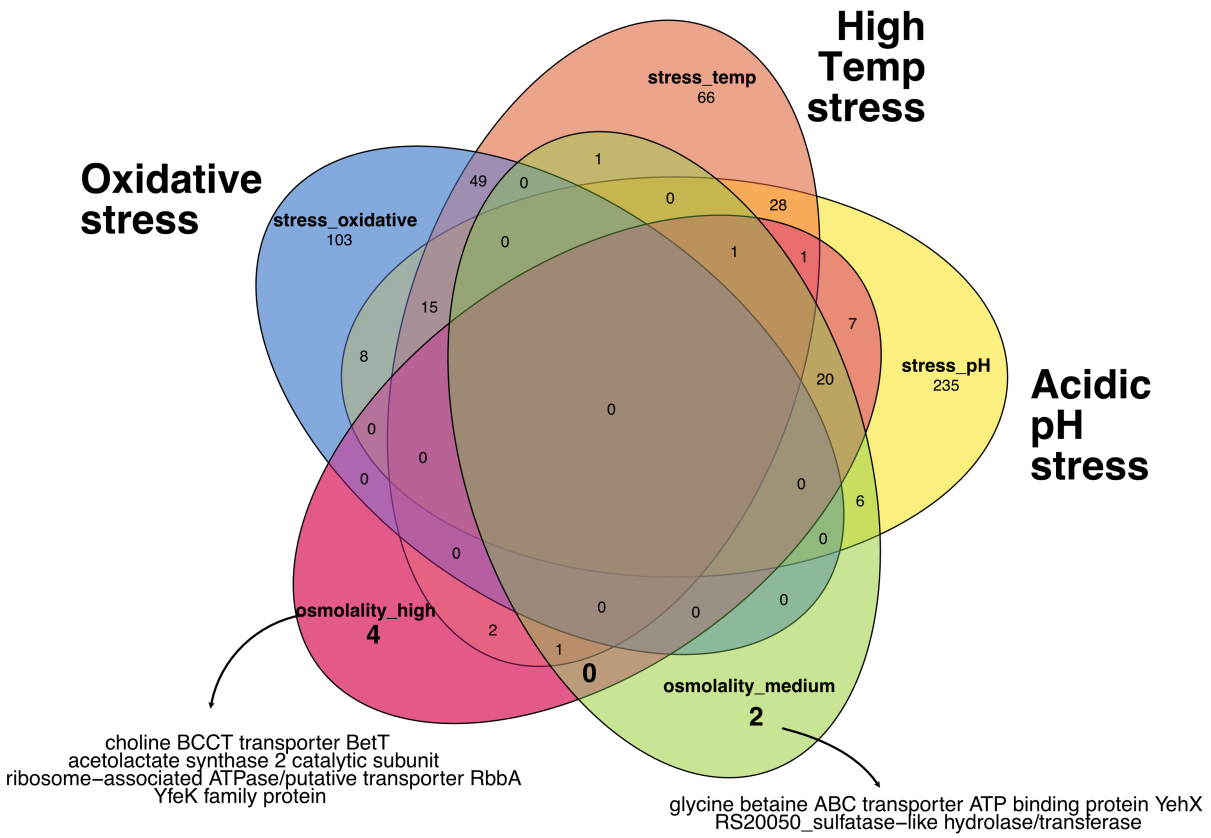

Figure 7. Relationship between over expressed genes in high osmolality, medium osmolality conditions, and general stress conditions (high temperature (42°C), acidic pH (5.8) and oxidative stress (100mM hydrogen peroxide)). A 5-way Venn diagram shows these interactions. In bold, the number of genes being exclusively expressed by osmolality. The names of the genes being exclusively over expressed in high and medium osmolalities are shown.

As previously shown, EcN adapts to environmental stress by expressing different genes and pathways. Although interesting, all these measurements were done in the exponential growth phase. Given that bacteria adjust their gene expression to cope with the shift to stationary phase[103], osmolality response during this phase was also explored (**Chapter 2, section 2.3, Materials and methods**). Interestingly, from the 6 genes that are over expressed only in medium or high osmolality (**Figure 7**), 3 are also over expressed in stationary phase without stress (**Figure 2.6**). This result shows that these genes are activated by both osmolality and stationary phase, posing a problem for specific sensing in the gut environment. On the other hand, 2 of the remaining genes were over expressed in stationary phase with high osmolality stress, showing that these genes respond to osmolality shifts in both growth phases (**Figure 8**, in bold). There was one gene that was only expressed in medium osmolality conditions during exponential phase, and it showed no activity in the stationary phase conditions assayed (**Figure 8**). On the other hand, of the 22 genes over expressed in both high and medium osmolality, 17 are highly expressed in stationary phase

without stress (**Figure 8**). The remaining 5 genes respond to high and medium osmolalities during exponential and stationary phases (**Figure 8**).

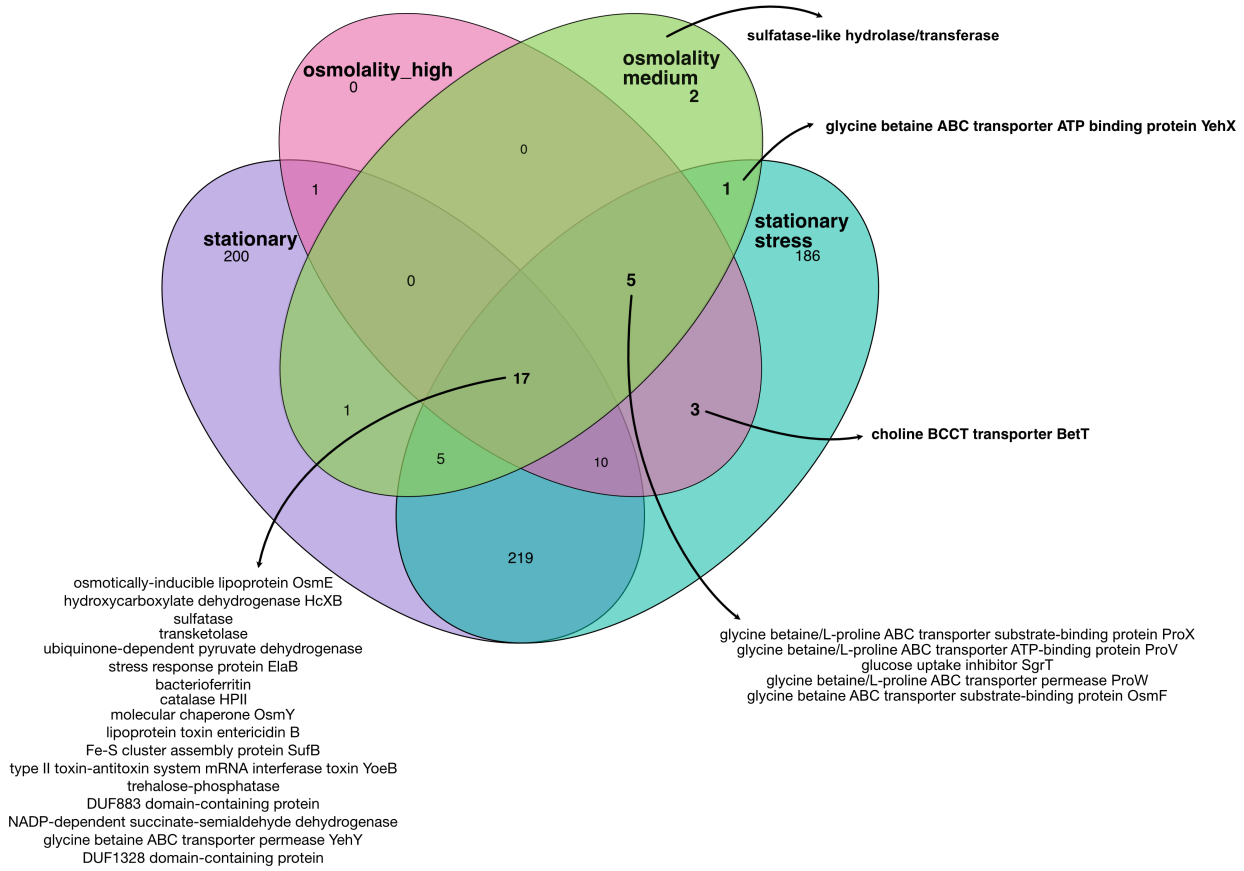

Figure 8. Relationship between over expressed genes in high osmolality, medium osmolality conditions, and stationary phase conditions. A 4-way Venn diagram illustrates these interactions. The names of the genes being over expressed in the stationary phase conditions, high and medium osmolalities are shown. The genes in bold correspond to the selected genes in **Figure 7**.

A strong response to osmolality in both growth phases is a desirable quality for biosensor development because *in vivo* measurements require the bacteria to navigate the complex environment of the gut. Here, the cells will be exposed to a variety of environmental conditions for a prolonged amount of time[4,104], which makes specific sensing a key element. Because of this, this study selected only genes that are not active during stationary phase without stress but respond to osmolality in exponential and stationary phase.

3.4.3 Levels of expression for EcN's osmolality genes and selection of promoters for biosensor development

Although the independent filtering and comparison between conditions resulted in a group of possible genes to use for the biosensor (**Figure 6, 7** and **8**), it is important to explore the level of

expression of these genes across all of the conditions. To do this, a heatmap showing gene expression was used (**Figure 9**). While expression varies in each individual condition (*e.g.* high lactulose, medium NaCl), it is observable that expression trends are maintained within treatments with certain exceptions. For instance, high expression was observed across all of the high osmolality and/or medium osmolality treatments. Likewise, low expression trends are observed in both high temperature stress and oxidative stress treatments. Interestingly, the acidic pH stress treatment showed similar expression patterns as the osmolality treatments; 21 out of the 22 genes over expressed in high and medium osmolality were also over expressed in the acidic pH condition, but not in the other two general stresses assayed (**Figure 7** and **9**). It has been observed that acid tolerance and osmotic pressure regulation share certain mechanisms, and thus gene expression patterns, to combat these stresses[99,105].

As mentioned before, only 2 genes were not expressed in the general stress conditions nor stationary phase without stress, but were expressed in stationary phase with stress (**Figures 7 and 8**) and, either high (shown *** and bold in **Figure 9)** or medium osmolality conditions (shown ** and bold in **Figure 9**). Also, there were 5 genes over expressed in high and medium osmolality conditions during exponential and stationary phase (**Figure 8 and 9**) that were not over expressed in stationary phase without stress. Based on these criteria, these 7 genes (**Figure 9** in bold) were analyzed as candidates for biosensor development.

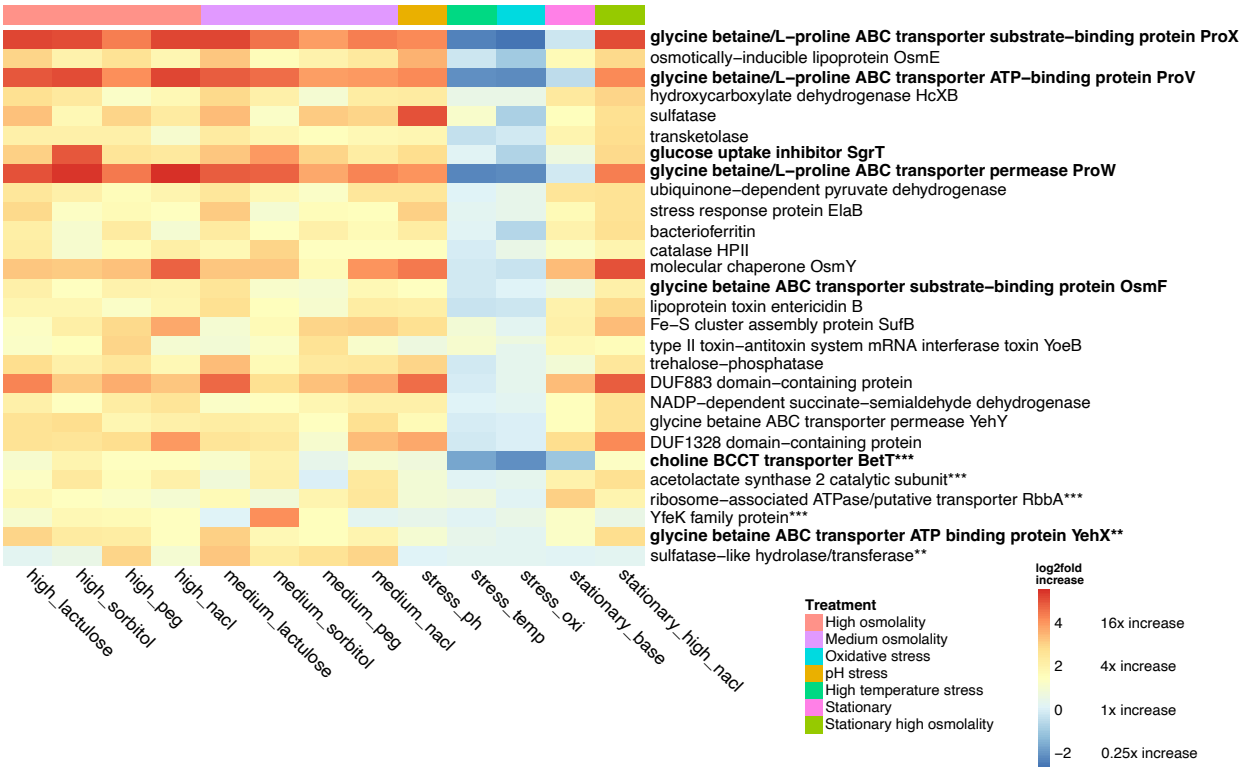

Figure 9. Heatmap illustrating RNA-seq differential expression data of genes overexpressed at high and/or medium osmolality across all the conditions assayed. The information is labeled according to the legends to the right. Red to yellow colors indicate values greater than 0. White to blue colors indicate values around or below 0. Genes exclusively over expressed at high osmolality are labeled with ***. Genes exclusively over expressed at medium osmolality are labeled with **. The rest of the genes are overexpressed at high and medium osmolalities, with over expression in at least one of the general stress conditions assayed. Shown in bold are the genes that did not show over expression during stationary phase, without stress.

Looking at the heatmap, it is clear that some genes respond more strongly than others to the conditions assayed. Of the 7 genes selected, the highest fold increase (greater than 4 log2 increase in some cases, **Table 5**) in high and medium osmolalities, was observed for *proX*, *proV*, *proW* (**Figure 9**). These genes encode the glycine betaine/L-proline ABC transporter and are expressed as a transcriptional unit called *proU* operon[106], explaining the similarity in their expression patterns. This operon is a key part of *E. coli and* other enterobacteria osmoregulation mechanisms, where cells respond to osmotic pressure by intracellular accumulation of solutes[107]. Furthermore, it was identified that the *proU* operon has two upstream regulatory elements or promoters: P1 and P2[108]. It is important to note that gene expression was similar in the two levels of osmolality assayed (**Table 5**), making it difficult to use these promoters to specifically sense high or medium levels of osmolality in the gut.

Another interesting gene to look at is *sgrT*, which encodes the glucose uptake transporter inhibitor SgrT and a small-RNA (sRNA) SgrS. In this study, the heatmap shows that across the osmolality conditions, this gene has an over expression between 2 and 4 log2 fold increase from the base

condition (**Figure 9**). In the literature, it's reported that SgrT and SgrS act separately in the glucose-phosphate stress response.[109] To date, this is the first time this gene is identified in the osmotic stress response of *E. coli*, hinting at the differences between EcN and other *E. coli* strains. Since the complex environment of the gut could activate different stress response circuits in bacteria, including glucose-phosphate stress, using this gene for biosensor development could lead to unspecific sensing. Due to this, this gene was excluded from further development as an osmolality biosensor.

A different gene over expressed in both osmolality conditions is *osmF*, which encodes the glycine betaine ABC transporter substrate binding protein. As seen in the heatmap, the expression levels of this gene across the osmolality samples are around ~2 log2 fold increase from the base condition (**Figure 9, Table 5**). It is reported that this protein binds glycine betaine to the transporter at low affinities at physiological conditions and stationary phase[110,111]. This gene is co-expressed with the *yehZYXW* operon, which is responsible for encoding the ABC transporter mentioned above. Interestingly, the gene *yehX* (encoding for glycine betaine ABC transporter ATP binding subunit YehX) is part of this operon[111], and was found to be over expressed in all the medium osmolality conditions, some high osmolality conditions and stationary phase with high osmolality (**Figure 9**). There are two identified promoters for this transcriptional unit, *osmFp1* and *osmFp2*[110]. This is the first study where these genes are identified in the osmotic response of *E.coli*, contradicting previous findings[110]. This result could hint at a difference between EcN and other *E. coli* strain's response to osmolality. It is important to highlight that gene expression is similar in both osmolality levels assayed (**Table 5**), which could interfere with specific sensing of different osmolality levels.

Lastly, there is *betT*, which encodes for a choline BCCT transporter, and is over expressed in all of the high osmolality conditions including stationary phase, but not in the stationary phase condition, general stress or some medium osmolality conditions (**Figure 9**). This gene is part of the Betaine Carnitine Choline Transport (BCCT) family of proteins and plays a central role in *E. coli*'s osmoadaptation strategy. Similar to other genes in this study, expression levels in both of the osmolality conditions are close together (**Table 5**).

Gene(s)	Promoter	Log2 fold increase high osmolality	Log2 fold increase medium osmolality
proU operon: *proX, proV, proW*	*proVp1, proVp2*	5.026 ± 0.437	4.463 ± 0.483
osmF-yehYXW operon: osmF, yehX	*osmFp1, osmFp2*	1.904 ± 0.301	1.672 ± 0.731
betT	*betTp*	1.521 ± 0.344	1.207 ± 0.657

Table 5. List of selected genes and respective promoters for osmolality biosensor development. Log2 fold increase average of high and medium osmolalities is shown for each with standard deviation.

In summary, the discussed genes, except for *sgrT*, were selected based on their gene expression profiles and fuction reported in the literature. All of the selected genes showed reactivity in more than one condition, that being high or medium osmolality, and acidic pH stress.

3.5. Discussion

This work focused on finding genes and their respective promoters that were responding to osmolality perturbations caused by a variety of osmolytes (lactulose, PEG, sorbitol, NaCl). First, it was shown that EcN has different growth patterns in the different osmolytes and osmolalities tested (**Figure 3**), therefore presumed that EcN is expressing different genes at different levels in order to survive. Following the logic of the osmolality conditions above, EcN is presumably expressing different genes in order to survive the general stress (acidic pH, high temperature and oxidative stress) according to the different response in rich media and rich media with general stress (**Figure 4**).

These observations were later corroborated by the transcriptomics analysis, which evaluated the gene expression of EcN to the above-mentioned conditions (Figure 5). Through filtering, comparison, and contrast of over expression patterns in medium and high osmolality conditions, it was revealed that 22 genes are responding to all osmolality perturbations, while 9 respond to the medium osmolality conditions and 14 to high osmolality conditions (Figure 6). Moreover, comparing these groups to the transcriptional response of three general stress conditions (acidic pH, high temperature and oxidative stress) revealed that none of the 22 genes are specifically responding to osmolality, as they all respond to at least one of the general stress conditions (21 respond to the acidic pH and 1 responds to high temperature) (Figure 7). On the contrary, of the 9 and 14 other genes, 6 were not reactive in the general stress conditions; 4 genes were exclusively expressed in all high osmolality conditions, while 2 in all the medium osmolality conditions assayed (Figure 7).

A strong response to osmolality in both exponential and stationary phase is a desirable quality for biosensor development because in vivo measurements require the bacteria to navigate the complex environment of the gut. In the context of a gut biosensor, cells will be exposed to a variety of environmental conditions for a prolonged amount of time[4,104], which makes specific sensing a key element. Therefore, an analysis of the osmolality response in stationary phase was made. Here, it was elucidated that out of the 22 genes mentioned above, only 5 were specifically responding to osmolality perturbations instead of responding to general stress caused by the transition from exponential to stationary growth phase (Figure 8). Three of these genes were expressed as a transcriptional unit called the proU operon, one is called sgrT and the last one is osmF. Similarly, only 1 out of 4 genes responding to high osmolality (betT), and 1 out of 2 in medium osmolality (yehX), showed a response to osmolality in stationary phase (**Figure 8 and 9**). Taken together, there were 7 potential genes considered for biosensor development, their level of expression (**Figure 9**) and reported function in the literature will determine whether they are suitable for gut osmolality biosensors.

The proU operon, encoding the glycine betaine/L-proline ABC transporter, is a well-known system in the osmoregulatory response of enterobacteria[106]. In *E. coli*, it is reported that this operon is induced by 20-70 and 400-fold at high osmolarities (osmolality increases as osmolarity increases) using *lacZ* fusions and β-galactosidase activity[112–114]. Also, gene expression tools like DNA microarrays and Northern Blots reveal over-expression of this operon in elevated osmolarities[97,98]. According to this, it is logical that these genes have high expression in the conditions assayed in this study, confirming EcN is directly responding to changes in osmolality. Extensive research shows that the activation of these genes is governed by two promoters; P1 is regulated at the transcriptional level by σ^s (*rpoS*), while P2 is regulated by σ^{70} (*rpoD*)[108,115,116]. It is known that in *E. coli*, RpoD is the principal sigma factor that aids in the initiation of transcription under physiological conditions[117], while RpoS is an alternative sigma factor present in suboptimal conditions like environmental stress and during stationary phase[118]. This data explains why the *proU* operon responded to osmolality shifts in different growth phases (**Figure 8** and **9**). It was observed that gene expression was similar in the two levels of osmolality assayed (**Table 5**), making it difficult to use these promoters to specifically sense high or medium levels of osmolality in the gut. Nonetheless, the promoters of the *proU* operon (*proVp1* and *proVp2*) were selected as candidates for gut osmolality biosensor development (**Table 5**). Further, *in vivo* testing of these promoters will give more insight into the differences of gene expression patterns between high and medium osmolality levels.

This study also confirmed the activity of betT, which encodes for a choline BCCT transporter. BetT is a membrane bound transporter of choline, a precursor of the osmoprotectant glycine-betaine[119]. As explained before, E. coli accumulates this compound in response to osmolality shifts in the environment[98]. This gene is regulated by the promoter, betTp whose expression is reported to be tightly linked with increasing osmolality conditions[119]. Based on this, this promoter was

selected for further biosensor development (Table 5). Like proU, expression levels in both of the osmolality conditions are close together (Table 5). Thus, other analyses will be needed to understand differences in gene expression and determine if this promoter is appropriate for specific biosensing in the gut, nevertheless, this gene, and its promoter were selected for biosensor development.

Contrary to these findings, three genes have not been observed to act in the osmoadaptative response of E. coli, hinting at possible differences in the osmoadaptative response between EcN and other E. coli strains. The first gene, sgrT, has a central role in the glucose-phosphate stress response. Here cells reduce sugar uptake to combat the accumulation of phosphorylated glucose analogs that cannot be metabolized[109]. Both of it's products, SgrT and SgrS, inhibit the major glucose transporter (PtsG) and mannose transporter (MnnXYZ); SgsS does it in a transcriptional level by base-pairing to the mRNAs of the transporters, while SgrT binds directly to the PtsG transporter in the membrane[109,120,121]. As previously mentioned, during osmotic stress, the cell accumulates solutes intracellularly to combat the osmotic pressure[122]. It is not clear why this gene was over expressed in all of the osmolality conditions assayed and not the two general stress conditions, but it was not considered for further biosensor development because it could lead to unspecific response to other types of stress, especially in a complex environment like the gut.

In contrast, the second and third genes, osmF and yehX, are co-expressed in the yehZYXW operon and encode a glycine betaine ABC transporter and a binding protein. This transcriptional unit has 2 promoters (osmFp1 and osmFp2) regulated by different transcriptional regulators. The first promoter is regulated by σS (rpoS), an important regulator for stress response and stationary phase in E.coli[118]. The second promoter is regulated by σ32 (rpoH), known as the key regulator of E.coli's heat shock response[123]. A study on the functionality of this operon reveals that contrary to other transporter systems, it does not directly act in the osmotic stress response, thus, it is not over expressed in high osmolality conditions[111]. Authors attribute osmotic induction of this operon to cross reactivity due to stress cross-resistance, something explained by the regulatory elements that govern its expression. It's unknown whether this operon plays a real role in EcN's osmolality response, but given their strong response in both of the osmolality conditions (Table 5), these genes and their promoters were selected as candidates for osmolality biosensor development (Table 5). Further experimentation in vitro and in vivo is required to determine differences of gene expression between high/medium osmolality and whether the activation of this operon is an osmolality-specific response.

This work also showed that some of these promoters present cross reactivity to acidic pH conditions. Since bacterial response to stress is a complex and broad process, this result was expected, nevertheless it will be a constraint for biosensor development. A possible way to control for cross reactivity is engineering logic gates into the genetic circuit, a strategy previously used for gut biosensor development. For instance, promoter 1 responds to osmolality and stress "A", while

promoter 2 responds to stress "A" but not osmolality. This way, the circuit will be activated only when osmolality shifts are encountered. Taking the results of this study, the over expressed genes in the three general stress conditions assayed could be used as a control for nonspecific sensing (**Figure S5**). Another constraint of using these genes will be their similar response to high and medium osmolality levels, making it difficult to separately report for each of these conditions. Further gene expression studies (*e.g. in vivo* transcriptomics, qPCR, high throughput testing of fluorescence driven libraries, among others) will be needed to precisely determine if there are significant differences in the levels of expression between medium and high osmolality. An alternative could be to consider repressed genes as well, given that repression is also an option to report on microbial activity.

Taken together, the selection of these five genes provides a starting point for gut osmolality biosensors using the probiotic strain EcN. Finally, this thesis showed that characterizing the transcriptional response of this bacterium elucidated gene expression patterns that had not been reported in other strains of *E.coli*, providing more options for building biosensors of gut biomarkers.

Chapter 4: Measuring prion propagation in single bacteria elucidates mechanism of loss

4.1. Chapter Introduction

It has been observed that single cells have different behaviors in clonal populations[124]. This phenomenon is known as cellular heterogeneity, and it allows organisms to respond to a variety of environmental cues, improving their survival and functionality[125]. An example of this is prions, commonly known as self-propagating protein aggregates made up by proteins that are able to adopt a different configuration[126]. Recognized as protein-based elements of inheritance, prions can generate the existence of different phenotypes in a clonal cell population[127]. Recently, the existence of bacterial prions was elucidated with the *Clostridium botulinum* Rho transcriptional terminator and the *Campylobacter hominis* SSB protein[128,129]. In these studies, *E. coli* was used as a model organism, where a new genetic assay determined that prion propagation occurs for over a hundred generations. Interestingly, it was observed that a fraction of the cells lost the prion by an unknown mechanism. Since propagation studies are done at a population level, it is challenging to determine the loss mechanism from cell to cell. Here, we used the mother machine microfluidic device to study prion loss in single bacteria. In this manuscript, a mechanism of prion propagation and loss was uncovered in bacteria. With this data, a stochastic model was developed, explaining the dynamics of this process.

4.2. Introduction

Prion-forming proteins (hereafter prion proteins) are proteins that can adopt multiple conformations, of which at least one is self-propagating. Prions were originally discovered as the cause of devastating neurodegenerative diseases, such as Creutzfeldt-Jakob's disease (CJD), in mammals[126]. Subsequently, non-pathogenic prions were found across diverse species – such as budding yeast[130–134], Drosophila[135], Arabidopsis[136], and mammals[137–139] – where they are thought to function as protein-based carriers of epigenetic information. In many cases, the prion capability is conferred on the protein by a modular prion domain (PrD), necessary and sufficient for formation of the prion. Conversion from the soluble form to the prion form (a highly structured aggregated form in many well-studied cases) bestows a loss-of-function[140] or gain-of-function[138,141,142] to the attached protein, which can result in a fitness advantage under certain environmental conditions[132–134,143,144]. A particular property of prions is that they can sometimes form multiple structures, called strains, each of which propagates itself with different properties. In mammals, different strains of the prion protein (PrP) are the cause of different diseases[145,146], while in yeast different strains of the intensively studied prion [*PSI*$^{+}$] (formed by the essential translation release factor Sup35) differ in their stabilities and aggregate size distributions[147–149].

While the detailed molecular mechanisms of prion propagation are under investigation[150,151], studies in yeast and mammals appear to be consistent with the nucleated polymerization model[152–154]. In this model, proteins are converted from the soluble form to the prion form by elongation of existing oligomeric prion aggregates, while aggregates can be fragmented into smaller oligomers (presumably by chaperones like Hsp104, an ATP-dependent disaggregase that is required for prion propagation in yeast[155]). Initial conversion to the prion form is suggested to happen by the rare spontaneous oligomerization to a critical size *n*, below which oligomers would revert to the soluble form.

Recently, thousands of candidate prion domains (cPrDs) have been identified in bacteria using bioinformatic analyses[129]. So far, two of these domains were found to form self-propagating prion aggregates in *Escherichia coli*: the PrDs from the Rho termination factor of *Clostridium botulinum* (*Cb* Rho,[129]) and from the single-stranded DNA binding protein of *Campylobacter hominis* (*Ch* SSB,[128]). Of note, many orthologs of these proteins also have predicted cPrDs[129]. Although individual lineages could propagate the prions for more than a hundred generations, a fraction of the cells in each lineage was seen to lose have lost the prion at each replating round[128,129]. The mechanisms by which the prion is lost, and how long individual cells propagate the prion, are unknown. In the previous study of the *Ch* SSB PrD, two types of lineages were observed, one exhibiting a high-stability phenotype and one exhibiting a lower-stability phenotype, suggesting that prion strains could also exist in bacteria[128]. In addition, although the molecular mechanisms of prion propagation appear conserved across mammals and yeast, it is unknown if this apparent conservation of mechanism also extends to bacteria.

In this study, we sought to address these questions by measuring prion propagation in single bacteria. Using microfluidics, single-cell time-lapse microscopy, and mathematical modeling, we uncover how the *Ch* SSB PrD prion (hereafter the *Ch* SSB prion) is propagated and lost. We find that the prion is propagated in two distinct modes with aggregates of different size and stability. We discover that the loss of the prion was caused mainly by stochastic inheritance of the aggregates to only one of the two daughter cells at division (i.e. “partitioning errors”). We show that two orthologous SSB cPrDs also form self-propagating prion aggregates, and that the modes of propagation and loss are conserved in these domains. In addition, we describe lineage-specific differences in the stabilities of prion propagation, thus providing additional support for the previous suggestion that bacterial prions, like yeast prions, can exist as phenotypically distinct strains. We also describe a *Ch* SSB PrD mutant that undergoes conversion to the prion form more readily than the wild-type domain. We implement a stochastic version of the nucleated polymerization model, which strikingly recapitulates all the observed single-cell properties. We use this model to further corroborate our finding that prion loss is caused by partitioning errors by making a prediction, which we then validate experimentally. The model also allows us to estimate the prion replication rate, which is found to be similar to that of mammalian prions. This work provides a new assay for studying prion propagation in individual cells, provides insights on prion

propagation and loss, and further establishes the conservation of prion propagation mechanisms across domains of life.

4.3. Results

Experimental system to track prion propagation and loss in single cells

To investigate how long individual cells propagate a prion and the mechanisms of prion loss, we developed an experimental system that enables us to track prion propagation in thousands of individual cells for many cell divisions (**Fig. 10a-d**). For this, we used the previously constructed His6-mEYFP-Ch SSB-PrD (hereafter Ch SSB PrD) fusion protein [128] to visualize prion propagation using fluorescence microscopy. Like the Sup35 prion protein in yeast[156–158], Ch SSB PrD requires the presence of a pre-existing prion known as [PIN+] (for [PSI+] inducibility) to access the prion conformation, but not for its maintenance (i.e. the propagation phase)[159]. Several prion proteins can serve as [PIN+], including the *Saccharomyces cerevisiae* New1 protein[156,159–162]. Therefore, to study prion propagation, we transiently expressed a New1-mScarlet-I fusion on a temperature-sensitive plasmid. After inducing synthesis of the New1 fusion protein and subsequently curing the cells of the New1-encoding plasmid (verified by antibiotic sensitivity and absence of mScarlet-I signal, **Fig. S6a-c**), colonies containing prion-propagating cells were identified using a previously developed reporter system[159]. Specifically, cells containing prion aggregates were previously shown to have elevated levels of the chaperone ClpB, such that colonies containing such cells can be distinguished on X-gal-containing plates using a PclpB-lacZ reporter[159]. As expected, dark blue colonies displayed visible protein aggregation of the Ch SSB PrD (as observed by fluorescence microscopy) in a fraction of the cells, and cell extracts prepared from blue colony cultures contained characteristic SDS-stable aggregates (as observed by semi-denaturing detergent agarose gel electrophoresis; SDD-AGE) (**Fig. 10b-c**). In contrast, the cells in pale blue colonies showed diffuse fluorescence and contained no SDS-stable protein aggregates (**Fig. 10b-c**). As previously observed[159], replating dark blue colonies gave both dark and pale colonies, while replating pale colonies resulted in only pale colonies. We thus concluded that dark blue colonies contain a mixture of cells with self-propagating prion aggregates displaying aggregated fluorescence and cells with the protein in the soluble form exhibiting diffuse fluorescence.

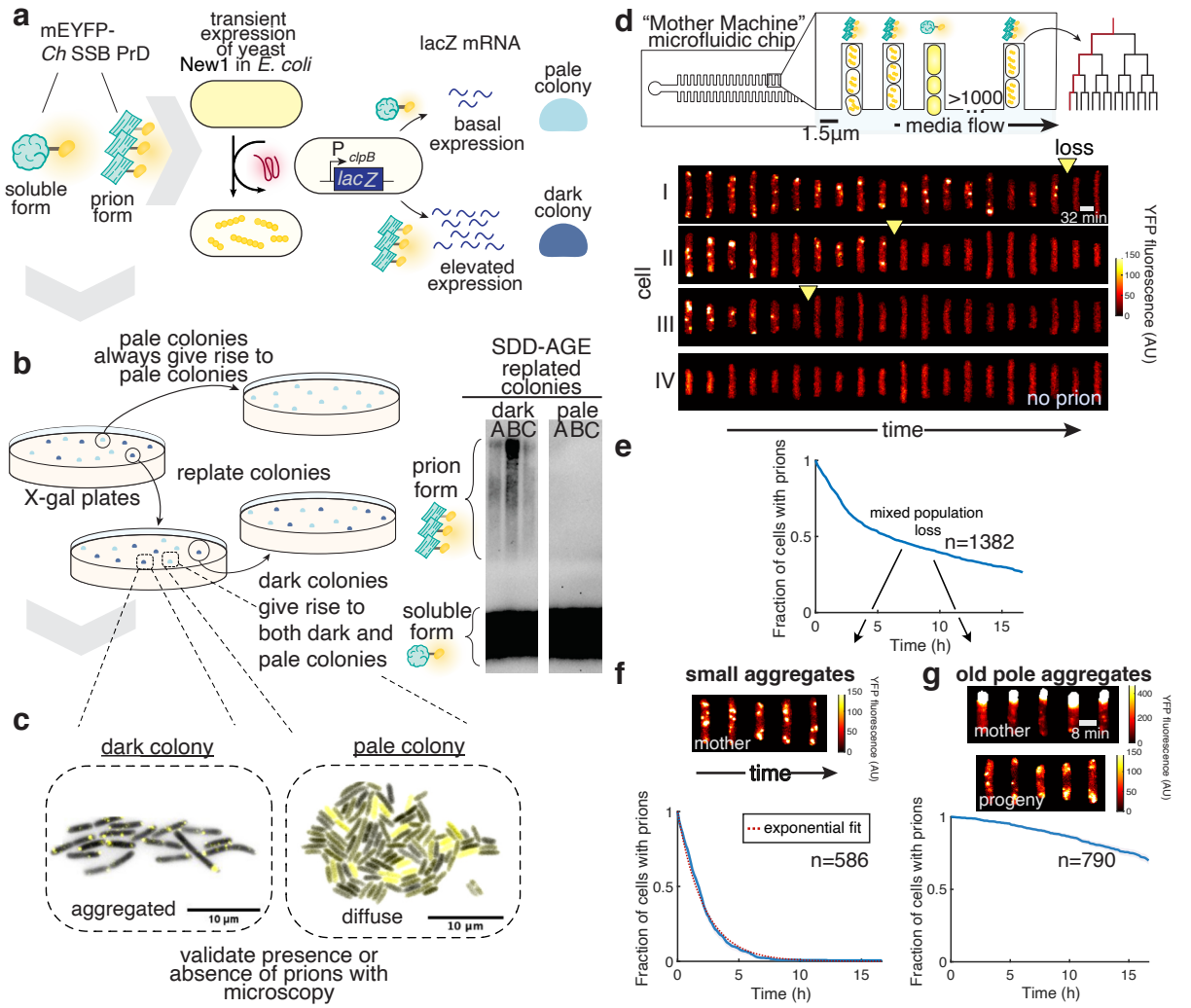

Fig. 10. **Experimental setup enables quantification of prion dynamics in single cells**. **a)** Transient expression of the *S. cerevisiae* New1 protein induces conversion of His6-mEYFP-Ch SSB PrD from its soluble form into the prion form in *E. coli*. Bacteria with prions have elevated levels of ClpB, such that bacterial colonies with prion-containing cells can be distinguished from colonies with cells containing the protein in the soluble form using a PclpB-lacZ transcriptional reporter (dark blue vs pale colonies, respectively). **b)** Dark blue colonies contain self-propagating aggregates. (Left) Replating dark blue colonies results in a mix of dark and pale colonies, while replating pale colonies results in only pale colonies. (Right) SDD-AGE shows that different dark blue colonies (A, B and C) contain SDS-stable aggregates, whereas pale colonies contain only soluble Ch SSB PrD (prion formation was induced with New1-CFP; a gel where induction was done with New1-mScarlet-I can be found in Fig. S1d). **c)** Fluorescence microscopy images of *E. coli* expressing His6-mEYFP-Ch SSB PrD shows that cells from dark colonies display visible fluorescence aggregation, whereas cells from pale colonies display diffuse YFP fluorescence. **d)** After prion conversion, cells from a dark blue colony are loaded in a microfluidic device where cells are trapped in dead-end trenches and newborn cells are washed away by the flow of growth medium. Fluorescence time-lapse microscopy montage (kymographs) of individual lineages shows that cells propagate the aggregates for heterogeneous duration (I-III) before irreversibly reverting to diffuse fluorescence. YFP fluorescence is shown false-colored according to the colormap indicated on the graph. The prion loss called by our spot-finding algorithm is indicated by a yellow triangle. Cells that have diffuse fluorescence at the beginning of the experiments maintain it (IV). **e)** The fraction of cells with prions over time (prion loss curve) for all aggregate phenotypes shows a biphasic decay, suggesting the presence of two distinct subpopulations. **f)** The prion loss curve for cells with small aggregates fits well to an exponential distribution (red line, R = 0.92). Representative kymograph of cells with small aggregates (top) **g)** Loss curve for cells

with old-pole aggregates. Kymographs for the tracked cell (mother) and its progeny (top). The old-pole aggregate is mostly immobile, and the progeny contain small aggregates. The colormap for the old-pole aggregate is different as these aggregates are brighter. The standard error on the mean (SEM) in **e-g** was estimated by bootstrapping, and an envelope is shown as 2xSEM.

For time-lapse microscopy, cells from a single colony containing prion-propagating cells were loaded into a microfluidic device[163] where cells are trapped in short trenches and the newborn cells are washed away by the constant flow of growth media (**Fig. 10d**). Automated time-lapse microscopy and analysis enables us to track individual lineages for more than two dozen cell divisions while precisely measuring cell fluorescence, growth rate, size, and other characteristics. Using this approach, we observed that cells propagated the prion (aggregated fluorescence, **Fig. 10d**) over multiple cell divisions before irreversibly losing the prion (diffuse fluorescence, **Fig. 10d**). Even though the protein concentration was constant throughout the experiment (after reaching equilibrium of growth conditions, **Chapter 2, Materials and Methods 2.9, Fig. S7a-c**), individual lineages displayed remarkable variation in the duration of prion propagation; some cells lost the prion after a few divisions while others kept it for the whole duration of the experiment (~30 divisions).

Prion propagation occurs through two distinct modes

We next sought to quantify how long individual cells could maintain the prion. For the analyses, we define the time of prion loss as the last time aggregates were detected using a spot-finding algorithm (**Chapter 2, Materials and Methods 2.9, Fig. S8a-c**). Counting the detectable aggregates showed that aggregates were both lost and generated until the irreversible loss event, supporting the idea that the prion is propagated during the experiment rather than being simply diluted (**Fig. S8d**). To measure the distribution of propagation duration, we calculated the fraction of tracked cells containing prion aggregates as a function of time (**Chapter 2, Materials and Methods 2.9**). We observed a loss curve with two phases: an initial phase of rapid loss followed by a phase with a slower rate of loss (**Fig. 10e**). This result suggested that there could be two sub-populations of cells with distinct loss kinetics. Indeed, upon visual inspection of the cells, we noticed that a fraction of the cells contained a large aggregate localized to the old pole (i.e. the pole not renewed after cell division), while the rest contained many small and dynamic aggregates (**Fig. 10f-g**). This old-pole aggregate was mostly immobile, presumably because its size sterically prevents diffusion through the nucleoid (**Fig. 10g**). These cells contained bona fide prion aggregates as their progeny contained small aggregates similar to the small and dynamic aggregates that we observed for the other cells in the device (**Fig. 10g**). We thus re-analyzed the loss kinetics, but this time separately for the small and old-pole aggregate types. We used two different methods for classifying old-pole aggregates, based on the mobility of the aggregates or the fluorescence intensity, which gave similar results (**Chapter 2, Materials and Methods 2.9, Fig. S9a-b**). We found that the small aggregates were lost relatively quickly, while the old-pole aggregates were generally much more stable (**Fig. 10f-g**). The loss curve for the small aggregates fitted well with an exponential decay with a half-life of ~1.5h (**Fig. 10f**), representing a process

with a constant probability of losing the prion state over time (i.e. a memoryless process). This memoryless process is consistent with previous replating experiments, where a similar fraction of prion-positive colonies is found upon successive replating[129,159,160]. In contrast, few cells with the old-pole aggregates lost the prion over the course of the experiment (93 out of 790 cells), which precluded us from analyzing the loss dynamics of the old-pole aggregates.

These data suggest two modes of prion propagation in *E. coli*: cells containing highly stable old-pole aggregates that give rise to a small aggregate-containing daughter cell at division, and small aggregate-containing cells that lose their prion aggregates with exponential decay. The old-pole aggregate-containing cells would represent a very small fraction of a growing culture (e.g. after 10 divisions, one old-pole cell would become 1 out of 2^{10} = 1,024 cells), but they are enriched in our microfluidic device as we are tracking the cells at the end of dead-end trenches. We thus focused the following analyses on the cells containing small aggregates only.

Prion loss is mainly driven by partitioning errors at cell division

How do cells lose the prion? A previous study in *E. coli* cells producing the yeast Sup35 PrD suggested that loss of the Sup35 prion could occur through fluctuations in the concentration of the prion protein[160]. Based on previous studies in bacteria and yeast[160,164], we hypothesized that the loss could be due to two non-mutually exclusive mechanisms: 1) stochastic variation in the concentration of the prion protein (or other cellular components, such as the disaggregase ClpB, which is required for the propagation of the Ch SSB prion), or 2) mis-partitioning of prion aggregates at cell division (**Fig. 11a**). These hypotheses lead to different predictions about the prion loss dynamics. If prion loss is caused by stochastic fluctuations in either the prion protein or cellular components, prion loss would be uncorrelated with cell division. On the other hand, if prion loss is caused by asymmetric partitioning of aggregates, the loss would be correlated with cell division and would occur in only one of the two daughter cells.

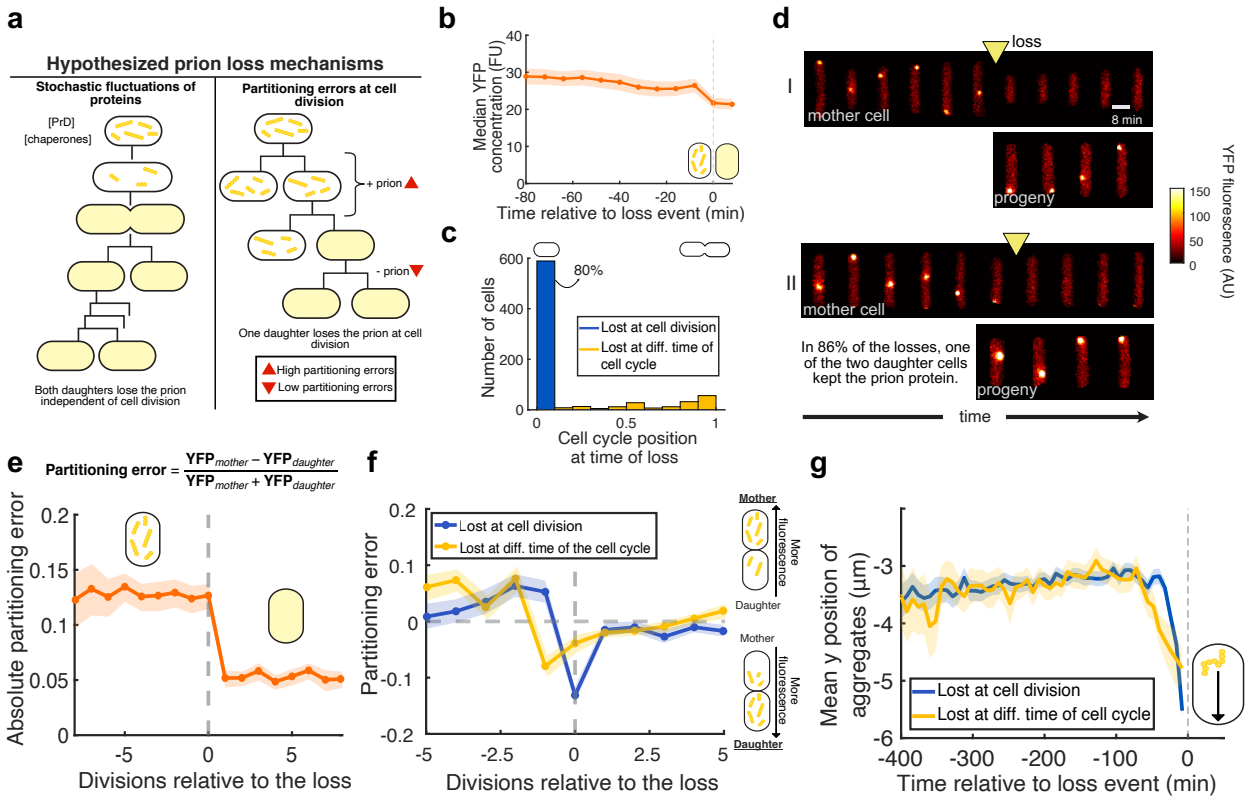

Fig. 11. Prion loss is driven by partitioning errors at cell division. a) Schematic representation of the hypothesized mechanisms for prion loss in bacterial cells. **b)** Median concentration of fluorescence (Ch SSB PrD) relative to the loss of the prion is constant (n = 762 cells). The loss event is indicated with a dotted gray line at time 0. **c)** Histogram of the cell cycle position at the time of loss, where 0 is defined as the moment right after a division and 1 right before. Most cells (~80%) lose the prion immediately after cell division (n = 762 cells). **d)** Kymographs of loss event show that prion loss happens in only one of the two daughter cells (86% of the losses, n = 356 loss events). YFP fluorescence is shown false colored according to the colormap indicated on the graph. **e)** Mean absolute partitioning errors at the cell divisions relative to prion loss (n = 349 cells). The absolute partitioning error is constant prior to the loss, and higher than after the loss. **f)** Mean partitioning errors in the cell divisions relative to the loss show that fluorescence is being transmitted to the daughter at the moment of loss for cells that lost the prion at the moment of cell division (blue lines, n = 349 cells). For the cells that lost the prion at a different moment of the cell cycle, this transfer happens one division prior to the loss (yellow line). For symmetric divisions, the average partitioning error would be ~0, since molecules have an equal chance of being inherited by the mother or daughter cells. **g)** Average longitudinal position (y) of tracked aggregates shows that they move toward the daughter cell prior to the loss (n = 754 cells). The envelopes represent 2xSEM in **b** and **e-g**.

By tracking prion loss in hundreds of cells with fluorescence microscopy, we could test these hypotheses. Aligning the cells at their moment of loss showed that the fluorescence was constant prior to the loss (**Fig. 11b**), suggesting that fluctuations in prion protein levels likely play only a minor role in the overall loss. To investigate the possibility that variation in cellular components plays a role in the loss of the prion, we measured the position in the cell cycle at the moment of loss. We observed that ~ 80% of cells lost the prion at the first time point after cell division (**Fig. 11c**). We also observed that in ~ 86% of losses in the mother (the cell tracked for the duration of the experiment), the prion was maintained in the newly born daughter cell (**Chapter 2, Materials**

and Methods 2.9, Fig. 2d). These observations suggested that prion loss is mainly caused by partitioning errors at cell division rather than fluctuations of cellular components, although they do not exclude the possibility that such fluctuations could contribute[165].

Although *E. coli* divides symmetrically with proteins randomly partitioned in the daughter cells, one cell can end up with more of a particular protein by chance. These "partitioning errors" – defined as the normalized difference in the number of molecules between the daughter cells at division (**Fig. 11e**) – follow a binomial distribution and are generally low because on average they are inversely proportional to the square root of the number of molecules[166,167]. However, cells with the prion have relatively large aggregates, effectively reducing the number of molecules to partition. Partitioning errors at cell division were indeed on average larger and there were more frequent extreme errors (i.e. >30%) before cells lost the prion than after (**Fig. 11e, Fig. S10**). In addition, the partitioning errors were constant prior to the loss (**Fig. 11e**), suggesting that the distribution of aggregate size was constant prior to the loss, and that this loss is a sudden rather than gradual event. This further supports the concept that the prion is being propagated until a stochastic event causes its loss. For the cells that lost the prion at cell division, proteins were found to be asymmetrically separated to the daughter at the moment of loss (**Fig. 11f**). Here, we again define the "mother" cell as the cell tracked for the duration of the experiments, and the "daughter" cells as the progeny that are eventually washed out from the device. For the cells that lost the prion at a different time during the cell cycle, a similar mis-partitioning into the daughter cell was observed one division prior to the loss (**Fig. 11f**), suggesting that partitioning errors also play a role in the loss of the prion in these cells. Corroborating these results, tracking the position of visible aggregates revealed that they moved on average one cell length towards the daughter cell prior to both types of loss (**Fig. 11g**). We thus concluded that, at least in this system, prion loss is mainly caused by stochastic partitioning errors of aggregates at cell division, prior to or at the moment of loss.

Orthologous cPrDs can form prions with similar properties

The two modes of propagation and the molecular events leading to the prion loss could be specific to the studied Ch SSB PrD or a more general property of bacterial prions. To begin to investigate this question, we constructed fluorescent fusions of cPrDs from SSB orthologs. We discovered two orthologous SSB PrDs – from *Lactobacillus heilongjiangensi*s (Lh) and *Moraxella lincolnii* (Ml) – that could form self-propagating aggregates after transient expression of the initiation factor New1, as shown with fluorescence microscopy, SDD-AGE, and replating experiments (**Fig. 12a-c, S11c**). We then evaluated the properties of the aggregates formed by these PrDs in our microfluidic device. Remarkably, we found that their modes of propagation (i.e. small vs old-pole aggregates, **Fig. S11a**), loss kinetics (**Fig. 12a**), fraction of loss at cell division (**Fig. 12d**), and partitioning errors (**Fig. S11b**) were similar to those formed by the Ch SSB PrD (though with some quantitative differences in average loss rates). Therefore, these results support the idea that the

modes of prion propagation and the mechanism of prion loss through mis-partitioning at cell division are not only specific to Ch SSB PrD, but a more general characteristic among SSB PrDs.

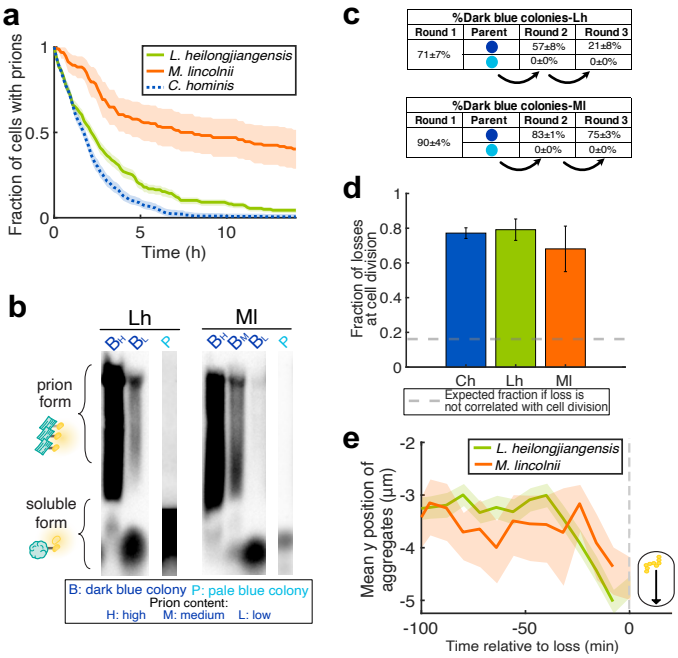

Fig. 12. **Orthologous SSB cPrDs form self-propagating aggregates comparable to Ch SSB. a)** Prion loss curve for small aggregate cells of Lh SSB PrD (n = 228 cells) and Ml SSB PrD (n = 83 cells) compared to Ch SSB PrD from Fig. 1. **b)** SDD-AGE of dark and pale colonies confirms the presence of the aggregated prion form of Lh SSB and Ml SSB in cell extracts derived from dark blue colony cultures. Dark blue colonies with high, medium and low prion content as estimated from fluorescence microscopy images were assayed (Fig. S11d, Chapter 2, Materials and Methods 2.9). Pale colony cultures give rise exclusively to the soluble form. **c)** SSB orthologs form self-propagating aggregates for multiple generations. Replating dark blue colonies gives a mix of dark and pale colonies, while replating pale colonies results in exclusively pale colonies. **d)** Fraction of prion losses at cell division shows that most loss happens at cell division for the different orthologs (n = 754 cells for Ch, 187 cells for Lh, 47 cells for Ml). The error bars represent 2xSEM as estimated by bootstrapping. **e)** Average longitudinal position (y) of tracked aggregates shows that they move toward the daughter cell prior to the loss for the different orthologs (n = 187 cells for Lh, 47 cells for Ml). The envelopes represent 2xSEM in a and **d-e**.

A PrD can be propagated with distinct kinetics in distinct lineages

To investigate whether or not these PrDs could form phenotypically distinguishable prion strains[147–149], we quantified prion stability in cells derived from different dark blue colonies representing different lineages propagating the prion. Our experimental setup provided precise and reproducible measurement of the stability; cells containing the Lh SSB PrD in its prion form (i.e. the Lh SSB prion) and obtained from one colony exhibited similar loss kinetics during four different experiments on four different days (**Fig. 13a**). However, during our quantification of loss kinetics, we discovered one lineage of cells containing the Ch SSB prion that exhibited unusually stable propagation. Quantifying prion stability in cells obtained from this colony in our microfluidic device revealed a loss rate an order of magnitude lower than that of the other lineages (**Fig. 13b**). To test whether this property was self-propagating, we grew the lineage used for the

microfluidic experiments for two additional rounds of about 37 generations each, loading cells from each of the successive rounds of growth into the device (**Fig. 13b**) and also replating them on indicator medium (**Fig. S12a**). Strikingly, the loss kinetics were constant over ~110 generations and nearly all colonies were prion positive after each round of plating. DNA sequencing of the PrD-containing plasmid from cells of this lineage revealed no mutation in the promoter, the PrD, or the plasmid origin of replication (**Fig. S12d**), suggesting that the stability property is inherited through the structure of the aggregates rather than genetically.

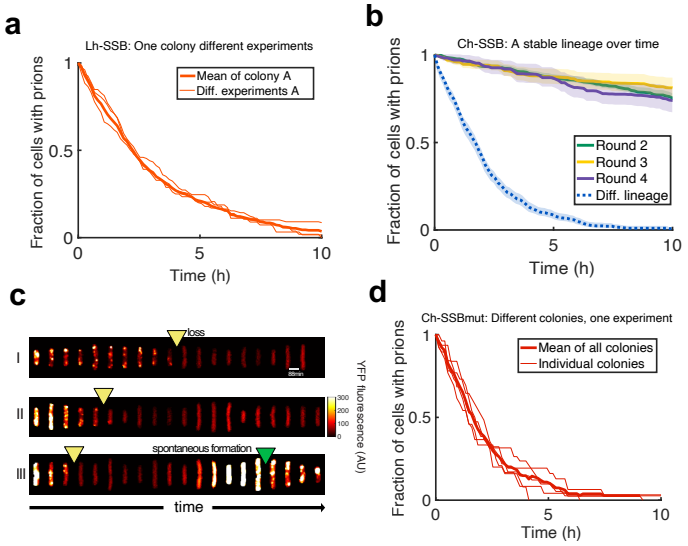

Fig. 13. Distinct bacterial lineages propagating identical prion protein exhibit distinct prion loss kinetics. a) The experimental setup provides precise measurement of the prion loss kinetics. Prion loss curves for one colony of Lh SSB PrD in four different experiments (thin orange lines, average in bold, n = 815 cells total). **b)** The prion loss curve for a stable lineage of Ch SSB PrD remains constant over multiple rounds of growth (~37 generations each, n = 1,018 cells total). Round 1 refers to the first plating of induced cells cured of New1, and each subsequent round includes an overnight growth in liquid culture and plating on indicator medium. Round 2, 3, and 4 cells were obtained from a colony culture inoculated from a Round 2, 3, and 4 colony, respectively. Another lineage (from Fig. 1, dashed blue line)) is shown as a comparison. The envelopes represent 2xSEM as estimated by bootstrapping. **c)** Kymograph of a mutant of Ch SSB PrD that can form selfpropagating aggregates without the presence of the initiation factor (termed Ch SSBmut PrD). YFP fluorescence is shown false colored according to the colormap indicated on the graph. The prion is eventually lost, but rare spontaneous re-formation (green arrow) happens at low inducer concentration (2 μM IPTG for the duration of experiment). The spontaneous re-formation events were observed following large stochastic fluctuations in fluorescence, likely due to plasmid copy number variation. Such fluctuations were also observed in experiments with other PrDs, but in these cases they did not cause re-formation of the prion. **d)** Prion loss curve for different colonies of the Ch SSBmut PrD exhibit similar propagation dynamics (thin line, average in bold, n = 155 cells).

A mutant PrD can form a prion without an initiation factor

To explore the possibility that genetic mutations can be identified that increase prion-forming propensity, we performed random mutagenesis of the PrD-encoding moiety of the Ch SSB PrD construct (**Chapter 2, Materials and Methods 2.9**). We screened for and isolated a mutant (termed Ch SSBmut PrD) that formed dark blue colonies with SDS-stable aggregates even without exposure to the initiation factor New1 (**Fig. S13b**). To investigate whether or not the aggregates

formed by this mutant were propagated in a similar manner to those formed by the Ch SSB PrD, we characterized the dynamic properties of the Ch SSBmut PrD in the microfluidic device. We observed that the mutant aggregates were propagated and lost with similar modes, kinetics, and loss mechanisms as the wild-type Ch SSB aggregates (**Figs. 13c-d, S13a-f**). However, in some rare cases, the mutant protein could spontaneously reform the aggregates, consistent with its ability to access the prion conformation independently of New1 (**Fig. 13c**). We speculate that the Ch SSBmut PrD is a prion domain with a high probability of forming one particular strain. Consistent with this possibility, we found that cells from five distinct colonies exhibited the same kinetics of prion loss (**Fig. 13d**). This mutant will be characterized extensively in another study. Nonetheless, our results indicate that the aggregates formed by the Ch SSBmut PrD are bona fide prions despite their [PIN$^+$]-independence.

Physiological impact of the presence of prions aggregates

We then sought to determine the general physiological impact of such heterologous prion aggregates in *E. coli.* Among eukaryotic prions, it is striking that some are the cause of fatal neurodegenerative diseases while others appear to have low or no toxicity[126,137–139,145]. In bacteria, a potential impact on growth rate (as a proxy for cell viability) is challenging to precisely quantify in bulk due to the different modes of prion propagation as well as the stochastic loss of the prion during growth. Thus, using our microfluidic device, we quantified the growth rate of individual cells that did not have the prion, of cells that maintained old-pole aggregates, and of the cells with small aggregates. Cells with small aggregates had a median doubling time ~1.5% slower than cells without the prion, and cells with old-pole aggregates had a ~3% growth penalty compared to cells without the prion (**Fig. S14a**). We also quantified the death rate of cells propagating the prion, and observed that the death rate was overall very low (~6×10^{-3} /h) and similar to cells not propagating the prion (**Fig. S14b**). We thus concluded that the presence of prion aggregates had a small yet meaningful negative effect on the overall cell physiology.

A stochastic model recapitulates the experimentally observed prion propagation dynamics

Prion propagation in yeast and mammals has been mathematically modeled in various studies[147,150,151,153,168–170]. To investigate if these molecular models can describe the observed dynamics of our system, we adapted a mathematical model of prion propagation for single bacterial cells. In particular, we modeled the propagation and loss of prion aggregates in growing and dividing cells with a stochastic generalization of the nucleated polymerization model[152,153] (**Fig. 14a, details in Chapter 2, Materials and Methods 2.9**). Proteins are produced in the soluble form, and can then be converted in the prion form by elongation of an existing aggregate oligomer. Aggregates can be fragmented into smaller oligomers – keeping the number of monomers constant – and aggregates below a critical size n spontaneously fold back into the soluble form. Cells grow continuously and divide once they reach a critical size, such that proteins are randomly partitioned between the two daughter cells according to a binomial distribution[166,167]. Individual time traces were generated using the Gillespie algorithm, which simulates the stochastic chemical reactions[171].

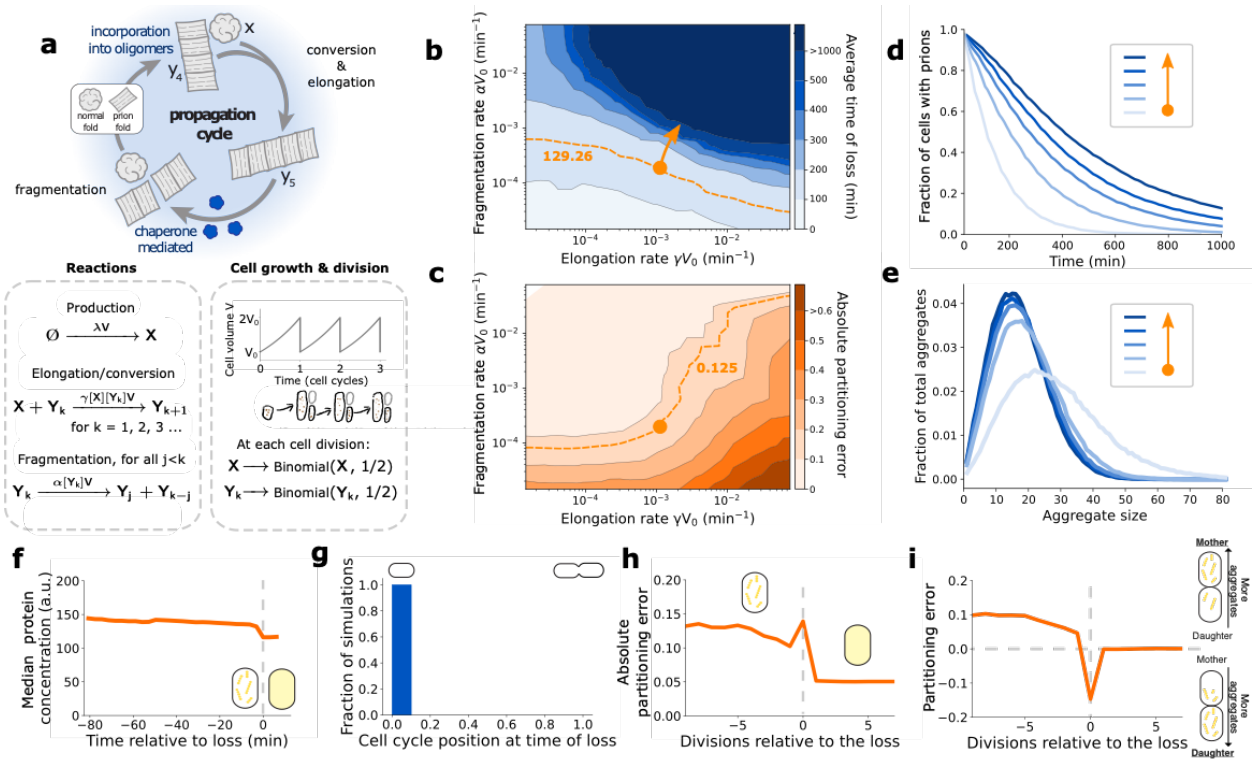

Fig. 14. A stochastic nucleated polymerization model recapitulates the experimental results. a) A stochastic model of prion propagation in growing and dividing cells. Soluble fold protein numbers, denoted by X, are produced constitutively with a rate that scales with the cell volume, so that their concentration becomes cell-cycle independent (see SI 3.2.1). The number of prion fold aggregates made of k proteins is denoted by Yk, where k = 1, 2, 3,…. When a soluble fold protein collides with an aggregate of size k, it can be converted to prion fold by elongating the aggregate to size k + 1. Assuming mass action kinetics, soluble fold proteins are converted to prion fold with a reaction rate proportional to the protein concentrations. Similarly, chaperon mediated fragmentation follows a reaction that is proportional to the aggregate concentrations, with each binding between any two monomers having the same probability of splitting. Concentrations are given by dividing the protein numbers by the cell volume, which grows exponentially from V0 to 2V0 between divisions with a fixed doubling time. At cell division, protein numbers are split randomly, with each soluble protein and each aggregate having a 50% chance of remaining in the cell. **b)** Soluble fold production parameter λV0 was estimated to be 1.75 min−1 by comparing the measured partitioning error of cells after loss of prions with their respective simulations (see SI 3.2.3.2). With no minimal seed size n = 0 (see SI 3.2.5 for n = 2), a parameter sweep of elongation and fragmentation parameters shows that prions in cells with larger fragmentation and elongation rates are more stable. An average time of loss of 129.26 min was measured in the experiment shown in **Fig. 10f**, with the corresponding contour indicated by the dashed orange line. **c)** Cells with smaller fragmentation rates and larger elongation rates have larger partitioning error prior to loss. An absolute partitioning error prior to loss of 0.125 was measured in the experiment shown in **Fig. 11e**, with the corresponding contour indicated by the dashed orange line. Using the two contour plots from b and c we find the model parameters that match the measured time of loss and partitioning error, indicated by the orange dot. **d)** Time of loss curves follow an exponential, in agreement with **Fig. 10f**. Plotted are the time of loss curves for systems with parameters along the solid orange line in **b**. Loss is defined as when Yk = 0 for all k. **e)** The model can predict the aggregate size distribution prior to loss, showing that smaller aggregates are more stable in this parameter regime. **f)** The total protein concentration is approximately constant leading up to the loss, in agreement with **Fig. 11b**. **g)** In this model the prion state is always lost at cell division. **h)** Absolute partitioning errors are larger before the loss, in agreement with Fig. 2e. **i)** A large negative partitioning error occurs at the time of loss, in agreement with **Fig. 11f.**

First, we simulated the model in a large parameter space of elongation and fragmentation rates (**Fig. 14b-c**). We found that systems with large elongation and fragmentation rates were more stable as they take longer to lose the prions. Outside of this parameter space, however, the prion was eventually lost on timescales similar to our experiments. We then estimated the elongation and fragmentation rates by selecting the unique model parameters that matched the observed loss rates and partitioning errors as indicated in **Fig. 14b-c** (see **Chapter 2, Materials and Methods 2.9**for details). Strikingly, this simple model could recapitulate all the observations from the experiments. We find that simulated cells reached a quasi-stationary state, where the distribution of prion aggregates (**Fig. S15a-d**), the total amount of protein (**Fig. 14f**), and the absolute size of partitioning errors (**Fig. 14h**), were approximately constant prior to the loss. As observed experimentally, a large partitioning error into the untracked cell was observed at the moment of loss (**Fig. 14i**), which happened at cell division (**Fig. 14g**). Finally, the loss curve in the population followed an exponential decay, corresponding to constant probability of loss over time (**Fig. 14d**). The model also shows how different prion conformations, with potentially different elongation and fragmentation rates, can lead to different stabilities.

Using this model, we predicted that cells with larger volumes would have lower partitioning errors, which would make the prion more stable (**Fig. S15e-f**). To test this prediction, we used a mutant with longer cell size but with the same growth rate (*ftsN* deleted of codons encoding amino acid residues 244-319[172], **Fig. S16a,b,d**), which revealed that ~ 50% fewer cells lost the prion during replating experiments (**Fig. S16c**). We thus concluded that partitioning errors played an important role in the loss of the prion, that cell volume affects prion loss, and that the nucleated polymerization model was consistent with our experimental results.

3.5. Discussion

Here, we used microfluidics and fluorescence microscopy to track thousands of individual cells propagating prion aggregates. Notably, cells tracked for over 20 generations with the prion would have likely renewed almost every single protein in the cell (and thus the prion proteins many times), showcasing the self-propagating nature of the prion aggregates. For proteins that are not degraded, half of the proteins are renewed after one cell division. Thus, after 20 cell divisions, $1/2^{20}$ of the ~ 2^{21} original proteins will not have been renewed, such that only a handful of the original proteins will remain[173,174].

Modes of propagation

We discovered that, for the three PrDs studied, the prions were propagated through two modes: stable old pole aggregates and less stable small aggregates (**Fig. 15**).

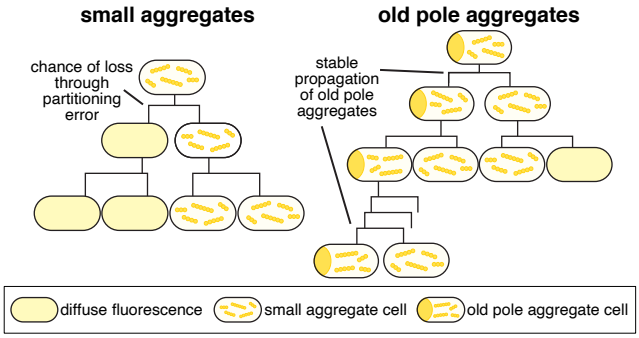

Fig. 15. **Schematic of the two observed modes of prion propagation.** Cells with small aggregates have a probability of losing the prion at each cell division through partitioning errors. At cell division, an old-pole aggregate cell generates a small aggregate cell and an old-pole aggregate cell. Although the old-pole aggregate is very stable, the cells containing old-pole aggregates represent a small fraction of a growing culture. The small aggregate cells generated through this division presumably propagate the prion similarly to the other observed small aggregate cells.

We note that the old-pole aggregate cells also contain small aggregates which can be difficult to visualize due to the brightness of the large aggregate. Therefore, at division, the old-pole cells generate one cell bearing an old-pole aggregate and one bearing small aggregates (**Fig. 15**). We have not investigated the formation of these old-pole aggregates, but speculate that they can be formed stochastically once an aggregate reaches a critical size. This critical size would prevent them from freely diffusing through the cell and confine them to the pole, while potentially also preventing chaperones from fragmenting them normally. It remains to be determined if other PrDs, from bacteria or other organisms, exhibit this type of propagation. Yet, we conjecture that these old-pole aggregate cells could form a rare yet stable reservoir of the prion epigenetic state, generating cells containing small aggregates at each cell division.

In contrast, the cells containing the small aggregates lost the prion relatively quickly, with a constant rate of loss over time (memoryless process with half-life of ~2-6 generations). We note that this stability will depend on the concentration of the prion protein, which was kept as low as possible during these experiments. The loss of the prion in these cells was driven mainly by a sudden mis-partitioning of prion aggregates at cell division, giving a probability of losing the prion at each cell division (**Fig. 15**), consistent with the memoryless loss kinetics. It remains to be determined if other bacterial PrDs, such as the Rho PrD from *Clostridium botulinum* (which had a lower rate of loss during replating[129]), are propagated and lost similarly.

Different lineages have different stability

In addition to disentangling the modes of propagation at the single-cell level, our microfluidic assay enabled precise quantification of the loss kinetics. This enabled us to observe that distinct lineages of the same PrD could propagate aggregates with distinct stabilities. In particular, we characterized one lineage of the Ch SSB prion that had a stability an order of magnitude greater than the others. This finding recapitulates and extends observations made in the previous study of the Ch SSB PrD, where both low-propagation and high-propagation lineages were

characterized[128]). These results are reminiscent of what has been observed in yeast, where one protein (e.g. Sup35) can form multiple self-propagating structures, called strains, with different stabilities (e.g. $[PSI^+]^{strong}$ vs. $[PSI^+]^{weak}$)[147,162,175–177]. Further work will be necessary to show whether the different lineages observed reflect different self-propagating structures.

In contrast, we characterized a mutant PrD that could form self-propagating aggregates without an initiation factor (independently of $[PIN^+]$). We conjecture that this mutant is a PrD with a high probability of forming one particular self-propagating structure, similar to how certain mutations of the mammalian PrP lead to the formation of a particular prion strain in genetic prion diseases (e.g. familial CJD)[178–180].

Molecular model of prion propagation and challenges in bacteria

Finally, we developed a stochastic implementation of the nucleated polymerization model that could recapitulate all the observed single-cell properties. In the future, the simple model could be tested further by perturbing the experimental parameters, e.g., by changing the concentration of the disaggregase ClpB (required for the propagation of the Ch SSB prion). This would indicate whether additional constraints that have been necessary to explain results in yeast, such as a size-dependent transmission of aggregates[170] or different seed size for prion strains[151], are also necessary. This model also reveals challenges for prion propagation in bacteria. Using the experimental measurements (partitioning errors and the average time of prion loss), we can estimate the total number of proteins, the fragmentation rate, and the elongation rate, and thus obtain an approximation for the replication rate ($k = \sqrt{[monomer] \cdot \gamma\alpha}$, see **Chapter 2, Materials and Methods 2.9**). Even though the PrDs studied here appear to be lost relatively quickly, the estimated replication rate (~ 10^{-5}/s) is of similar order of magnitude to other prions, such as the mammalian PrP *in vivo*[150].

How does the model explain the discrepancy between the fast replication rate and the prion instability? *E. coli* is small and therefore has low numbers of proteins, which results in high partitioning errors. For example, the total number of proteins is ~100 times smaller in *E. coli* than in *S. cerevisiae,* which would result in partitioning errors ~10 times larger (i.e. Embedded Image). In addition, *E. coli* divides rapidly, which further reduces the stability of the prion, as proteins need to be converted to the prion state prior to the division for stable propagation. The lower stability we observed contrasts with what was observed in yeast, with e.g., a loss rate of 10^{-5} $generations^{-1}$ for $[PSI^+]$. Nevertheless, we speculate that less stable PrDs do not make them less useful as an epigenetic switch. Prions have been suggested to provide an epigenetic state with fitness advantage under certain environmental conditions[132–134,143,144]. The optimal stability of such an epigenetic state depends on the rate of change of the environment experienced by the organism, which is difficult to estimate. Thus, whether a loss rate on the order of generations (for the PrDs studied here) or tens of thousands of generations (e.g. yeast $[PSI^+]$) is more or less useful biologically depends on temporal dynamics of the environment.

In conclusion, this work further establishes the conservation of prion propagation across domains of life. Further work will unravel how many of the thousands of predicted prokaryotic candidate PrDs can form prions, and how prion formation affects cell physiology.

4.5. Supplementary Results and Discussion

Supplementary results and discussion can be found in the following link under section 3 of the document: https://www.biorxiv.org/content/10.1101/2023.01.11.523042v1.supplementary-material

Chapter 5: Conclusion and future directions

In **Chapter 3** of this thesis, the study of EcN's osmolality transcriptional response allowed the selection of three osmolality-specific genes and their respective promoters (five) as candidates for gut osmolality biosensors. This was done through RNA-seq and differential gene expression analysis. The selection of these promoters considered their gene expression levels (over twofold) in the conditions assayed and their reported functionality in the literature. As mentioned before, all the genes selected have cross reactivity with at least one more condition, which is why further promoter reactivity analysis is necessary at an *in vitro* and *in vivo* levels. Furthermore, it was revealed that gene expression during stationary phase was an important factor to select genes that responded specifically to osmolality. It will be important to study the genes responding to osmolality in stationary phase with the other osmolytes assayed (PEG, lactulose, and sorbitol).

This study provides a starting point for gut osmolality biosensors using the probiotic strain EcN. Likewise, it showed that characterizing the transcriptional response of this bacterium revealed gene expression patterns that had not been reported in other strains of *E.coli*, providing more options for building biosensors of gut biomarkers. In the future, these promoters will be validated *in vivo* and further paired with stable fluorescent proteins (FPs) and genetic memory elements to report on local osmolality changes along the gut. In the long term, these biosensors would be encapsulated, released in the human gut, collected from the stool of patients and analyzed by clinicians to diagnose conditions and personalize microbiome interventions.

Separately, **Chapter 4** of this thesis also studied prion propagation and loss in single bacteria using microfluidics and fluorescence microscopy. It was shown that the propagation occurs in two distinct modes with distinct stability and inheritance characteristics. It was found that the prion is lost through random partitioning of aggregates to one of the two daughter cells at division. Extending these findings to prion domains from two orthologous proteins, similar propagation and loss properties were observed. These findings also provide support for the suggestion that bacterial prions can form more than one self-propagating state. A stochastic version of the molecular model of prion propagation from yeast and mammals recapitulates all the observed single-cell properties. This model highlights challenges for prion propagation that are unique to prokaryotes and illustrates the conservation of fundamental characteristics of prion propagation across domains of life.

Appendix

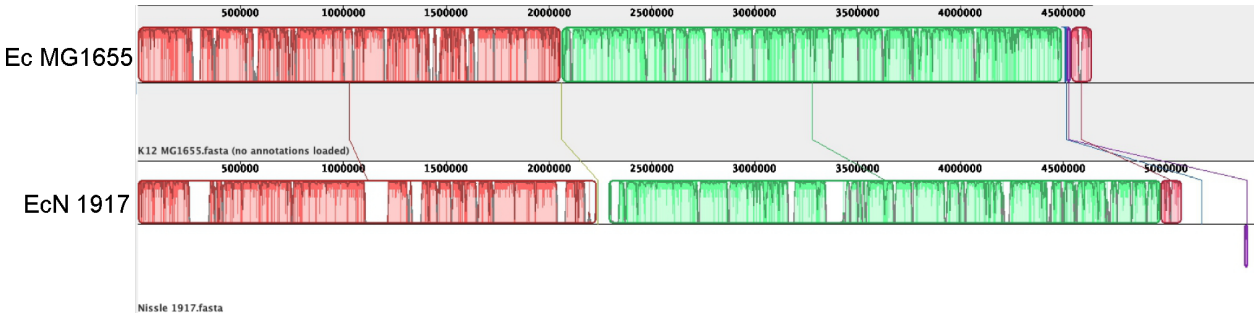

Figure S1. Whole genome alignment reveals 1,000 different coding sequences (CDS) between *E. coli* MG1655 and *E. coli* Nissle. Alignment was made with Mauve software [181].

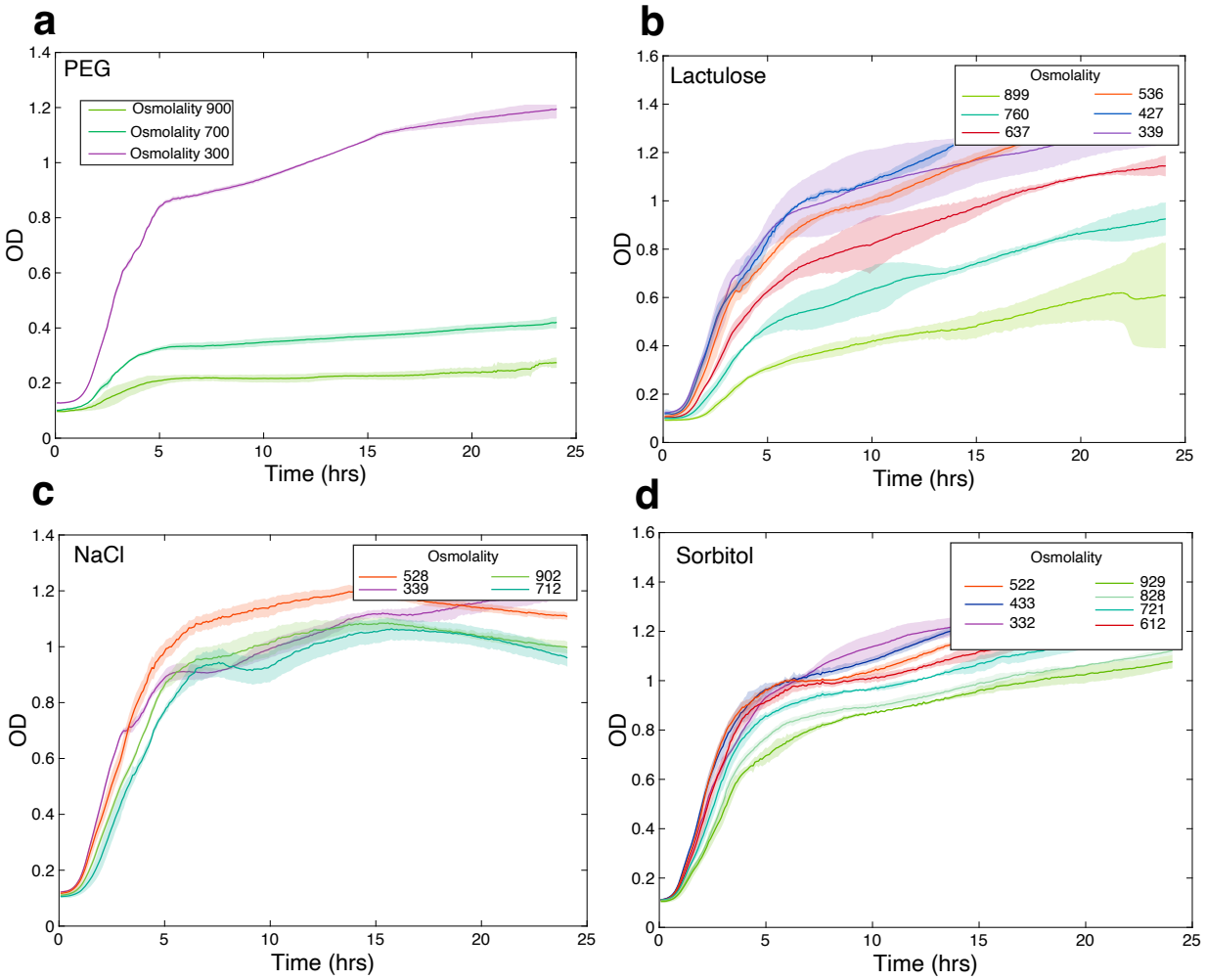

Figure S2. Growth curves (OD in function of time) of EcN in untreated (LB) and treated (LB+osmolyte) rich media. Multiple levels of osmolality were evaluated for each osmolyte: **a)** PEG; **b)** Lactulose; **c)** Sodium chloride (NaCl); and **d)** Sorbitol. Osmolality values are expressed in mOsm/kg. For every condition, 3 biological replicates were made. The curves represent the average of the replicates, while the shaded area represents the standard deviation.

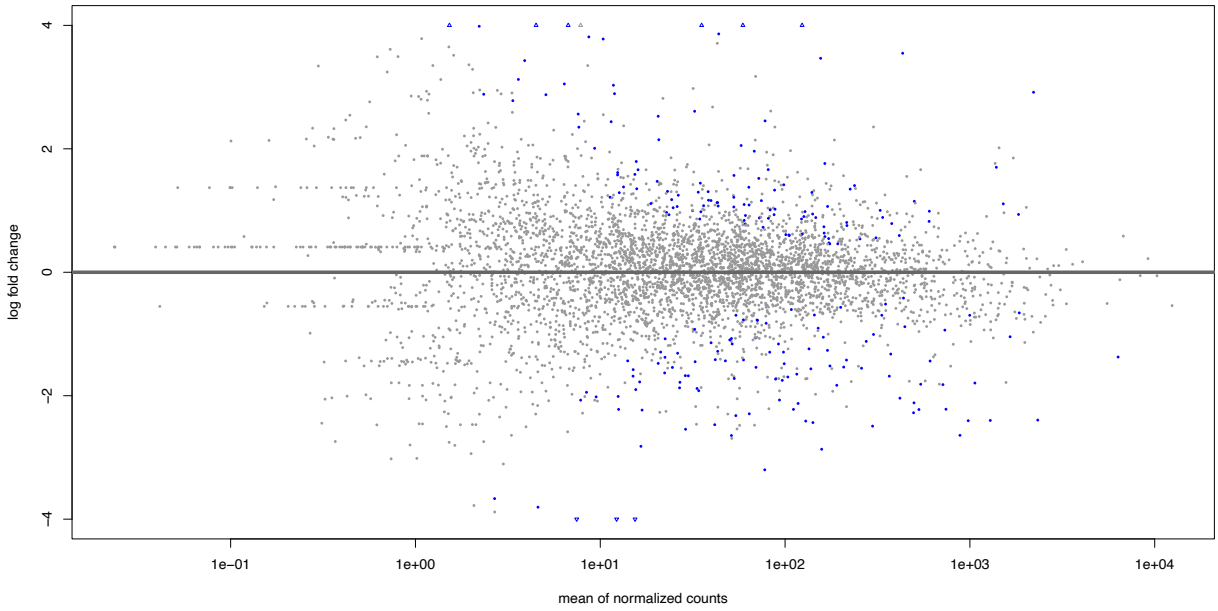

Figure S3. MA-plot showing the mean of normalized counts of all the samples for each gene in function of the log2 fold change. Data shown without LFC shrinkage. Data points coloured in blue have an adjusted p-value less than 0.1. Data points that fall out of the window (-4,4) are shown in triangles.

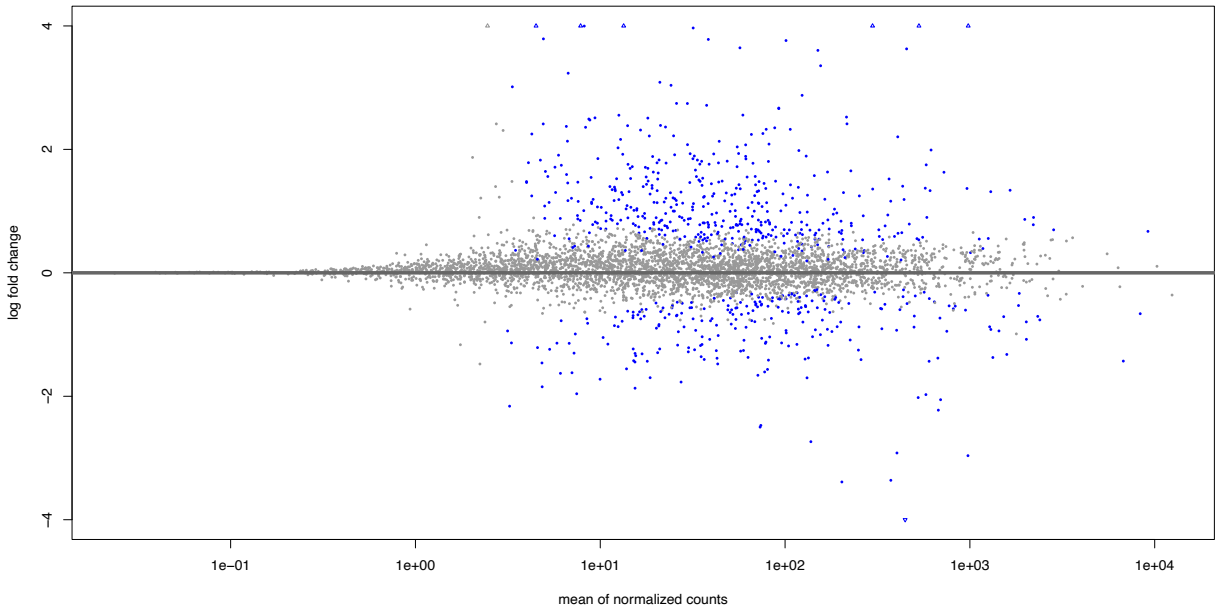

Figure S4. MA-plot showing the mean of normalized counts of all the samples for each gene in function of the log2 fold change. Data shown with LFC shrinkage. Data points coloured in blue have an adjusted p-value less than 0.1. Data points that fall out of the window (-4,4) are shown in triangles.

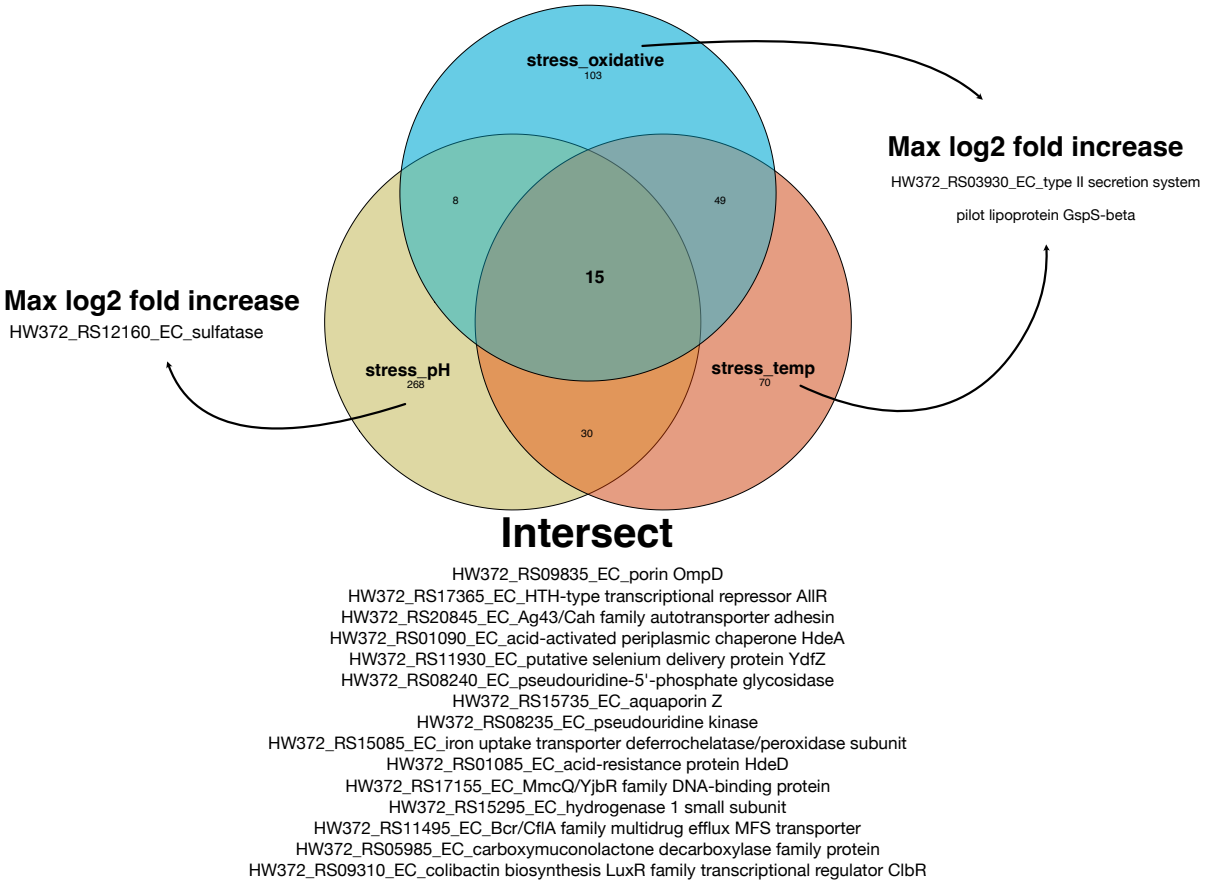

Figure S5. Relationship between overexpressed genes in general stress conditions. A 3-way Venn diagram between acidic pH stress (5.8), oxidative stress (100 uM hydrogen peroxide) and high temperature (42°C) shows 15 genes are significantly over expressed in the three conditions. The identity of these genes is displayed under Intersect. The genes with the highest log2 fold increase for each individual condition are also displayed.

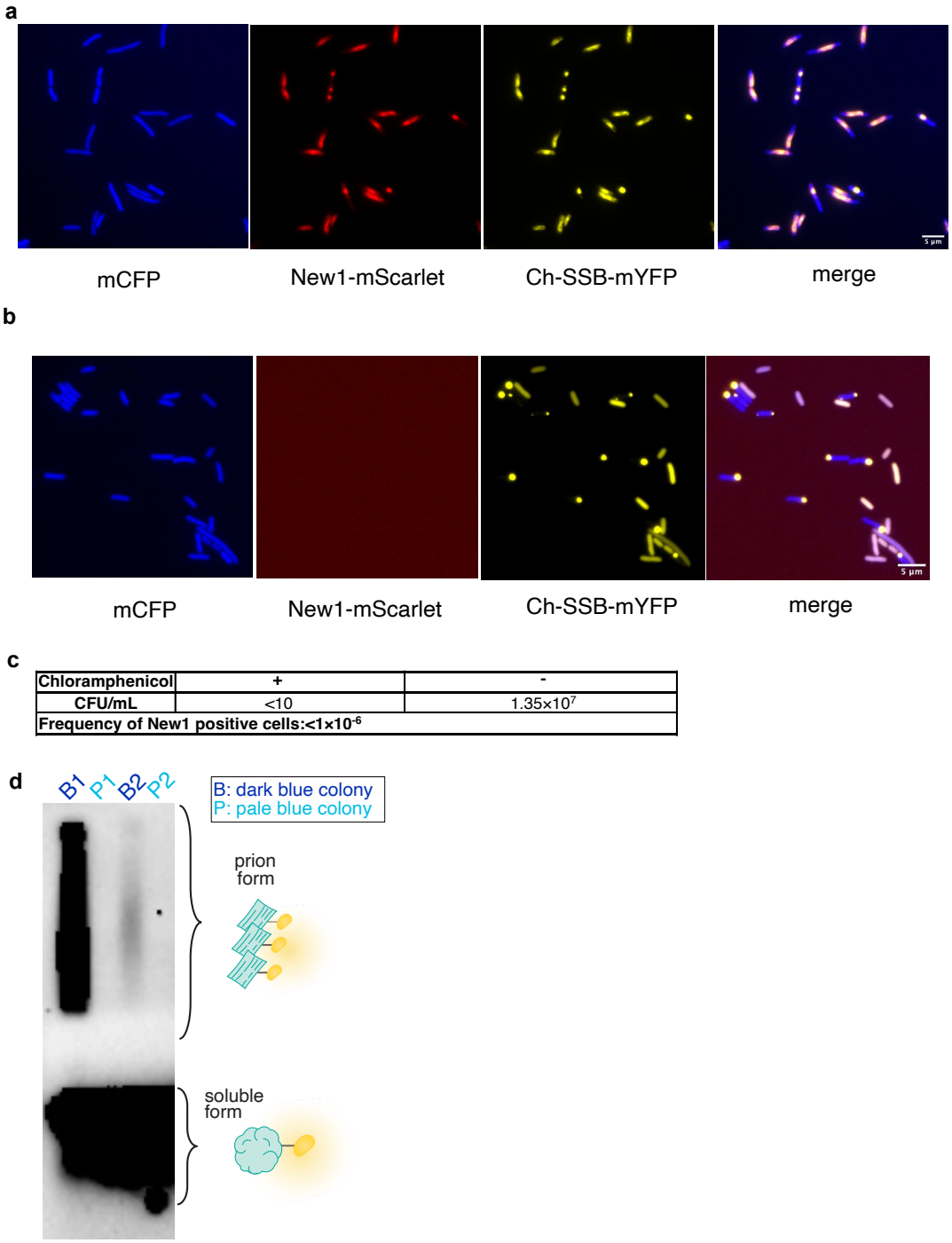

Fig. S6. Complete curing of New1-mScarlet-I-expressing temperature sensitive plasmid and subsequent induction of prion formation a) Fluorescence microscopy of cells that harbor Ch SSB PrD before curing of the New1-mScarlet-I plasmid. The cells express CFP constitutively (for cell segmentation and tracking), mEYFP (fused to Ch SSB PrD) and mScarlet-I (fused to New1). **b)** Fluorescence microscopy of cells that harbor Ch SSB PrD after curing the temperature sensitive plasmid at 37°C overnight shows hat no New1-mScarlet signal is detected. **c)** Plating of a culture used for microfluidic experiment shows that no cells contain the cured New1-expressing plasmid. CFU/ml of cells grown overnight with and without chloramphenicol (resistance marker of New1-mScarlet-I plasmid). No colonies are observed in the presence of chloramphenicol. **d)** SDD-AGE shows that dark blue colonies contain SDS-stable aggregates, whereas pale colonies contain only soluble Ch SSB PrD. Prion formation was previously induced with New1-mScarlet-I and then the cells were cured of the New1-mScarlet-I plasmid.

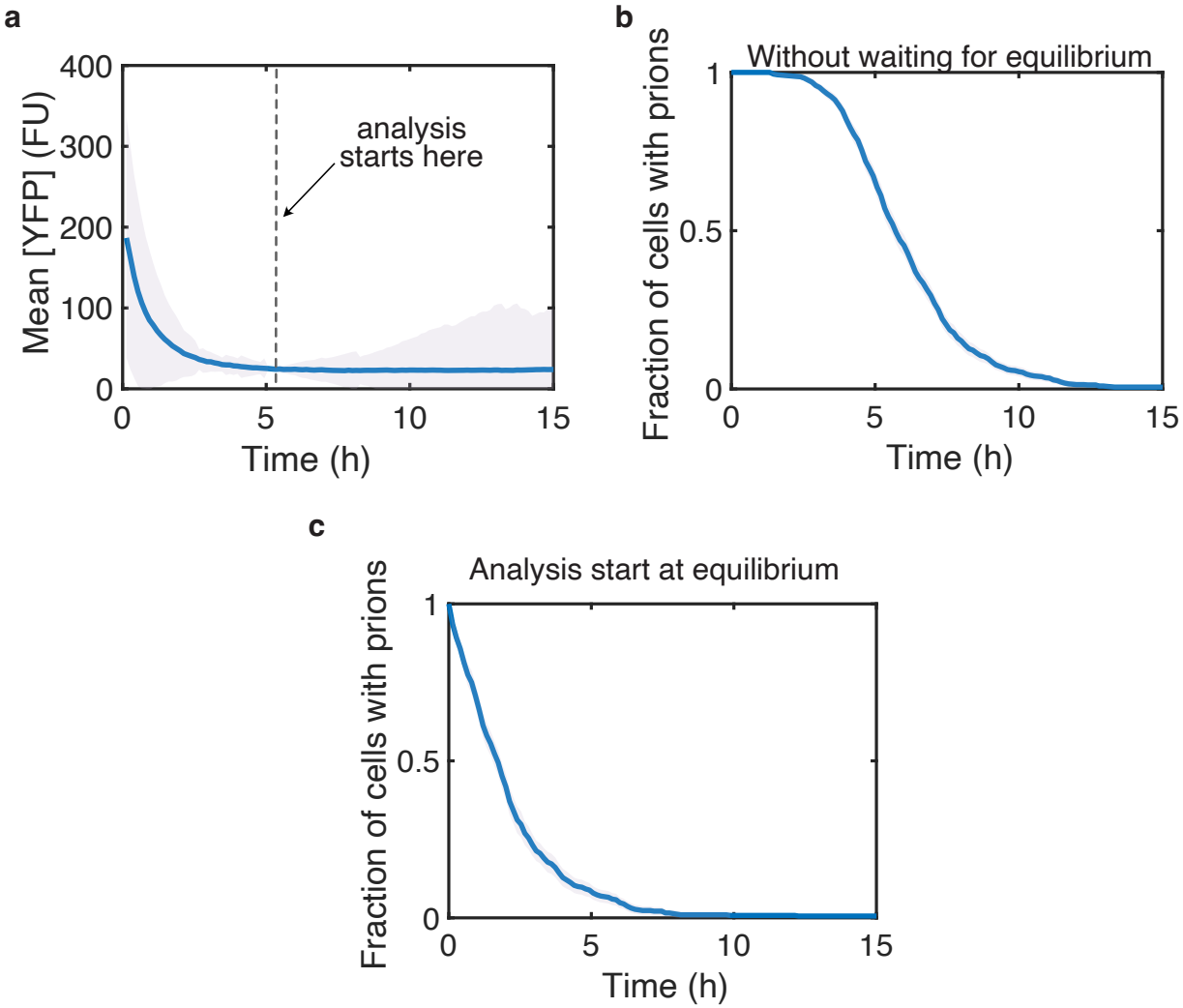

Fig. S7. Equilibration of growth conditions in the microfluidic device prior to beginning the analysis. a) The concentration of the Ch SSB PrD (as reported by its fused YFP) reaches equilibrium after ~5h in the device. Average concentration of YFP fluorescence for the cells in the device over time (n = 947 cells), where the dashed line indicates where the analysis starts for the experiment. The decrease in YFP fluorescence is due to the change of the concentration of IPTG from 10 μM outside the device to 0 μM in the device. **b)** and **c)** Prion loss curve with the analysis starting immediately with the imaging (b, n = 947 cells) and with the analysis starting when growth conditions are at equilibrium (c, n = 614 cells). The envelopes indicate 2xSEM (estimated by bootstrapping for b and c).

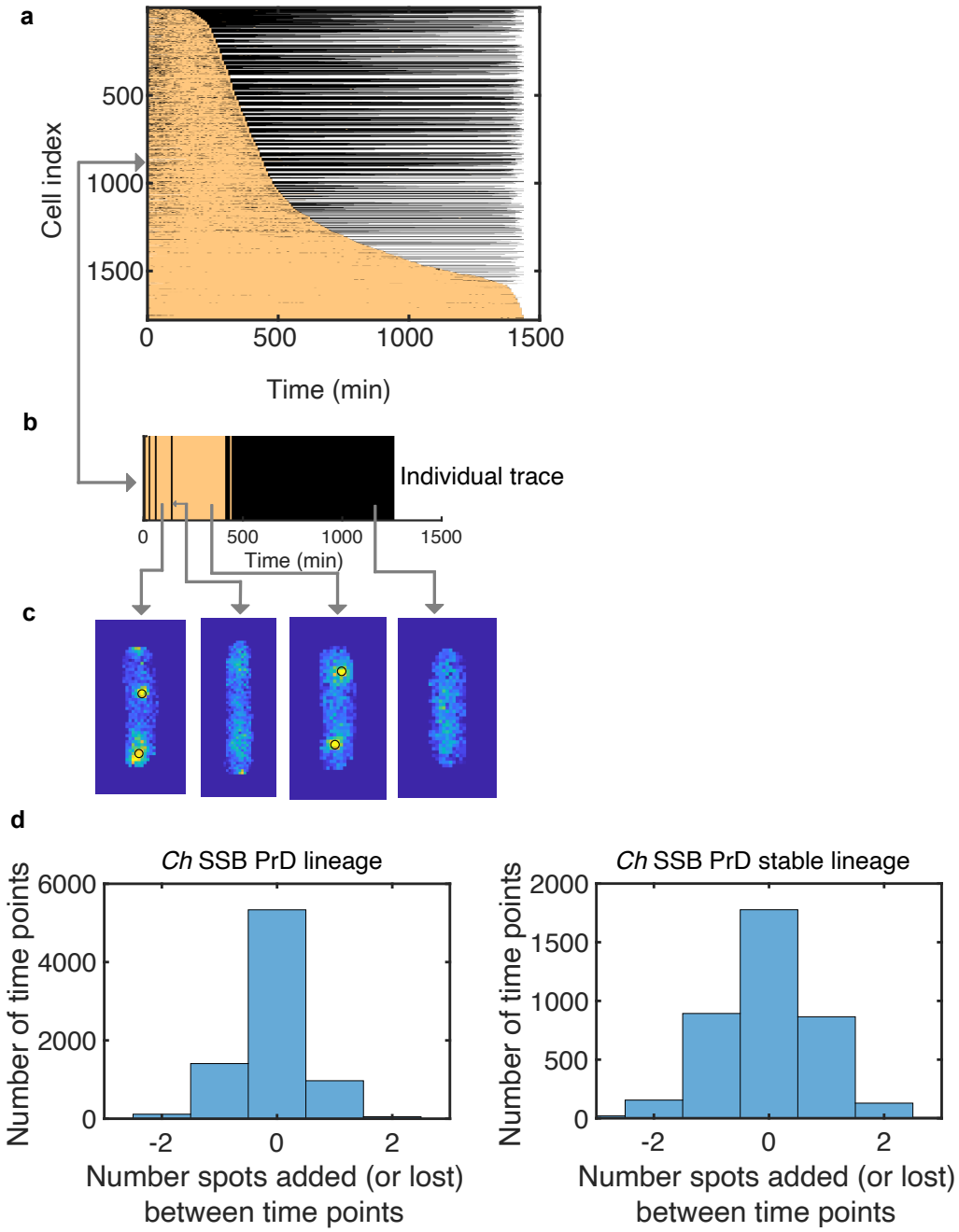

Fig. S8. Estimation of prion loss using a spot-finding algorithm. a) Cell traces ordered by the duration of prion propagation, with the coloration indicating the presence (beige) or absence (black) of spots, as determined by a spot-finding algorithm. The prion loss was called the first time 8 subsequent time points have no aggregates. b) One example cell trace showing the irreversible loss of the prion aggregates. Aggregates are sometimes not detected during the prion propagation phase, presumably because the size of the aggregates is below the detection limit. **c)** Example images of the cell tracked in **b)**, showing the detection of the aggregates using the spot-finding algorithm (black circles). **d)** Aggregates are added and removed during the tracking of the cells in the device. Histogram of the difference in the number of detected aggregates in between time points for the Ch SSB lineage of Fig. 1 (left, n = 586 cells) and the ultra stable lineage of Fig. 4b (right, n = 553 cells).

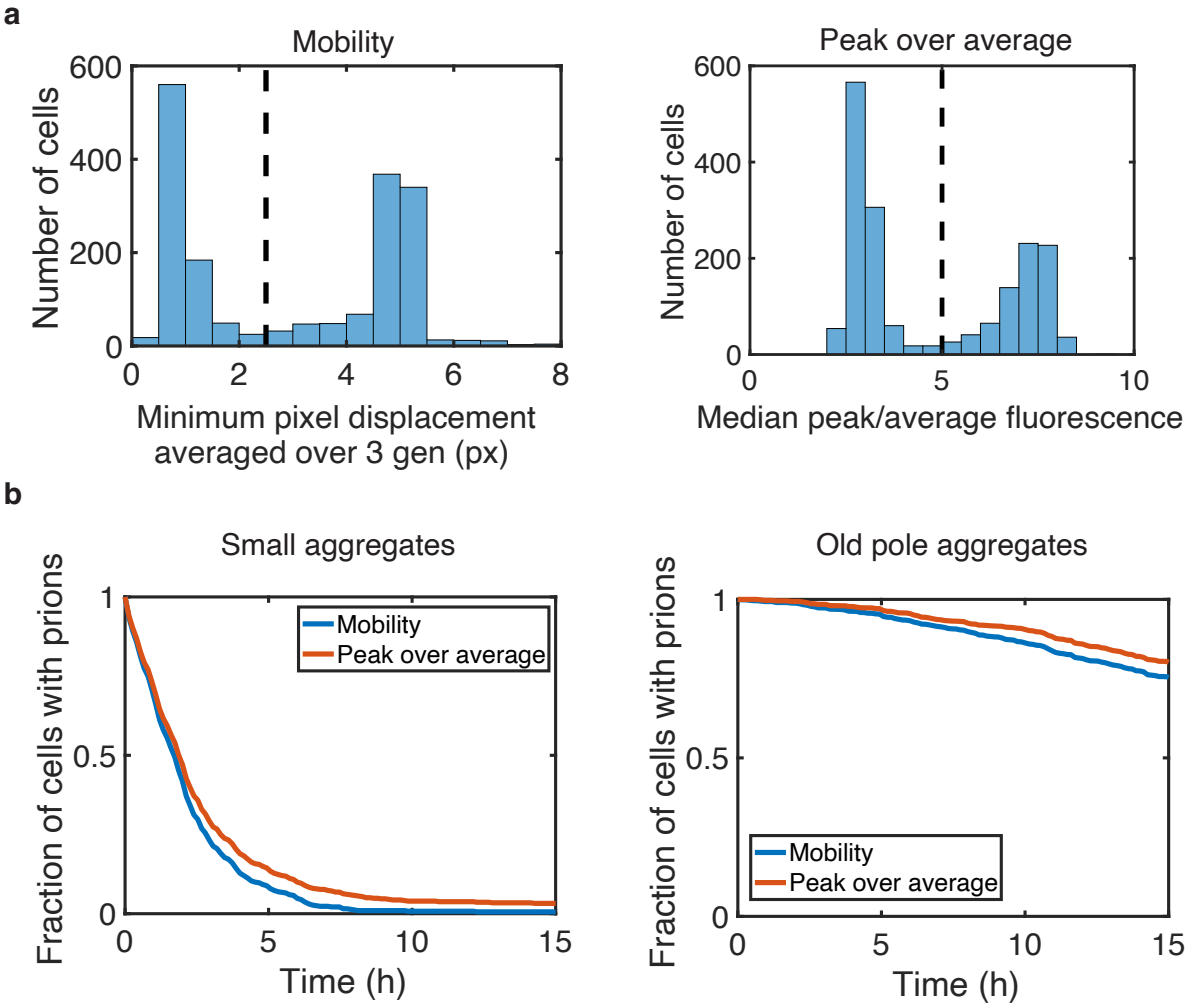

Fig. S9. Two methods for classifying aggregates give similar results. a) (Left) Aggregates can be distinguished by measuring movement of the aggregate over time (mobility), with old-pole and small aggregate cells displaying low and high mobility, respectively. Histogram of minimum movement of aggregates averaged over three generations for each cell. (Right) Alternatively, aggregates can be classified by their fluorescence intensity, with old-pole aggregates being brighter. Histogram of peak fluorescence intensity (median of top 10% of pixels in the cells) divided by the average fluorescence intensity. Dashed lines represent the thresholds for classification of aggregates as small or old-pole types (n = 1,788 cells). **b)** Prion loss curve for the small (left, n = 614 cells for mobility and 681 cells for peak over average) and old-pole aggregates (right, n = 831 cells for mobility and 764 cells for peak over average), with the classification performed using the mobility (blue) or the fluorescence intensity (red) thresholds of a).

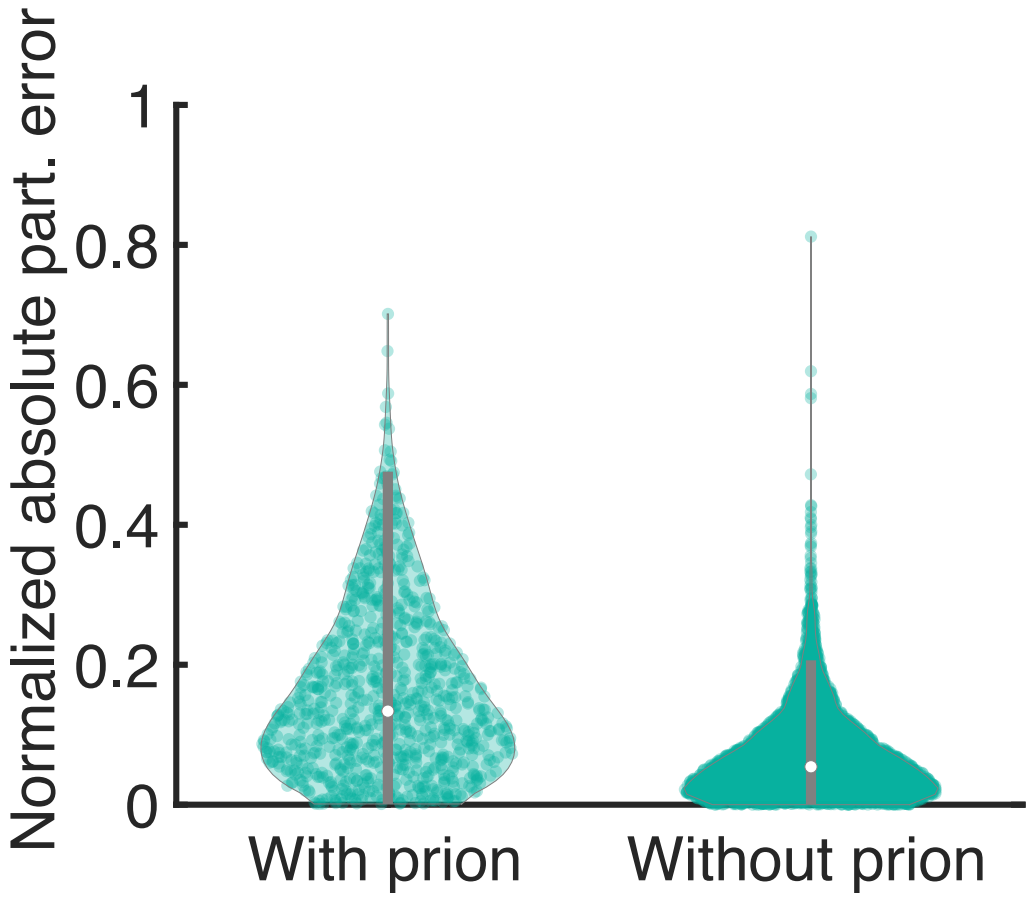

Fig. S10. The partitioning errors are greater when the cells contain prions. Violin plot showing the distribution of absolute partitioning errors (|YFPmother − YFPdaughter|/(YFPmother + YFPdaughter) for cells that contain prion and after they lost the prion (n = 886 cell division with the prion, 4,997 divisions without the prion). The partitioning errors are on average larger and there are more frequent extreme partitioning errors when cells contain prion aggregates.

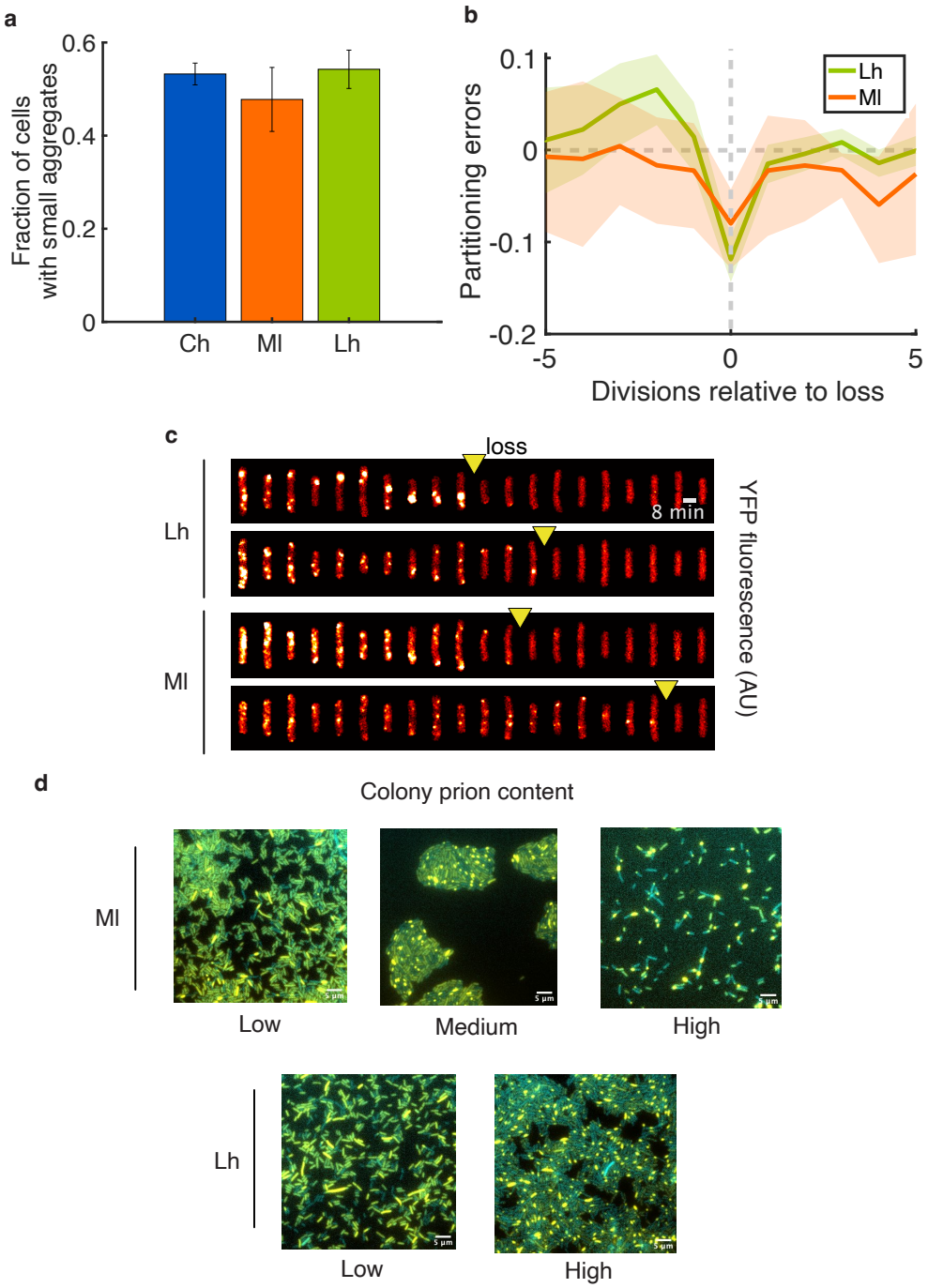

Fig. S11. **Orthologous SSB PrDs form self-propagating prion aggregates with similar properties. a)** Fraction of cells that contain small aggregates (as opposed to old-pole aggregates) for cells containing the Ch SSB (blue, n = 1,779 cells), Ml SSB (orange, n = 224 cells), or Lh SSB (green, n = 601 cells) prions. **b)** The orthologs also show a transfer of fluorescence to the untracked cell at the moment of prion loss, as shown in the partitioning errors in the divisions relative to the loss (Lh, green line, n = 99 cells, Ml, orange line, n = 29 cells). **c)** Kymographs showing the propagation and loss of the prion aggregates for the two orthologs, where the yellow triangles indicate the losses identified using the spot-finding algorithm. **d)** Fluorescence microscopy of dark blue colonies with Lh SSB PrD and Ml SSB PrD. The YFP is shown in yellow (SSB PrD fusion) and the CFP (constitutive marker for segmentation) is shown in cyan. Cells with prions show aggregated fluorescence, and cells without prions show diffuse fluorescence. The fraction of cells with prions can differ between different colonies, presumably due to the stochastic loss of the prion during the colony forming process.

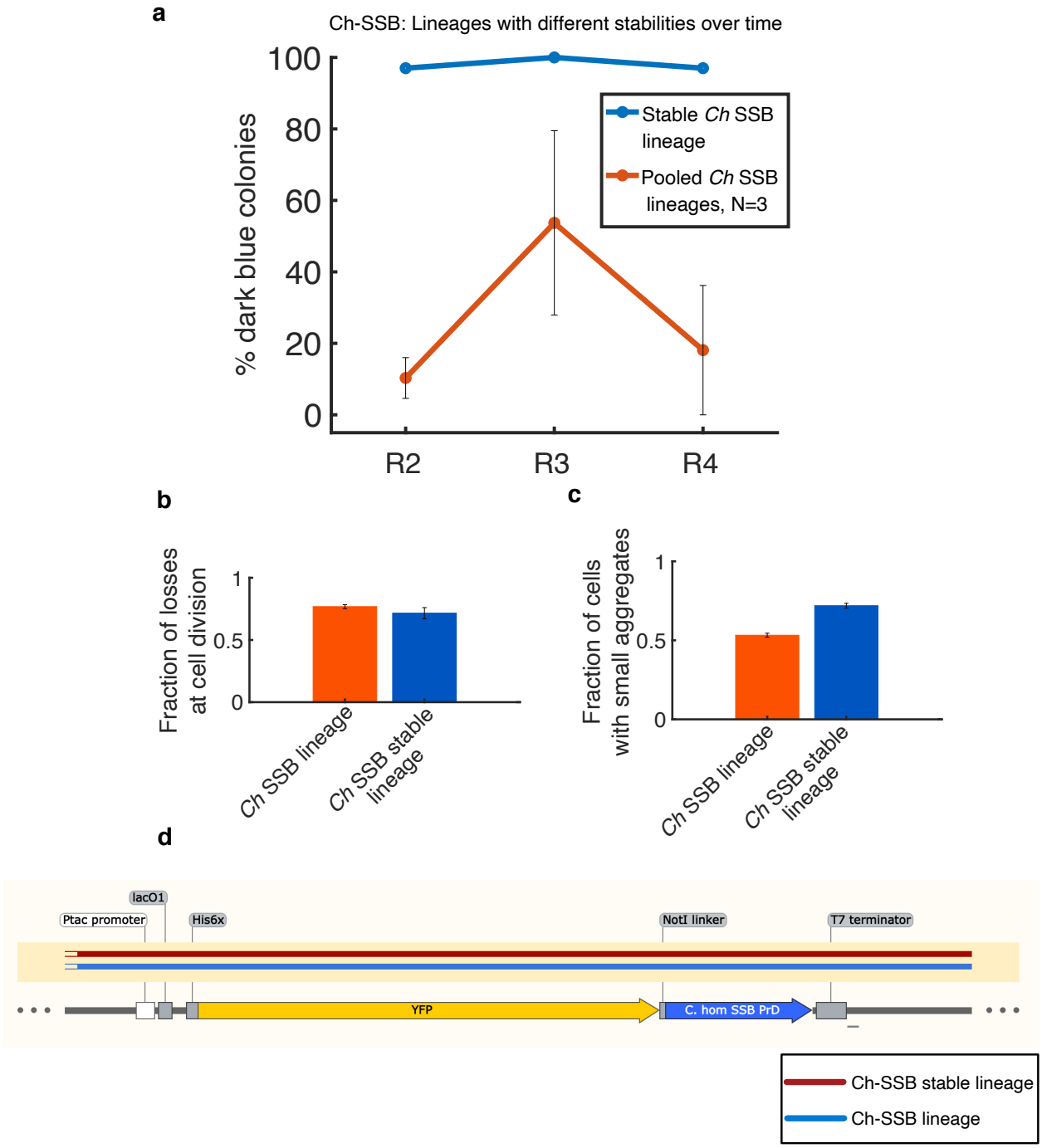

Fig. S12. One lineage propagates the Ch SSB prion with very high stability. a) The stability of the prion is kept over multiple rounds of growth. The stable lineage (blue) and a pool of Ch SSB prion-containing colonies (red) were grown and replated for multiple rounds, and the fraction of colonies with prion-containing cells was estimated using the PclpB-lacZ reporter. R2, R3, and R4 designate the colonies obtained after plating the Round 1, Round 2, and Round 3 colony cultures, respectively (see Fig. 4b). While the pooled colonies show a fraction of colonies with prion-containing cells between 10% and 50%, the ultra-stable lineage has close to 100% during each replating. The properties of the ultra-stable lineage are similar in the microfluidic device, where most losses happen at cell division **(b)**, and with a similar fraction of cells with small aggregates **(c)**. **d)** DNA sequencing of the plasmid containing the PrD-YFP fusion in the stable lineage shows no mutations.

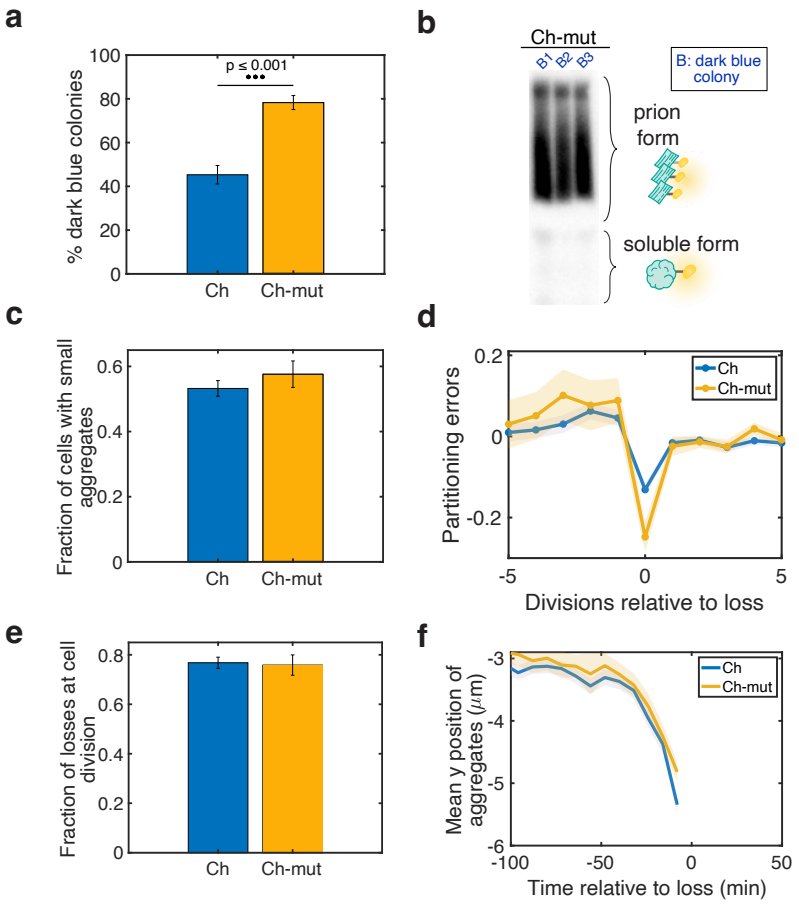

Fig. S13. A mutant Ch SSB PrD (Ch SSBmut) forms self-propagating aggregates without exposure to New1 with similar properties to those formed by the Ch SSB PrD. a) Percentage of dark blue colonies (indicating prion-containing cells with the PclpB-lacZ assay) upon replating single blue colonies shows that the mutant has a higher fraction of colonies with prion-containing cells (p = 4.1e-04). **b)** SDD-AGE of 3 colonies of the mutant shows the presence of insoluble aggregates. **c-f)** The mutant domain exhibits similar properties to the WT domain as assayed by our microfluidic assay. The fraction of cells with small aggregates (c, n = 1,779 cells for the WT and 578 cells for the mutant), the partitioning errors relative to the loss (e, n = 349 cells for the WT and 125 cells for the mutant), the fraction of losses at cell division (e, n = 754 loss events for the WT and 207 loss events for the mutant), and the position of the aggregates (f, n = 754 cells for the WT and 207 cells for the mutant) are similar for both PrDs.

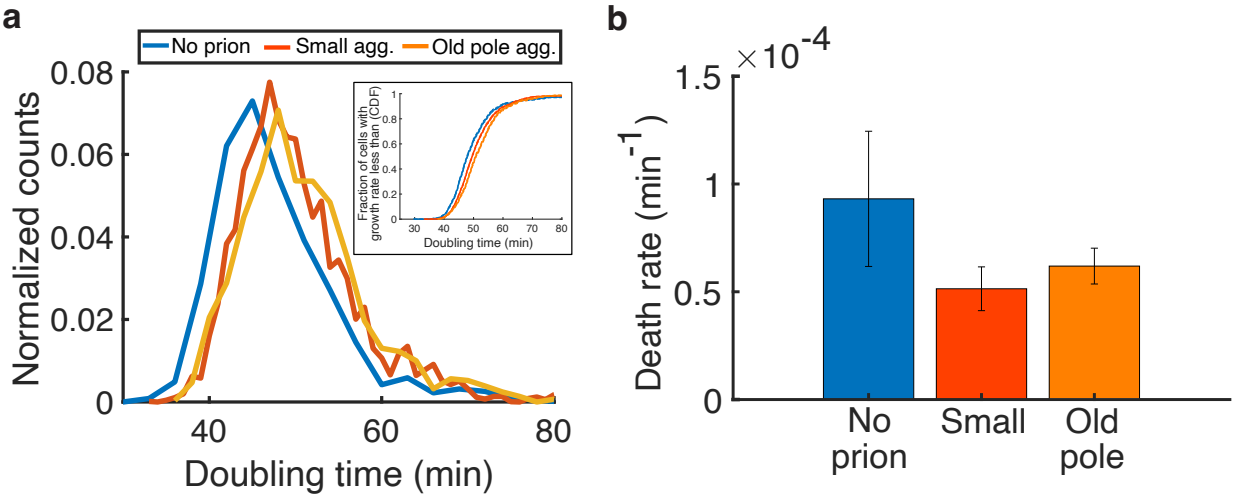

Fig. S14. Propagation of the Ch SSB prion imposes a slight growth rate penalty on the cells. a) Histogram of estimated doubling time in the microfluidic device for cells without the prion (blue), with the small aggregates (red), and with the old-pole aggregates (yellow, n = 6,767 time points without the prion, 14,154 with small aggregates, and 5,952 with old pole aggregates). The median doubling time is ~1.5 min greater for cells with small aggregates and ~3 min greater for cells with old-pole aggregates as compared to cells without prions. (Inset) Cumulative distribution function (CDF) of the doubling time. **b)** Estimated death rate in the microfluidic device of cells without prions (blue), with small aggregates (red), and with old pole aggregates (yellow, n = 8 cells deaths without the prion, 23 with small aggregates, and 50 with old pole aggregates out of 10,740 min, 55,936 min, and 100,943 min observed, respectively).

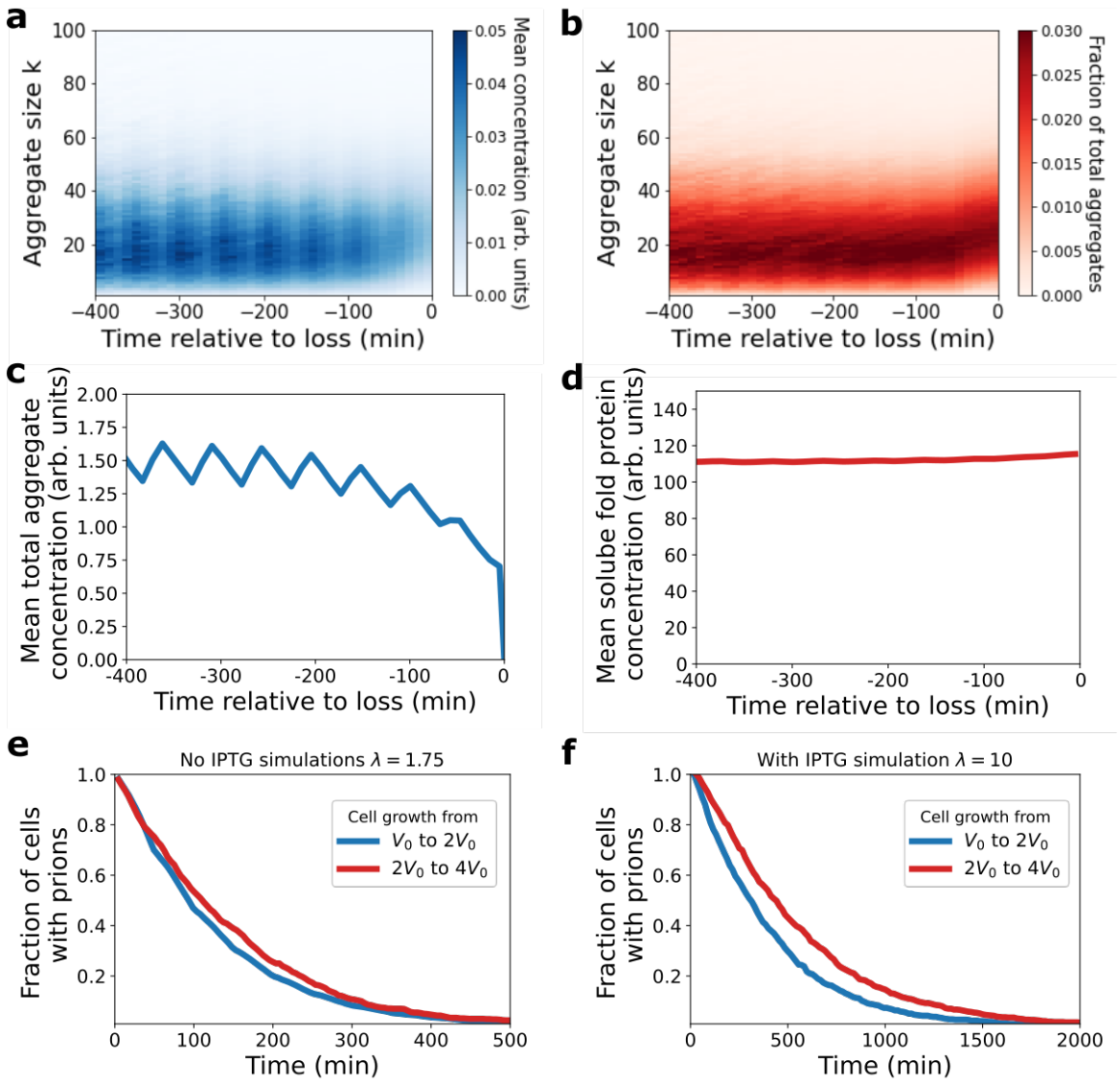

Fig. S15. The distribution of aggregate size reaches a quasi-stationary state before the time of prion loss in the simulations of our stochastic model. a) The distribution of aggregate concentrations is cyclo-stationary prior to 200 minutes before loss. The division time here is 50 min. The y-axis corresponds to the aggregate size k where k is the subscript in Yk. Time is binned in bins of 10 minutes, and average concentrations are computed in each bin taken over 100,000 simulations. **b)** The distribution of the fraction of total aggregates is constant prior to loss except for a slight growth in aggregate size right before the loss. The fraction of Yk was computed in each time bin i as hy i k i/ P j hy i j i. **c)** The mean total aggregate concentration, P k yk/V , is cyclo-stationary prior to 200 min before loss. Aligning the cells at the time of loss effectively aligns the division times because in the model the division time is constant. Mother cells that keep the prion at division tend to gain prion concentration at division because the partition is on average positive, see Fig. 5i of the main text. **d)** The average soluble fold protein concentration hX/V i is constant prior to loss except for a slight increase right before the loss. **e)** The model predicts that the prion is more stable in cells with larger sizes. This is because in order for the concentrations of molecules to be identical between small and large cells, larger cells need to have higher numbers of molecules, thus reducing partitioning errors. Each curve corresponds to 1000 simulations with a fixed cell division time of 50 min. Model parameters were estimated as described in Fig. 5 and the SI 3.2 to model the mother machine experiments where there is no IPTG. **f)** In the replating experiments, cells are grown in 10 µM IPTG. In the model, this corresponds to an increase in the soluble fold protein production parameter λ. Setting λ = 10, we find that the difference in prion stability is more stark between small cells and large cells.

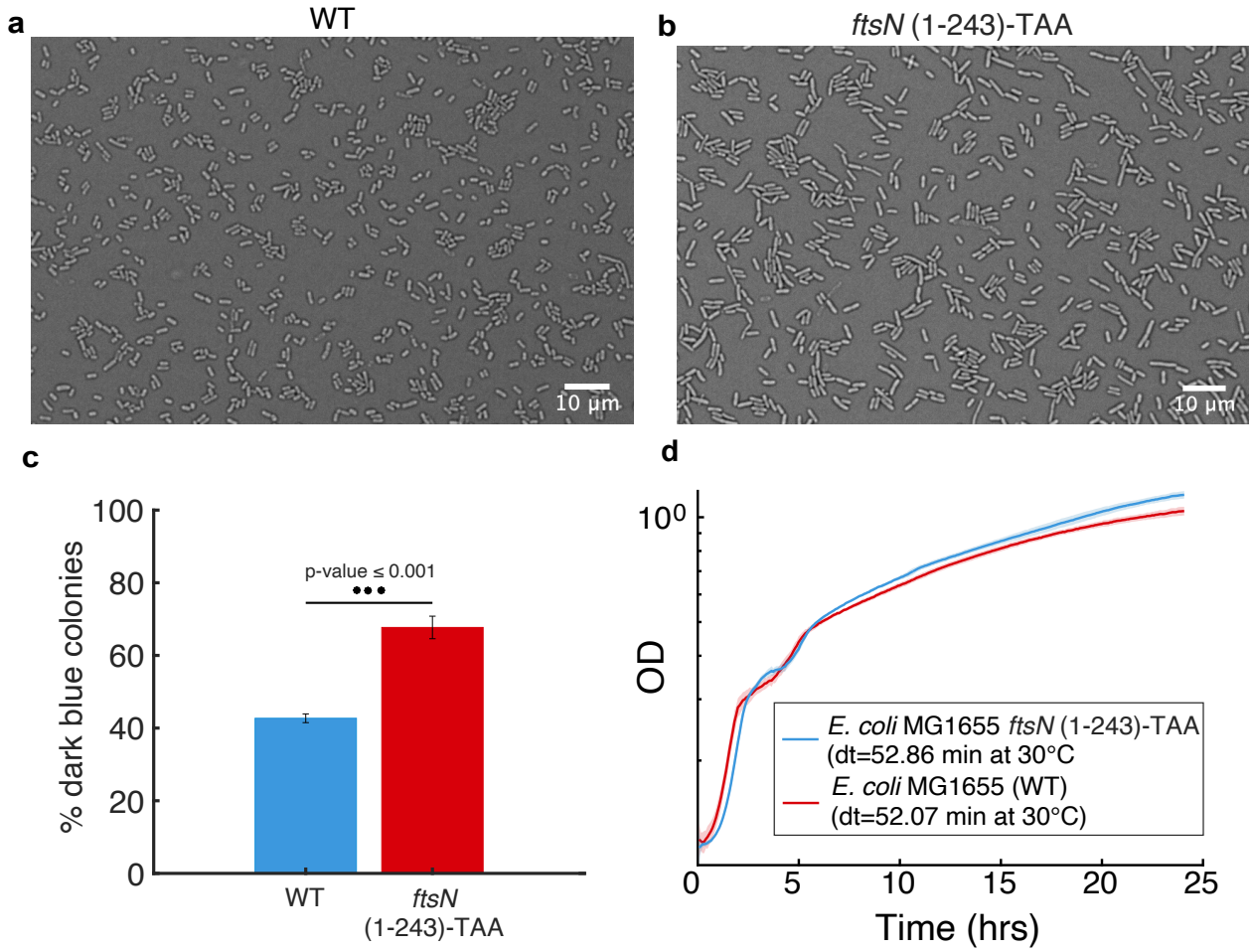

Fig. S16. A mutant with bigger cell size and similar growth rate propagates the Ch SSB prion with a higher stability. a) 60x microscopy image of background strain BLS80 cells in exponential phase. **b)** 60x microscopy image of BLS333 cells (N-terminal truncation of ftsN) in exponential phase, showing elongated cells compared to BLS80 (as previously reported (1)). **c)** The mutant strain with bigger cell size propagates the prion with a higher stability during replating. A pool of colonies containing Ch SSB prion aggregates were replated to assay stability and assessed for the presence of the prion using the PclpB-lacZ assay (dark blue indicates the presence of the prion). The percentage of colonies with prion-containing cells is higher in the mutant than in the WT, where ~60% of WT cells lose the prion during the replating compared to ~35% for the mutant. **d)** Growth curves for the WT (red) and ftsN mutant (blue) at 30°C, showing that they grow with similar doubling times (52.1 min for the WT and 52.9 min for the mutant).

References

1. Tropini, C. How the Physical Environment Shapes the Microbiota. *mSystems* **6**, e0067521 (2021).
2. Kho, Z. Y. & Lal, S. K. The Human Gut Microbiome - A Potential Controller of Wellness and Disease. *Front. Microbiol.* **9**, 1835 (2018).
3. Jandhyala, S. M. *et al.* Role of the normal gut microbiota. *World J. Gastroenterol.* **21**, 8787–8803 (2015).
4. Donaldson, G. P., Lee, S. M. & Mazmanian, S. K. Gut biogeography of the bacterial microbiota. *Nat. Rev. Microbiol.* **14**, 20–32 (2016).
5. Fallingborg, J. Intraluminal pH of the human gastrointestinal tract. *Dan. Med. Bull.* **46**, 183–196 (1999).
6. Sumigray, K. D., Terwilliger, M. & Lechler, T. Morphogenesis and Compartmentalization of the Intestinal Crypt. *Dev. Cell* **45**, 183–197.e5 (2018).
7. Pédron, T. *et al.* A crypt-specific core microbiota resides in the mouse colon. *MBio* **3**, (2012).
8. Nugent, S. G., Kumar, D., Rampton, D. S. & Evans, D. F. Intestinal luminal pH in inflammatory bowel disease: possible determinants and implications for therapy with aminosalicylates and other drugs. *Gut* **48**, 571–577 (2001).
9. Juckett, G. & Trivedi, R. Evaluation of chronic diarrhea. *Am. Fam. Physician* **84**, 1119–1126 (2011).
10. Tropini, C. *et al.* Transient Osmotic Perturbation Causes Long-Term Alteration to the Gut Microbiota. *Cell* **173**, 1742–1754.e17 (2018).
11. Najem, O., Shah, M. M. & De Jesus, O. *Serum Osmolality*. (StatPearls Publishing, 2022).
12. Koeppen, B. M. & Stanton, B. A. 1 - Physiology of Body Fluids. in *Renal Physiology (Fifth Edition)* (eds. Koeppen, B. M. & Stanton, B. A.) 1–14 (Mosby, 2013).
13. Shiau, Y. F., Feldman, G. M., Resnick, M. A. & Coff, P. M. Stool electrolyte and osmolality measurements in the evaluation of diarrheal disorders. *Ann. Intern. Med.* **102**, 773–775 (1985).
14. Burg, M. B. & Ferraris, J. D. Intracellular organic osmolytes: function and regulation. *J. Biol. Chem.*

283, 7309–7313 (2008).

15. Woods, T. A. Diarrhea. in *Clinical Methods: The History, Physical, and Laboratory Examinations* (eds. Walker, H. K., Hall, W. D. & Hurst, J. W.) (Butterworths).
16. Klaschik, E., Nauck, F. & Ostgathe, C. Constipation--modern laxative therapy. *Support. Care Cancer* **11**, 679–685 (2003).
17. Cesar, S. *et al.* Bacterial Evolution in High-Osmolarity Environments. *MBio* **11**, (2020).
18. Sleator, R. D. & Hill, C. Bacterial osmoadaptation: the role of osmolytes in bacterial stress and virulence. *FEMS Microbiol. Rev.* **26**, 49–71 (2002).
19. Caon, M. Osmoles, osmolality and osmotic pressure: clarifying the puzzle of solution concentration. *Contemp. Nurse* **29**, 92–99 (2008).
20. Altendorf, K. *et al.* Osmotic Stress. *EcoSal Plus* **3**, (2009).
21. Höltje, J. V. Growth of the stress-bearing and shape-maintaining murein sacculus of Escherichia coli. *Microbiol. Mol. Biol. Rev.* **62**, 181–203 (1998).
22. Christian, J. H. B. The Influence of Nutrition on the Water Relations of Salmonella Oranienburg. *Aust. Jnl. Of Bio. Sci.* **8**, 75–82 (1955).
23. Wood, J. M. Bacterial osmoregulation: a paradigm for the study of cellular homeostasis. *Annu. Rev. Microbiol.* **65**, 215–238 (2011).
24. Wood, J. M. Bacterial responses to osmotic challenges. *J. Gen. Physiol.* **145**, 381–388 (2015).
25. Kim, A. Y. C. Phosphoinositide interacting regulator of TRP (Pirt), a novel membrane protein in the somatosensory system. (2009).
26. Trchounian, A. & Kobayashi, H. Kup is the major K+ uptake system in Escherichia coli upon hyper-osmotic stress at a low pH. *FEBS Lett.* **447**, 144–148 (1999).
27. Asha, H. & Gowrishankar, J. Regulation of kdp operon expression in Escherichia coli: evidence against turgor as signal for transcriptional control. *J. Bacteriol.* **175**, 4528–4537 (1993).
28. Mellies, J., Brems, R. & Villarejo, M. The Escherichia coli proU promoter element and its contribution to osmotically signaled transcription activation. *J. Bacteriol.* **176**, 3638–3645 (1994).

29. Lamark, T., Røkenes, T. P., McDougall, J. & Strøm, A. R. The complex bet promoters of Escherichia coli: regulation by oxygen (ArcA), choline (BetI), and osmotic stress. *J. Bacteriol.* **178**, 1655–1662 (1996).

30. David, L. A. *et al.* Gut microbial succession follows acute secretory diarrhea in humans. *MBio* **6**, e00381–15 (2015).

31. Semrad, C. E. Approach to the Patient with Diarrhea and Malabsorption. *Goldman's Cecil Medicine* 895 (2012).

32. Vernia, P., Gnaedinger, A., Hauck, W. & Breuer, R. I. Organic anions and the diarrhea of inflammatory bowel disease. *Dig. Dis. Sci.* **33**, 1353–1358 (1988).

33. Barkas, F., Liberopoulos, E., Kei, A. & Elisaf, M. Electrolyte and acid-base disorders in inflammatory bowel disease. *Ann. Gastroenterol. Hepatol.* **26**, 23–28 (2013).

34. Tontini, G. E., Vecchi, M., Pastorelli, L., Neurath, M. F. & Neumann, H. Differential diagnosis in inflammatory bowel disease colitis: state of the art and future perspectives. *World J. Gastroenterol.* **21**, 21–46 (2015).

35. Lebwohl, B. & Rubio-Tapia, A. Epidemiology, Presentation, and Diagnosis of Celiac Disease. *Gastroenterology* **160**, 63–75 (2021).

36. Mattar, R., de Campos Mazo, D. F. & Carrilho, F. J. Lactose intolerance: diagnosis, genetic, and clinical factors. *Clin. Exp. Gastroenterol.* **5**, 113–121 (2012).

37. Olden, K. W. Diagnosis of irritable bowel syndrome. *Gastroenterology* **122**, 1701–1714 (2002).

38. GBD 2017 Inflammatory Bowel Disease Collaborators. The global, regional, and national burden of inflammatory bowel disease in 195 countries and territories, 1990-2017: a systematic analysis for the Global Burden of Disease Study 2017. *Lancet Gastroenterol Hepatol* **5**, 17–30 (2020).

39. ASGE Standards of Practice Committee *et al.* Bowel preparation before colonoscopy. *Gastrointest. Endosc.* **81**, 781–794 (2015).

40. Shobar, R. M. *et al.* The Effects of Bowel Preparation on Microbiota-Related Metrics Differ in Health and in Inflammatory Bowel Disease and for the Mucosal and Luminal Microbiota

Compartments. *Clin. Transl. Gastroenterol.* **7**, e143 (2016).

41. Nagata, N. *et al.* Effects of bowel preparation on the human gut microbiome and metabolome. *Sci. Rep.* **9**, 4042 (2019).
42. Bhalla, N., Jolly, P., Formisano, N. & Estrela, P. Introduction to biosensors. *Essays Biochem.* **60**, 1–8 (2016).
43. Vo-Dinh, T. & Cullum, B. Biosensors and biochips: advances in biological and medical diagnostics. *Fresenius J. Anal. Chem.* **366**, 540–551 (2000).
44. Turner, A., Karube, I. & Wilson, G. S. Biosensors : Fundamentals and Applications. (1987).
45. Van Dorst, B. *et al.* Recent advances in recognition elements of food and environmental biosensors: a review. *Biosens. Bioelectron.* **26**, 1178–1194 (2010).
46. Sharma, T. K., Ramanathan, R., Rakwal, R., Agrawal, G. K. & Bansal, V. Moving forward in plant food safety and security through NanoBioSensors: Adopt or adapt biomedical technologies? *Proteomics* **15**, 1680–1692 (2015).
47. Jolly, P., Formisano, N. & Estrela, P. DNA aptamer-based detection of prostate cancer: *Chem. Pap.* **69**, 77–89 (2015).
48. Paddle, B. M. Biosensors for chemical and biological agents of defence interest. *Biosens. Bioelectron.* **11**, 1079–1113 (1996).
49. Mehrotra, P. Biosensors and their applications - A review. *J Oral Biol Craniofac Res* **6**, 153–159 (2016).
50. Song, Y. *et al.* Application of Bacterial Whole-Cell Biosensors in Health. in *Handbook of Cell Biosensors* (ed. Thouand, G.) 945–961 (Springer International Publishing, 2022).
51. Su, L., Jia, W., Hou, C. & Lei, Y. Microbial biosensors: a review. *Biosens. Bioelectron.* **26**, 1788–1799 (2011).
52. Lim, J. W., Ha, D., Lee, J., Lee, S. K. & Kim, T. Review of micro/nanotechnologies for microbial biosensors. *Front Bioeng Biotechnol* **3**, 61 (2015).
53. Ravikumar, S., Baylon, M. G., Park, S. J. & Choi, J.-I. Engineered microbial biosensors based on

bacterial two-component systems as synthetic biotechnology platforms in bioremediation and biorefinery. *Microb. Cell Fact.* **16**, 62 (2017).

54. Park, M., Tsai, S.-L. & Chen, W. Microbial biosensors: engineered microorganisms as the sensing machinery. *Sensors* **13**, 5777–5795 (2013).
55. Chang, H.-J. *et al.* Programmable receptors enable bacterial biosensors to detect pathological biomarkers in clinical samples. *Nat. Commun.* **12**, 5216 (2021).
56. Wang, J. & Childers, W. S. The Future Potential of Biosensors to Investigate the Gut-Brain Axis. *Front Bioeng Biotechnol* **9**, 826479 (2021).
57. Tanna, T., Ramachanderan, R. & Platt, R. J. Engineered bacteria to report gut function: technologies and implementation. *Curr. Opin. Microbiol.* **59**, 24–33 (2021).
58. Ursell, L. K., Metcalf, J. L., Parfrey, L. W. & Knight, R. Defining the human microbiome. *Nutr. Rev.* **70 Suppl 1**, S38–44 (2012).
59. Kinross, J. M., Darzi, A. W. & Nicholson, J. K. Gut microbiome-host interactions in health and disease. *Genome Med.* **3**, 14 (2011).
60. Riglar, D. T. & Silver, P. A. Engineering bacteria for diagnostic and therapeutic applications. *Nat. Rev. Microbiol.* **16**, 214–225 (2018).
61. Ulrich, L. E., Koonin, E. V. & Zhulin, I. B. One-component systems dominate signal transduction in prokaryotes. *Trends Microbiol.* **13**, 52–56 (2005).
62. Mitrophanov, A. Y. & Groisman, E. A. Signal integration in bacterial two-component regulatory systems. *Genes Dev.* **22**, 2601–2611 (2008).
63. Guet, C. C., Elowitz, M. B., Hsing, W. & Leibler, S. Combinatorial synthesis of genetic networks. *Science* **296**, 1466–1470 (2002).
64. Green, A. A. *et al.* Complex cellular logic computation using ribocomputing devices. *Nature* **548**, 117–121 (2017).
65. Sheth, R. U. & Wang, H. H. DNA-based memory devices for recording cellular events. *Nat. Rev. Genet.* **19**, 718–732 (2018).

66. Benitez, J.-M. *et al.* Role of endoscopy, cross-sectional imaging and biomarkers in Crohn's disease monitoring. *Gut* **62**, 1806–1816 (2013).

67. Tang, Q. *et al.* Current Sampling Methods for Gut Microbiota: A Call for More Precise Devices. *Front. Cell. Infect. Microbiol.* **10**, 151 (2020).

68. Loftus, E. V., Jr. Clinical epidemiology of inflammatory bowel disease: Incidence, prevalence, and environmental influences. *Gastroenterology* **126**, 1504–1517 (2004).

69. Archer, E. J., Robinson, A. B. & Süel, G. M. Engineered E. coli that detect and respond to gut inflammation through nitric oxide sensing. *ACS Synth. Biol.* **1**, 451–457 (2012).

70. Chen, X. J., Wang, B., Thompson, I. P. & Huang, W. E. Rational Design and Characterization of Nitric Oxide Biosensors in E. coli Nissle 1917 and Mini SimCells. *ACS Synth. Biol.* **10**, 2566–2578 (2021).

71. Daeffler, K. N.-M. *et al.* Engineering bacterial thiosulfate and tetrathionate sensors for detecting gut inflammation. *Mol. Syst. Biol.* **13**, 923 (2017).

72. Riglar, D. T. *et al.* Engineered bacteria can function in the mammalian gut long-term as live diagnostics of inflammation. *Nat. Biotechnol.* **35**, 653–658 (2017).

73. Chien, T. *et al.* Enhancing the tropism of bacteria via genetically programmed biosensors. *Nat Biomed Eng* **6**, 94–104 (2022).

74. Woo, S.-G. *et al.* A designed whole-cell biosensor for live diagnosis of gut inflammation through nitrate sensing. *Biosens. Bioelectron.* **168**, 112523 (2020).

75. Vaaben, T. H., Vazquez-Uribe, R. & Sommer, M. O. A. Characterization of Eight Bacterial Biosensors for Microbial Diagnostic and Therapeutic Applications. *ACS Synth. Biol.* **11**, 4184–4192 (2022).

76. Riglar, D. T. *et al.* Bacterial variability in the mammalian gut captured by a single-cell synthetic oscillator. *Nat. Commun.* **10**, 4665 (2019).

77. Mimee, M., Tucker, A. C., Voigt, C. A. & Lu, T. K. Programming a Human Commensal Bacterium, Bacteroides thetaiotaomicron, to Sense and Respond to Stimuli in the Murine Gut Microbiota. *Cell*

Syst **1**, 62–71 (2015).

78. Pedrolli, D. B. *et al.* Engineering Microbial Living Therapeutics: The Synthetic Biology Toolbox. *Trends Biotechnol.* **37**, 100–115 (2019).
79. Zhao, L. *et al.* A comparative study on the genomes, transcriptomes, and metabolic properties of Escherichia coli strains Nissle 1917, BL21(DE3), and MG1655. *Engineering Microbiology* **2**, 100012 (2022).
80. Charbonneau, M. R., Isabella, V. M., Li, N. & Kurtz, C. B. Developing a new class of engineered live bacterial therapeutics to treat human diseases. *Nat. Commun.* **11**, 1738 (2020).
81. Sonnenborn, U. Escherichia coli strain Nissle 1917—from bench to bedside and back: history of a special Escherichia coli strain with probiotic properties. *FEMS Microbiol. Lett.* **363**, fnw212 (2016).
82. Schultz, M. Clinical use of E. coli Nissle 1917 in inflammatory bowel disease. *Inflamm. Bowel Dis.* **14**, 1012–1018 (2008).
83. Deriu, E. *et al.* Probiotic bacteria reduce salmonella typhimurium intestinal colonization by competing for iron. *Cell Host Microbe* **14**, 26–37 (2013).
84. Kurtz, C. *et al.* Translational Development of Microbiome-Based Therapeutics: Kinetics of E. coli Nissle and Engineered Strains in Humans and Nonhuman Primates. *Clin. Transl. Sci.* **11**, 200–207 (2018).
85. Zhao, L. *et al.* A comparative study on the genomes, transcriptomes, and metabolic properties of Escherichia coli strains Nissle 1917, BL21(DE3), and MG1655. *Engineering Microbiology* vol. 2 100012 Preprint at https://doi.org/10.1016/j.engmic.2022.100012 (2022).
86. Elowitz, M. B., Levine, A. J., Siggia, E. D. & Swain, P. S. Stochastic gene expression in a single cell. *Science* **297**, 1183–1186 (2002).
87. Westreich, S. T., Treiber, M. L., Mills, D. A., Korf, I. & Lemay, D. G. SAMSA2: a standalone metatranscriptome analysis pipeline. *BMC Bioinformatics* **19**, 175 (2018).
88. Love, M. I., Huber, W. & Anders, S. Moderated estimation of fold change and dispersion for RNA-seq data with DESeq2. *Genome Biol.* **15**, 550 (2014).

89. Webb, M. The effect of magnesium on the growth and cell division of various bacterial species in complex media. *J. Gen. Microbiol.* **3**, 410–417 (1949).

90. Odahara, T. Stability and solubility of integral membrane proteins from photosynthetic bacteria solubilized in different detergents. *Biochim. Biophys. Acta* **1660**, 80–92 (2004).

91. Di Palma, J. A., Smith, J. R. & Cleveland, M. vB. Overnight efficacy of polyethylene glycol laxative. *Am. J. Gastroenterol.* **97**, 1776–1779 (2002).

92. Battesti, A., Majdalani, N. & Gottesman, S. The RpoS-mediated general stress response in Escherichia coli. *Annu. Rev. Microbiol.* **65**, 189–213 (2011).

93. Jozefczuk, S. *et al.* Metabolomic and transcriptomic stress response of Escherichia coli. *Mol. Syst. Biol.* **6**, 364 (2010).

94. Chung, H. J., Bang, W. & Drake, M. A. Stress response of Escherichia coli. *Compr. Rev. Food Sci. Food Saf.* **5**, 52–64 (2006).

95. Wang, Y., Chen, Y., Zhang, X., Lu, Y. & Chen, H. New insights in intestinal oxidative stress damage and the health intervention effects of nutrients: A review. *J. Funct. Foods* **75**, 104248 (2020).

96. González Plaza, J. J., Hulak, N., Zhumadilov, Z. & Akilzhanova, A. Fever as an important resource for infectious diseases research. *Intractable Rare Dis Res* **5**, 97–102 (2016).

97. Weber, A. & Jung, K. Profiling early osmostress-dependent gene expression in Escherichia coli using DNA macroarrays. *J. Bacteriol.* **184**, 5502–5507 (2002).

98. Gunasekera, T. S., Csonka, L. N. & Paliy, O. Genome-wide transcriptional responses of Escherichia coli K-12 to continuous osmotic and heat stresses. *J. Bacteriol.* **190**, 3712–3720 (2008).

99. Seo, S. W. *et al.* Revealing genome-scale transcriptional regulatory landscape of OmpR highlights its expanded regulatory roles under osmotic stress in Escherichia coli K-12 MG1655. *Scientific Reports* vol. 7 Preprint at https://doi.org/10.1038/s41598-017-02110-7 (2017).

100. Mager, W. H., de Boer, A. H., Siderius, M. H. & Voss, H. P. Cellular responses to oxidative and osmotic stress. *Cell Stress Chaperones* **5**, 73–75 (2000).

101. Lever, J., Krzywinski, M. & Altman, N. Principal component analysis. *Nat. Methods* **14**, 641–642 (2017).

102. Burden, C. J., Qureshi, S. E. & Wilson, S. R. Error estimates for the analysis of differential expression from RNA-seq count data. *PeerJ* **2**, e576 (2014).

103. Nyström, T. Stationary-phase physiology. *Annu. Rev. Microbiol.* **58**, 161–181 (2004).

104. Cummings, J. H., Jenkins, D. J. & Wiggins, H. S. Measurement of the mean transit time of dietary residue through the human gut. *Gut* **17**, 210–218 (1976).

105. Chakraborty, S., Winardhi, R. S., Morgan, L. K., Yan, J. & Kenney, L. J. Non-canonical activation of OmpR drives acid and osmotic stress responses in single bacterial cells. *Nat. Commun.* **8**, 1587 (2017).

106. Gowrishankar, J. Nucleotide sequence of the osmoregulatory proU operon of Escherichia coli. *J. Bacteriol.* **171**, 1923–1931 (1989).

107. Dattananda, C. S. & Gowrishankar, J. Osmoregulation in Escherichia coli: complementation analysis and gene-protein relationships in the proU locus. *J. Bacteriol.* **171**, 1915–1922 (1989).

108. Manna, D. & Gowrishankar, J. Evidence for involvement of proteins HU and RpoS in transcription of the osmoresponsive proU operon in Escherichia coli. *J. Bacteriol.* **176**, 5378–5384 (1994).

109. Lloyd, C. R., Park, S., Fei, J. & Vanderpool, C. K. The Small Protein SgrT Controls Transport Activity of the Glucose-Specific Phosphotransferase System. *J. Bacteriol.* **199**, (2017).

110. Checroun, C. ?s-Dependent regulation of yehZYXW, which encodes a putative osmoprotectant ABC transporter of Escherichia coli. *FEMS Microbiology Letters* vol. 236 221–226 Preprint at https://doi.org/10.1016/j.femsle.2004.05.046 (2004).

111. Lang, S. *et al.* YehZYXW of Escherichia coli Is a Low-Affinity, Non-Osmoregulatory Betaine-Specific ABC Transporter. *Biochemistry* **54**, 5735–5747 (2015).

112. May, G., Faatz, E., Villarejo, M. & Bremer, E. Binding protein dependent transport of glycine betaine and its osmotic regulation in Escherichia coli K12. *Mol. Gen. Genet.* **205**, 225–233 (1986).

113. Gowrishankar, J. Identification of osmoresponsive genes in Escherichia coli: evidence for

participation of potassium and proline transport systems in osmoregulation. *J. Bacteriol.* **164**, 434–445 (1985).

114. Faatz, E., Middendorf, A. & Bremer, E. Cloned structural genes for the osmotically regulated binding-protein-dependent glycine betaine transport system (ProU) of Escherichia coli K-12. *Molecular Microbiology* vol. 2 265–279 Preprint at https://doi.org/10.1111/j.1365-2958.1988.tb00028.x (1988).

115. Rajkumari K. & Gowrishankar J. In Vivo Expression from the RpoS-Dependent P1 Promoter of the Osmotically Regulated proU Operon inEscherichia coli and Salmonella entericaSerovar Typhimurium: Activation by rho andhns Mutations and by Cold Stress. *J. Bacteriol.* **183**, 6543–6550 (2001).

116. Rajkumari, K., Kusano, S., Ishihama, A., Mizuno, T. & Gowrishankar, J. Effects of H-NS and potassium glutamate on sigmaS- and sigma70-directed transcription in vitro from osmotically regulated P1 and P2 promoters of proU in Escherichia coli. *J. Bacteriol.* **178**, 4176–4181 (1996).

117. Miura, C. *et al.* Functional characterization of the principal sigma factor RpoD of phytoplasmas via an in vitro transcription assay. *Sci. Rep.* **5**, 11893 (2015).

118. Schellhorn, H. E. Function, Evolution, and Composition of the RpoS Regulon in Escherichia coli. *Front. Microbiol.* **11**, 560099 (2020).

119. Lucht, J. M. & Bremer, E. Adaptation of Escherichia coli to high osmolarity environments: osmoregulation of the high-affinity glycine betaine transport system proU. *FEMS Microbiol. Rev.* **14**, 3–20 (1994).

120. Raina, M. & Storz, G. SgrT, a Small Protein That Packs a Sweet Punch. *Journal of bacteriology* vol. 199 (2017).

121. Wadler, C. S. & Vanderpool, C. K. A dual function for a bacterial small RNA: SgrS performs base pairing-dependent regulation and encodes a functional polypeptide. *Proc. Natl. Acad. Sci. U. S. A.* **104**, 20454–20459 (2007).

122. Record, M. T., Jr, Courtenay, E. S., Cayley, D. S. & Guttman, H. J. Responses of E. coli to osmotic

stress: large changes in amounts of cytoplasmic solutes and water. *Trends Biochem. Sci.* **23**, 143–148 (1998).

123. Erickson, J. W., Vaughn, V., Walter, W. A., Neidhardt, F. C. & Gross, C. A. Regulation of the promoters and transcripts of rpoH, the Escherichia coli heat shock regulatory gene. *Genes Dev.* **1**, 419–432 (1987).

124. Altschuler, S. J. & Wu, L. F. Cellular heterogeneity: do differences make a difference? *Cell* **141**, 559–563 (2010).

125. Goldman, S. L. *et al.* The Impact of Heterogeneity on Single-Cell Sequencing. *Front. Genet.* **10**, 8 (2019).

126. Prusiner, S. B. Novel proteinaceous infectious particles cause scrapie. *Science* **216**, 136–144 (1982).

127. Chakravarty, A. K. & Jarosz, D. F. More than Just a Phase: Prions at the Crossroads of Epigenetic Inheritance and Evolutionary Change. *J. Mol. Biol.* **430**, 4607–4618 (2018).

128. Fleming, E., Yuan, A. H., Heller, D. M. & Hochschild, A. A bacteria-based genetic assay detects prion formation. *Proc. Natl. Acad. Sci. U. S. A.* **116**, 4605–4610 (2019).

129. Yuan, A. H. & Hochschild, A. A bacterial global regulator forms a prion. *Science* **355**, 198–201 (2017).

130. Glover, J. R. *et al.* Self-Seeded Fibers Formed by Sup35, the Protein Determinant of [PSI+], a Heritable Prion-like Factor of S. cerevisiae. *Cell* **89**, 811–819 (1997).

131. True, H. L. & Lindquist, S. L. A yeast prion provides a mechanism for genetic variation and phenotypic diversity. *Nature* **407**, 477–483 (2000).

132. Jakobson, C. M. & Jarosz, D. F. Organizing biochemistry in space and time using prion-like self-assembly. *Current Opinion in Systems Biology* **8**, 16–24 (2018).

133. Levkovich, S. A., Rencus-Lazar, S., Gazit, E. & Laor Bar-Yosef, D. Microbial Prions: Dawn of a New Era. *Trends Biochem. Sci.* **46**, 391–405 (2021).

134. Tuite, M. F. & Serio, T. R. The prion hypothesis: from biological anomaly to basic regulatory mechanism. *Nat. Rev. Mol. Cell Biol.* **11**, 823–833 (2010).

135. Majumdar, A. *et al.* Critical role of amyloid-like oligomers of Drosophila Orb2 in the persistence of memory. *Cell* **148**, 515–529 (2012).

136. Chakrabortee, S. *et al.* Luminidependens (LD) is an Arabidopsis protein with prion behavior. *Proc. Natl. Acad. Sci. U. S. A.* **113**, 6065–6070 (2016).

137. Fioriti, L. *et al.* The Persistence of Hippocampal-Based Memory Requires Protein Synthesis Mediated by the Prion-like Protein CPEB3. *Neuron* **86**, 1433–1448 (2015).

138. Hou, F. *et al.* MAVS forms functional prion-like aggregates to activate and propagate antiviral innate immune response. *Cell* **146**, 448–461 (2011).

139. Xu, H. *et al.* Structural basis for the prion-like MAVS filaments in antiviral innate immunity. *Elife* **2014**, 1–25 (2014).

140. Liebman, S. W. & Chernoff, Y. O. Prions in yeast. *Genetics* **191**, 1041–1072 (2012).

141. Li, J. *et al.* The RIP1/RIP3 necrosome forms a functional amyloid signaling complex required for programmed necrosis. *Cell* **150**, 339–350 (2012).

142. Si, K., Choi, Y. B., White-Grindley, E., Majumdar, A. & Kandel, E. R. Aplysia CPEB Can Form Prion-like Multimers in Sensory Neurons that Contribute to Long-Term Facilitation. *Cell* **140**, 421–435 (2010).

143. Newby, G. A. & Lindquist, S. Blessings in disguise: Biological benefits of prion-like mechanisms. *Trends Cell Biol.* **23**, 251–259 (2013).

144. Halfmann, R. *et al.* Prions are a common mechanism for phenotypic inheritance in wild yeasts. *Nature* **482**, 363–368 (2012).

145. Prusiner, S. B. Molecular biology of prion diseases. *Science* **252**, 1515–1522 (1991).

146. Solforosi, L., Milani, M., Mancini, N., Clementi, M. & Burioni, R. A closer look at prion strains: characterization and important implications. *Prion* **7**, 99–108 (2013).

147. Tanaka, M., Collins, S. R., Toyama, B. H. & Weissman, J. S. The physical basis of how prion conformations determine strain phenotypes. *Nature* **442**, 585–589 (2006).

148. Toyama, B. H. & Weissman, J. S. Amyloid structure: conformational diversity and consequences.

Annu. Rev. Biochem. **80**, 557–585 (2011).

149. Krishnan, R. & Lindquist, S. L. Structural insights into a yeast prion illuminate nucleation and strain diversity. *Nature* **435**, 765–772 (2005).

150. Meisl, G. *et al.* Scaling analysis reveals the mechanism and rates of prion replication in vivo. *Nat. Struct. Mol. Biol.* **28**, 365–372 (2021).

151. Villali, J. *et al.* Nucleation seed size determines amyloid clearance and establishes a barrier to prion appearance in yeast. *Nat. Struct. Mol. Biol.* **27**, 540–549 (2020).

152. Nowak, M. A., Krakauer, D. C. & Klug, A. Prion infection dynamics. *Biology: Issues, News ...* doi:10.1002/(SICI)1520-6602(1998)1:1<3::AID-INBI2>3.0.CO;2-9.

153. Sindi, S. S. Mathematical modeling of prion disease. *Prion-an overview, InTech* 207–227 (2017).

154. Masel, J., Jansen, V. A. & Nowak, M. A. Quantifying the kinetic parameters of prion replication. *Biophys. Chem.* **77**, 139–152 (1999).

155. Chernoff, Y., Lindquist, S., Ono, B., Inge-Vechtomov, S. & Liebman, S. Role of the chaperone protein Hsp104 in propagation of the yeast prion-like factor [psi+]. *Science* **268**, 880–884 (1995).

156. Derkatch, I. L., Bradley, M. E., Hong, J. Y. & Liebman, S. W. Prions affect the appearance of other prions: The story of [PIN+]. *Cell* **106**, 171–182 (2001).

157. Derkatch, I. L., Bradley, M. E., Zhou, P., Chernoff, Y. O. & Liebman, S. W. Genetic and Environmental Factors Affecting the de novo Appearance of the [PSI +] Prion in Saccharomyces cerevisiae. *Genetics* **147**, 507–519 (1997).

158. Osherovich, L. Z. & Weissman, J. S. Multiple Gln/Asn-Rich Prion Domains Confer Susceptibility to Induction of the Yeast [PSI+] Prion. *Cell* **106**, 183–194 (2001).

159. Fleming, E., Yuan, A. H., Heller, D. M. & Hochschild, A. A bacteria-based genetic assay detects prion formation. *Proc. Natl. Acad. Sci. U. S. A.* **116**, 4605–4610 (2019).

160. Yuan A.H. Garrity S.J. Nako E. and Hochschild, A. Prion propagation can occur in a prokaryote and requires the ClpB chaperone. *Elife* **10.7554**, eLife.02949 (2014).

161. Santoso, A., Chien, P., Osherovich, L. Z. & Weissman, J. S. Molecular basis of a yeast prion species

barrier. *Cell* **100**, 277–288 (2000).

162. Derkatch, I. L., Chernoff, Y. O., Kushnirov, V. V., Inge-Vechtomov, S. G. & Liebman, S. W. Genesis and variability of [PSI] prion factors in Saccharomyces cerevisiae. *Genetics* **144**, 1375–1386 (1996).

163. Wang, P. *et al.* Robust growth of Escherichia coli. *Curr. Biol.* **20**, 1099–1103 (2010).

164. Greene, L. E., Saba, F., Silberman, R. E. & Zhao, X. Mechanisms for Curing Yeast Prions. *Int. J. Mol. Sci.* **21**, (2020).

165. Ness, F., Cox, B. S., Wongwigkarn, J., Naeimi, W. R. & Tuite, M. F. Over-expression of the molecular chaperone Hsp104 in*Saccharomyces cerevisiae*results in the malpartition of [*PSI*] propagons. *Molecular Microbiology* vol. 104 125–143 Preprint at https://doi.org/10.1111/mmi.13617 (2017).

166. Huh, D. & Paulsson, J. Random partitioning of molecules at cell division. *Proc. Natl. Acad. Sci. U. S. A.* **108**, 15004–15009 (2011).

167. Huh, D. & Paulsson, J. Non-genetic heterogeneity from stochastic partitioning at cell division. *Nat. Genet.* **43**, 95–100 (2011).

168. Lemarre, P., Pujo-Menjouet, L. & Sindi, S. S. A unifying model for the propagation of prion proteins in yeast brings insight into the [PSI] prion. *PLOS Computational Biology* vol. 16 e1007647 Preprint at https://doi.org/10.1371/journal.pcbi.1007647 (2020).

169. Lemarre, P., Pujo-Menjouet, L. & Sindi, S. S. Generalizing a mathematical model of prion aggregation allows strain coexistence and co-stability by including a novel misfolded species. *J. Math. Biol.* **78**, 465–495 (2019).

170. Derdowski, A., Sindi, S. S., Klaips, C. L., DiSalvo, S. & Serio, T. R. A size threshold limits prion transmission and establishes phenotypic diversity. *Science* **330**, 680–683 (2010).

171. Gillespie, D. T. Exact stochastic simulation of coupled chemical reactions. *J. Phys. Chem.* **93555**, 2340–2361 (1977).

172. Truong, T. T., Vettiger, A. & Bernhardt, T. G. Cell division is antagonized by the activity of

peptidoglycan endopeptidases that promote cell elongation. *Mol. Microbiol.* **114**, 966–978 (2020).

173. Milo, R. What is the total number of protein molecules per cell volume? A call to rethink some published values. *Bioessays* **35**, 1050–1055 (2013).

174. Arike, L. *et al.* Comparison and applications of label-free absolute proteome quantification methods on Escherichia coli. *J. Proteomics* **75**, 5437–5448 (2012).

175. Uptain, S. M., Sawicki, G. J., Caughey, B. & Lindquist, S. Strains of [PSI+] are distinguished by their efficiencies of prion-mediated conformational conversion. *EMBO J.* **20**, 6236–6245 (2001).

176. Toyama, B. H., Kelly, M. J. S., Gross, J. D. & Weissman, J. S. The structural basis of yeast prion strain variants. *Nature* **449**, 233–237 (2007).

177. Sawaya, M. R. *et al.* Atomic structures of amyloid cross-beta spines reveal varied steric zippers. *Nature* **447**, 453–457 (2007).

178. Kim, M.-O., Takada, L. T., Wong, K., Forner, S. A. & Geschwind, M. D. Genetic PrP Prion Diseases. *Cold Spring Harb. Perspect. Biol.* **10**, (2018).

179. Takada, L. T. *et al.* Genetic prion disease: Experience of a rapidly progressive dementia center in the United States and a review of the literature. *Am. J. Med. Genet. B Neuropsychiatr. Genet.* **174**, 36–69 (2017).

180. Mastrianni, J. A. The genetics of prion diseases. *Genet. Med.* **12**, 187–195 (2010).

181. Darling, A. C. E., Mau, B., Blattner, F. R. & Perna, N. T. Mauve: multiple alignment of conserved genomic sequence with rearrangements. *Genome Res.* **14**, 1394–1403 (2004).